# FRACTURES SYSTEM WITHIN QUSAIBA SHALE OUTCROP AND ITS REALTIONSHIP TO THE GEOMECHANICAL AND LITHOLOGICAL PROPERTIES, QASIM AREA, CENTRAL SAUDI ARABIA

BY

**MOHAMED IBRAHIM MAHGOUB IBRAHIM**

A Thesis Presented to the
DEANSHIP OF GRADUATE STUDIES

**KING FAHD UNIVERSITY OF PETROLEUM & MINERALS**
DHAHRAN, SAUDI ARABIA

In Partial Fulfillment of the
Requirements for the Degree of

**MASTER OF SCIENCE**

**In**

**Geology**

**DEC 2016**

KING FAHD UNIVERSITY OF PETROLEUM & MINERALS

DHAHRAN- 31261, SAUDI ARABIA

**DEANSHIP OF GRADUATE STUDIES**

This thesis, written by **Mohamed Ibrahim** under the direction of his thesis advisor and approved by his thesis committee, has been presented and accepted by the Dean of Graduate Studies, in partial fulfillment of the requirements for the degree of **MASTER OF SCIENCE IN GEOLOGY**

Dr. Mustaffa Mohammad Hariri
(Advisor)

Dr. Abdulaziz Al-Shaibani
Department Chairman

Dr. Osman M. Abdullatif
(Member)

Dr. Salam A. Zummo
Dean of Graduate Studies

Dr. Mohammad Husain Makkawi
(Member)

10/1/17

Date

I dedicate this work for my mother and father, for my beloved sister and brothers, and for Gaidah.

# ACKNOWLEDGMENTS

Thanks to Allah for giving me Patience, health and strength to complete this work.

Thanks to King Fahd University of Petroleum & Minerals and to DSR project No. RG1418-1 -Qusaiba member shale gas reservoir characterization: Outcrop analog from Northwest Saudi Arabia- for providing technical and financial help throughout this research.

Thanks to my Committee Chairman, Dr. Mustafa Hariri for his great effort and guidance. Great thanks to my committee members Dr. Osman Abdullatif and Dr. Mohammad Makkawi for their guidance and support. Thanks to Dr. Abdulaziz Al-Shaibani, the chairman of Earth Sciences Department and to all the department's faculty members.

Thanks are also extended to all my colleagues in the department; students, technicians and staff for helping me in the field and laboratory work.

Special thanks to the Sudanese community in KFUPM.

Thanks to my mother whom I wouldn't have done anything if not for her.

Endless thanks to Gaidah for her permanent support.

# TABLE OF CONTENTS

# LIST OF TABLES

# LIST OF FIGURES

# ABSTRACT

| | | |
|---|---|---|
| Full Name | : | [Mohamed Ibrahim Mahgoub Ibrahim] |
| Thesis Title | : | [Fractures System Within Quasiba Shale Outcrop and its Relationship to the Geomechanical and Lithological Properties, Qasim Area, Central Saudi Arabia] |
| Major Field | : | [Geology] |
| Date of Degree | : | [Dec 2016] |

The basal Qusaiba hot shale member of Qalibah formation is considered to be an important source rock in the Paleozoic petroleum system of Saudi Arabia and an exploration target for tight shale as one of the unconventional resources of petroleum. The aim of this study is to define and understand the fractures network of Qusaiba shale member in outcrops located to the west of Qusayba' village in Al-Qasim area, Central Saudi Arabia. The main objective of studying fractures in Qusaiba shale member was to understand its relationship with lithology, geomechanical characteristics, and petrophysical properties. Fractures were studied in different scales in the study area from Lineaments to rock samples; Lineaments were analyzed and interpreted in a GIS environment using Spot-7 and Landsat-ETM+ high-resolution satellite images on a regional scale, and linear scanline method was used to characterize fractures on an outcrop- and bed-scale. Description data sheets were used for the detailed lithological description of Qusaiba shale member on two outcrops of 40m and 20m height respectively. Spectral gamma ray tool was used in the field to examine the fine cyclicity of the lithology, and Schmidt hammer to test the surface hardness and penetration resistance of different rock types. 60 rock samples of different lithologies were taken from the two outcrops for further geomechanical and petrophysical measurements. X-ray diffraction (XRD), Scanning electron microscope (SEM), and thin sections were used to define different lithofacies in the study area. A 3D geostatistical model has been generated using Sequential indicator simulation (SIS) and Truncated Gaussian Simulation (TGS) to describe the distribution of the lithofacies in the area by studying thickness and continuity of the layers in 12 pseudo-logs. Qusaiba shale member in the study area consists of 5 main lithofacies, divided based on their sedimentary structures and petrographic properties, from base to top; fissile shale lithofacies, very fine-grained micaceous siltstone, bioturbated mudstone, very fine to fine-grained hummocky cross-stratified sandstone, and fine to medium-grained low/high angle cross-stratified sandstone. Lineaments interpretation of the Spot-7 and Landsat ETM+ satellite images showed two major directions in the study area; 320º that follows the direction of Najd fault system and 20º that follows the direction of the extensional activities that took place after Amar collision. Higher density of fractures is within the fissile shale and mudstone lithofacies than sandstones lithofacies, and spacing is smaller in the fissile shale and mudstone lithofacies when compared to sandstones. Lineaments and large-scale fractures are Non-Stratabound fractures and they deal with the area as one big mechanical unit, whereas small-scale fractures are Stratabound fractures that propose different mechanical units within Qusaiba shale member in the study area. Strength geomechanical parameters such as Schmidt hammer, point load index, uniaxial compressive strength, and dynamic young modulus have greater values in the hummocky cross-stratified sandstone, low/high angle cross-stratified sandstone, and pebbly sandstone than in fissile shale, mudstone, and siltstone. Accordingly, the outcrops of Qusaiba shale member in the study area were divided into Five geomechanical units; from unit-1 to unit-5 based on their fractures density, petrophysical properties, and geomechanical properties.

This work would have a significant contribution to tight shale exploration plans in the subsurface by providing some knowledge about the mechanical behavior of the lower part of Qusaiba shale member of Qalibah formation.

# ملخص الرسالة

**الاسم الكامل: محمد ابراهيم محجوب ابراهيم**

**عنوان الرسالة: نظام الكسور في متكشفات طين قصيباء وعلاقتها بالخصائص الجيوميكانيكية والصخرية, منطقة القصيم, وسط المملكة العربية السعودية.**

**التخصص: جيولوجيا**

**تاريخ الدرجة العلمية: ديسمبر 2016**

**يعد الجزء السفلي من عضو قصيباء الغني بالمواد العضوية والتابع لمتكون القليبة من أهم صخور المصدر في نظام البترول التابع للعصر الباليوزوي في المنطقة العربية, وأحد أهداف استكشاف النفط الصخري غير التقليدي. تقوم هذه الدراسة على فهم نظام الكسور التكتونية وغير التكتونية لعضو قصيباء في متكشفات صخرية تقع غرب قرية قصيباء في منطقة القصيم بالمملكة العربية السعودية. الهدف الرئيسي من هذا البحث هو دراسة وفهم توزيع الكسور الطبيعية على الصخور ذات الخصائص الجيولوجية المختلفة, وعلاقتها بالخصائص الميكانيكية والفيزيائية لهذه الصخور. تم استخدام أوراق الوصف التفصيلي من أجل وصف الخصائص التركيبية لعضو قصيباء الطيني على متكشفين صخريين رئيسيين. جهاز أشعة جاما تم استخدامه في الحقل لاختبار التكرار الدوري للخصائص التركيبية الصخرية, وجهاز مطرقة شميدت لاختبار قوة السطح ومقاومة الاختراق للأنواع المختلفة من الصخور المكونة للعضو. توصيف الصخور في حقل الدراسة تم عمله عن باستخدام طريقة المسح الخطي. تم أخذ ستين عينة صخرية من المتكشفين الصخريين الرئيسيين لاجراء التحاليل الميكانيكية والفيبائية المختبرية. تم اجراء اختبار حيود الأشعة السينية واستخدام مجهر المسح الالكتروني والعينات الرقيقة المجهرية للمساعدة في تحديد السحنات الصخرية المختلفة في المنطقة. تم تصميم نموذج جيوإحصائي ثلاثي الأبعاد باستخدام محاكاة مؤشر المتابعة ومحاكاة اقتطاع جاوس لوصف توزيع السحنات الصخرية المختلفة على منطقة الدراسة عن طريق حساب سُمك واستمرارية الطبقات في اثني عشرة سجلاً اضافياً. تم استخدام صورتين جويتين سبوت-7 ولاندسات حرارية من أجل متابعة الأشكال الخطية وتحليلها على المستوى الاقليمي. عضو قصيباء الطيني في منطقة الدراسة يتكون من خمس سحنات رئيسية تم تقسيمها بناءً على التراكيب الجيولوجية والخصائص الفيزيائية, وتترتب من أسفل الى أعلى كما في المتكشفات الصخرية كالآتي: سحنة الطين الانشطاري و سحنة الغرين المايكي ذو الحبيبات الناعمة جداً و سحنة الطين المحتوي على آثار حيوية و سحنة الحجر الرملي المحتوي على الهاموكي ذو الحبيبات الناعمة جداً الى الناعمة و سحنة الحجر الرملي المحتوي على الزوايا التخطيطية ذو الحبيبات الناعمة الى المتوسطة. تفسير الأشكال التخطيطية في الصور الجوية سبوت-7 ولاندسات الحرارية أظهر اتجاهين رئيسيين للكسور في منطقة الدراسة: 320° في اتجاه الشمال الغربي و 20° في اتجاه الشمال الشرقي حيث يمكن أن يرتبط الاتجاه الأول بنظام نجد الصدعي والاتجاه الثاني بسلسلة الأنشطة التمديدية التي حدثت في المنطقة العربية بعد تصادم عَمَار. تحليل الكسور في منطقة الدراسة أظهر أن الكثافة الأعلى لها توجد في سحنتي الطين الانشطاري والطين المحتوي على آثار**

حيوية, وعلى النقيض تماماً فان المسافة بين الكسور في هاتين السحنتين هما الأقل بين جميع السجن. الكسور الخطية الجوية والكسور واسعة النطاق هي كسور لا يمكن تحديدها بالسحنات الصخرية وتتعامل مع المنطقة على أساس أنها وحدة ميكانيكية واحدة, بينما الكسور ضيقة النطاق هي كسور يمكن أن تحد بالقواعد الصخرية للسحنات المختلفة وتقترح هذه الصخور عدة وحدات ميكانيكية في المنطقة. خصائص القوة الميكانيكية كمطرقة شميدت ومؤشر نقطة الحمولة وقوة الضغط المحورية ومعامل الحيوية أظهرت قيم عالية في سحنات الحجر الرملي بالمقارنة مع السحنات الأخرى في المنطقة. متكشفات عضو قصيباء الطيني في منطقة الدراسة تم تقسيمها الى خمس وحدات ميكانيكية (وحدة-1 الى وحدة-5) بناءً على كثافة الكسور والخصائص الفيزيائية والميكانيكية. هذه الدراسة يمكن أن تشكل أهمية معتبرة في عمليات تخطيط استكشاف النفط الصخري في باطن الأرض عن طريق تقديم المعلومات عن التصرف الميكانيكي لصخور عضو قصيباء الطيني التابع لمتكون القليبة.

# CHAPTER 1

# INTRODUCTION

## 1.1 Introduction

Qusaiba shale member of Qalibah formation in Saudi Arabia was the first to deposit at the Silurian period, at that time the Arabian plate was of high paleolatitude (Cole, 1994). The plate has gone in a major rotation of about 100° during the period of Silurian to late Carboniferous (Konert et al., 2001) (Fig 1.1).

During early Silurian (Llandovery) period a major phase of global warming took place, and caused the retreat of the late Ordovician glaciers and a huge rise in the sea level. In Saudi Arabia, this period followed the de-glaciation of the late Ordovician and has been represented by Zarga and Sarah Formations. It's considered as an important regional marine transgression, that resulted in the deposition of basal Qusaiba hot shale member (Konert et al., 2001). High sea level and anoxic bottom conditions were the main reasons for the organic-rich shale preservation at the base of the Silurian transgression, this is what called now in Saudi Arabia as the hot shale of Qusaiba (Konert et al., 2001). The marginal areas of the Arabian platform at the Silurian period were characterized by shallow to open marine environments while the platform and along the subsiding intrashelf depression were characterized by deep marine environments (Konert et al., 2001) (Fig 1.2). Regionally, the contact between Qusaiba member and Sharawra member of Qalibah Formation is conformable (Senalp and Al-Duaiji, 2001) (Fig 1.3). From a stratigraphic point of view, Qusaiba member consists of two parts. The lower part is called basal hot shale, it represents type-II organic matter, and it was formed by the Silurian marine transgression, and the upper part is considered to be a coarsening upward pro-deltaic shale (Luning et al., 2000). In general, Qusaiba member was interpreted as delta-toe clays, it consists of light gray to dark gray shales in addition to thin beds of sandstones and siltstones which are distributed over the shales (Luning et al., 2000) (Fig 1.4).

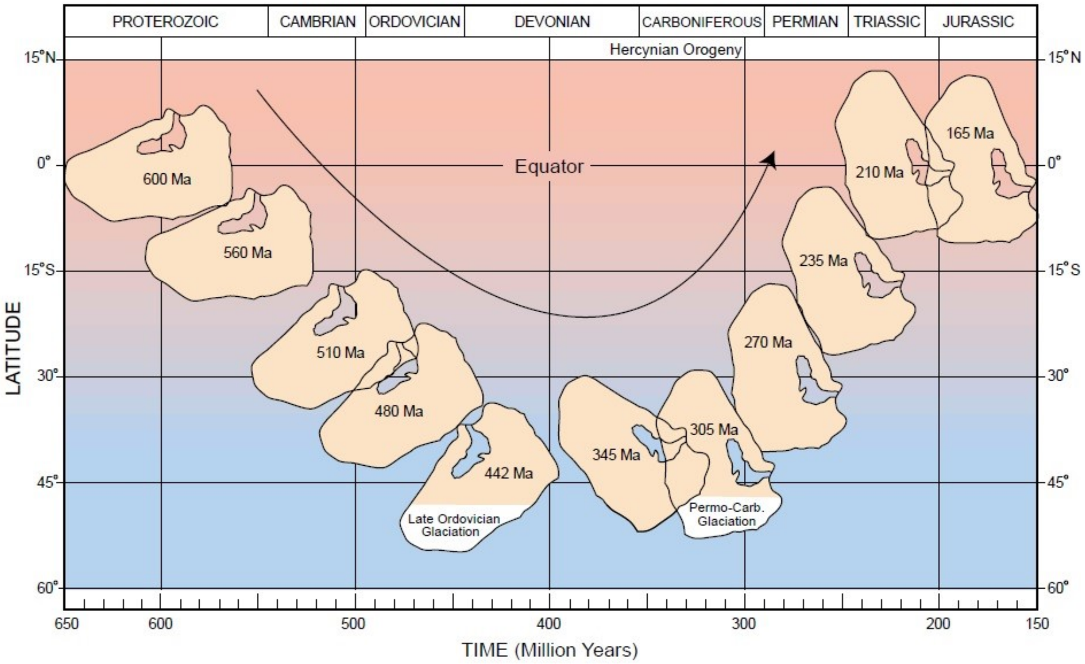

Figure 1-1 Arabian plate paleo-position during Paleozoic era (Konert et al., 2001).

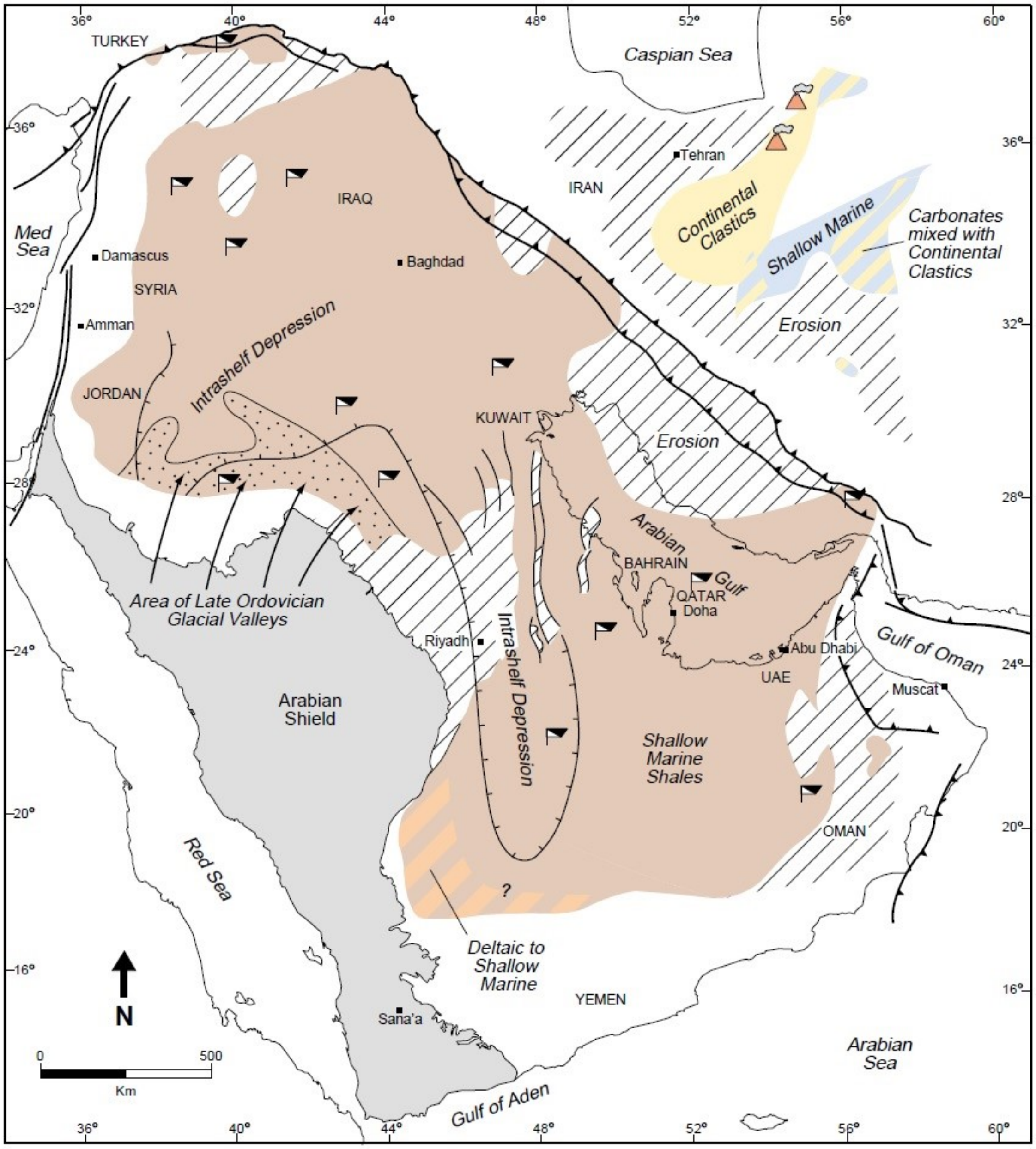

**Figure 1-2 The depositional environments of the early Silurian period in Arabian plate, when Qusaiba shale member was deposited in Saudi Arabia (Konert et al., 2001).**

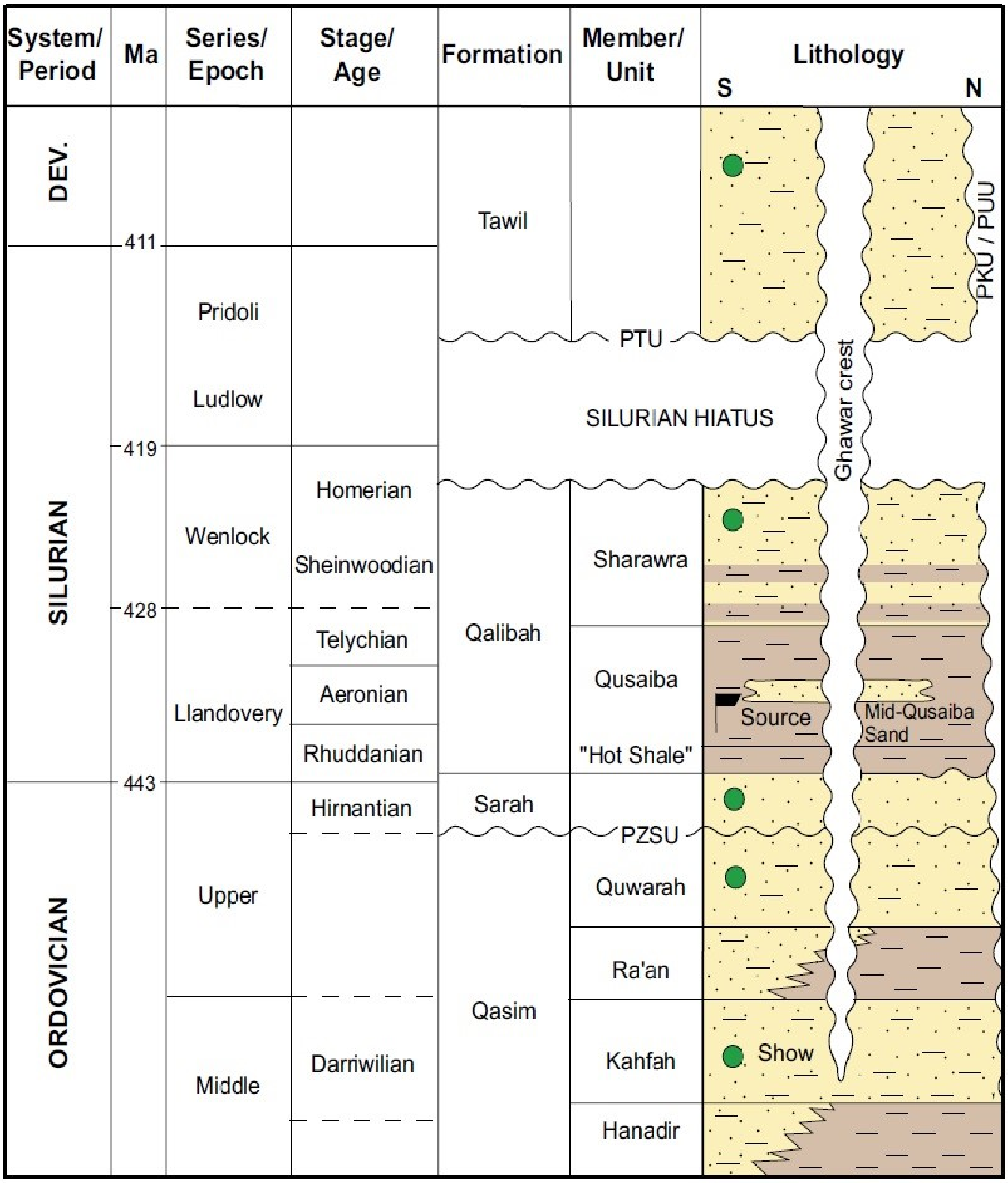

Figure 1-3 A stratigraphical section of east central Saudi Arabia that shows the conformable contact between Qusaiba member and Sharawra member of Qalibah formation (Miller and Melvin, 2005).

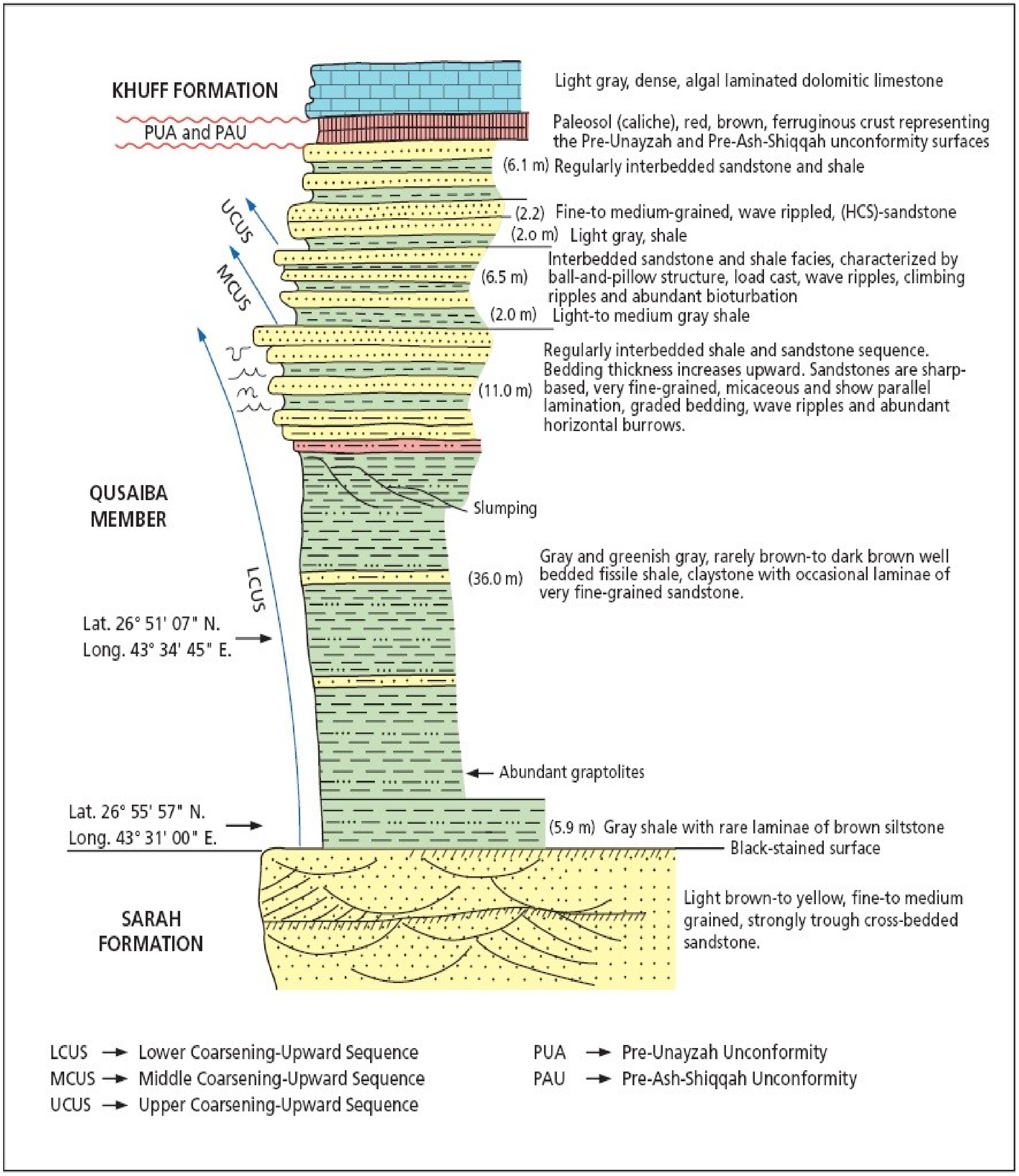

**Figure 1-4 A generalized geological description of the lower and upper part of Qusaiba member of Qalibah formation (Luning et al., 2000).**

## 1.2 Study Area

The outcrops of the study area are located in Central Saudi Arabia to the west of Qusayba village, in Al-Qasim area (Fig 1.5). The exposed rocks of Qusaiba are located in all directions around the coordination: 26°51’50.36” N 43°34’05.95” E, which is the Type section of Qusaiba member of Qalibah formation in Saudi Arabia. (Fig 1.6). This area has been selected because Qusaiba shale member is very well preserved in it, the measurements show that the thickness of Qusaiba shale member in the study area near Qusayba’ village is about 41 meters (Mahmoud et al., 1992). Most of the exposed parts of Qusaiba shale member in the study area are believed to be of the lower part of the member (Fig 1.7) (Grabowski, 2005).

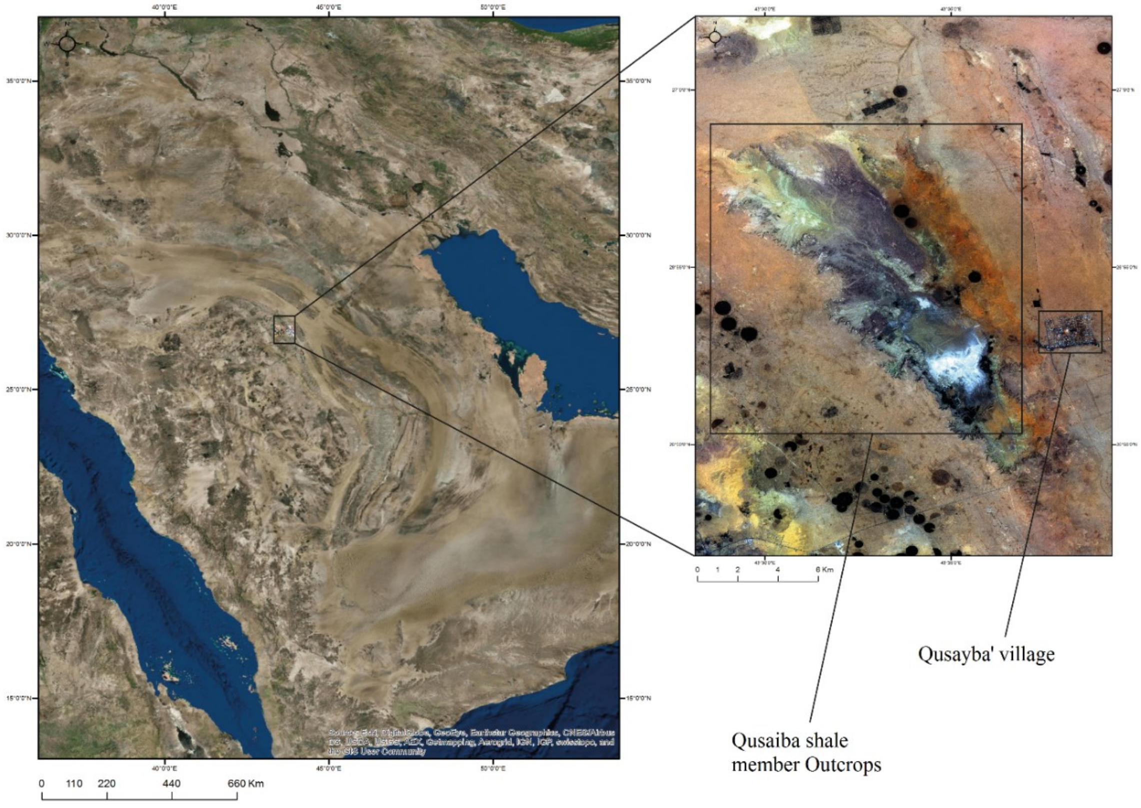

Figure 1-5 Landsat-ETM+ Satellite image shows the location of the study area (Esri, ArcMap).

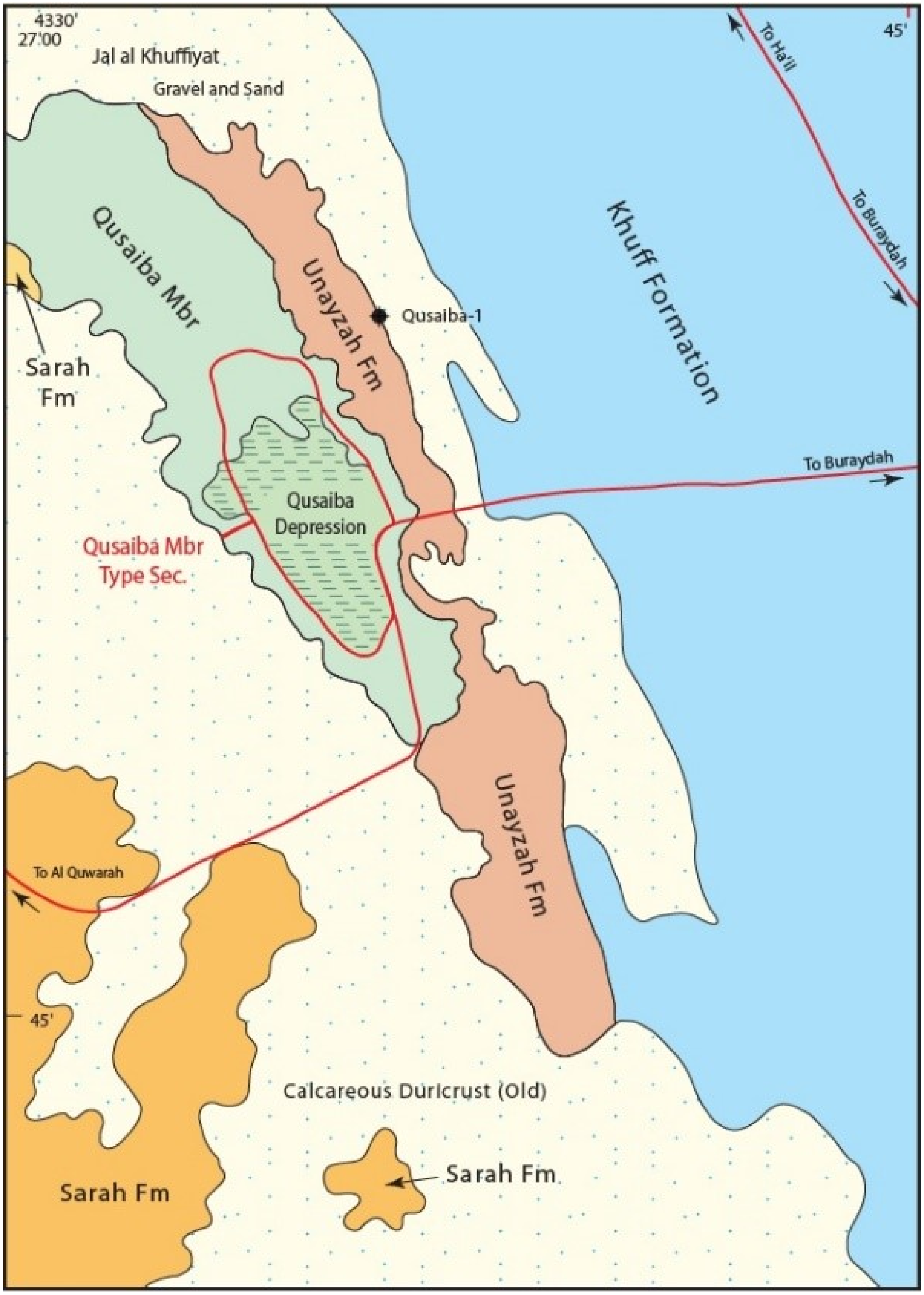

Figure 1-6 Type Section Locality of Qusaiba member in Qusaiba depression - Qasim area, Central Saudi Arabia (Manivit et al., 1986).

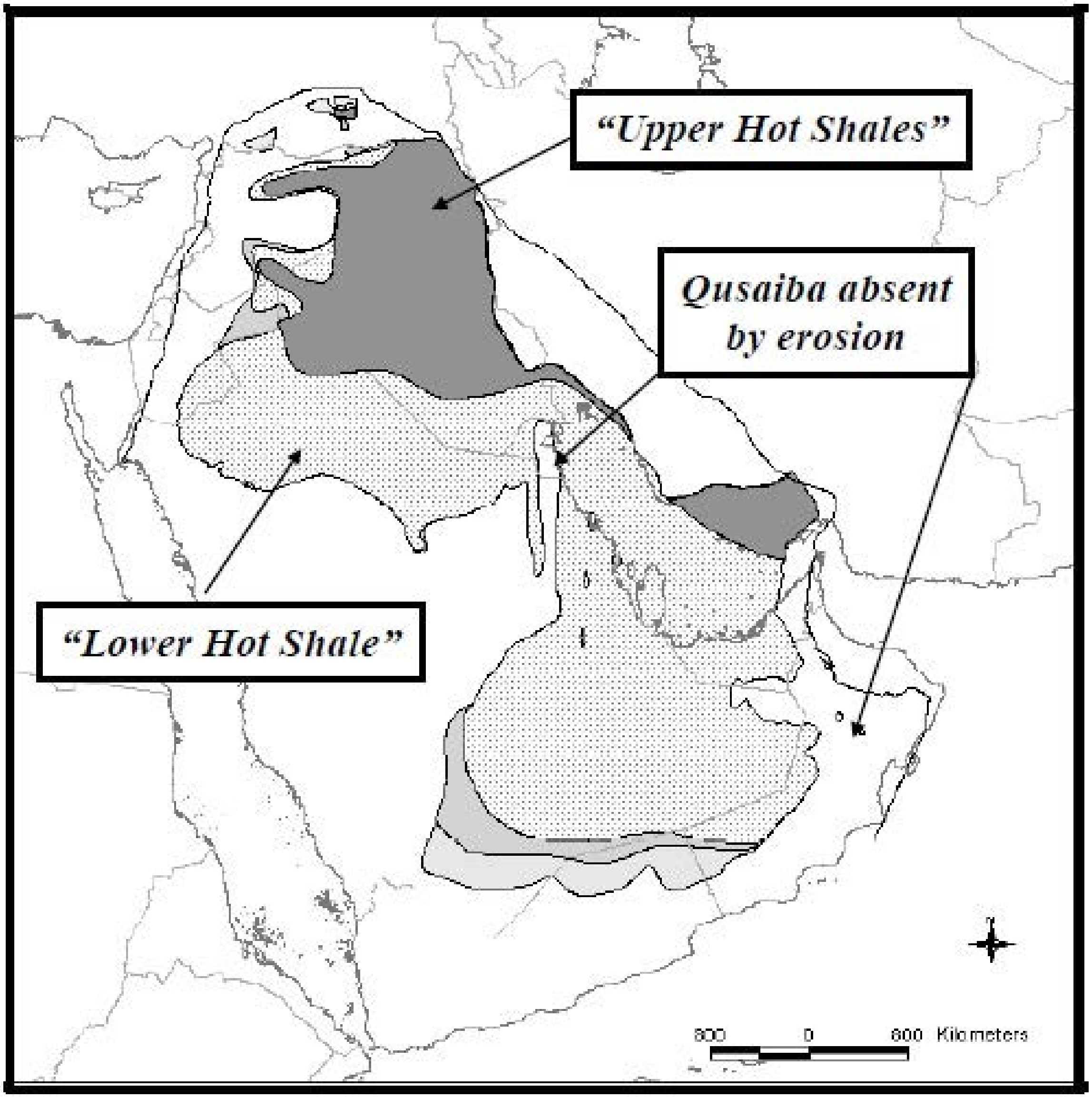

Figure 1-7 Distribution of lower and upper shale of Qusaiba member within Arabian plate, where the study area is located within the lower part of Qusaiba member (Grabowski, 2005).

## 1.3 Problem statement

No previous studies about fractures and/or geomechanical properties were conducted in an outcrop-scale in Qusaiba shale member in Saudi Arabia.

The basal Qusaiba shale member of Qalibah formation is one of the most prolific oil-prone source rocks in the region, it's believed to be the main source rock of the Paleozoic petroleum system in Saudi Arabia. Qusaiba member is also one of the important exploration targets of tight gas in Saudi Arabia as one of the Unconventional resources of petroleum, the studies of Saudi Aramco showed that the reservoir quality of Qusaiba shale is ranging between conventional to very tight (Hayton et al., 2010).

Studying fractures system in terms of distribution, density, trends, spacing, and other fractures characteristics within the member and the effect of the mechanical properties on the fractures behavior in relation to the lithology is considered as a subsurface challenge due to; Scale and Lack of data.

## 1.4 Objectives

- Study the relationships between natural fractures and geomechanical properties in Qusaiba shale member of Qalibah formation, and try to predict the behavior of natural and hydraulic fractures in the subsurface.
- Study the behavior of fractures over different lithofacies, and the effect of lithology on fractures.

## 1.5 Previous studies

The name Qusaiba was first derived by Powers (1986) after the name of Qusayba village, this name was used by Manivit (1986) and many others. Vaslet (1987) considered Qusaiba at that time as a shaly member of what was called Tayyarat formation. Mahmoud and others (1992) replaced the name Tayyarat formation by Qalibah formation and considered Qusaiba shale member one of Qalibah formation members after studying it in Qalibah and Tayma Towns. There are almost no studies that concentrated on the outcrop scale of Qusaiba member regarding the distribution of fractures, Stresses direction and the relationships between geomechanical properties, petrophysical properties, and stratigraphy.

(Cole, 1994) Studied the relationships between the reflectance of Graptolite – Chitinozoan and other maturity indicators from some samples of Qusaiba hot shale member in Saudi Arabia. This study indicated a discrepancy between the Graptolite – Chitinozoan reflectance and vitrinite reflectance, and it was interpreted as a result of the deposition and preservation of the organic matter under specific environmental conditions. (Cole, 1995) Studied the Petroleum geochemistry of Qusaiba shale member, he used saturate fraction biomarkers in addition to carbon isotopes to correlate oil to oil and oil to source. As a result of his study Cole revealed a powerful relationship between oil and the basal part of Qusaiba hot shale member. (Marshall, 1995) Studied the Silurian period deposits in central and northern Saudi Arabia, he defined their burial history, thermal maturity, and geotectonic. Marshall defined from the wells he used in his study some immature Silurian rocks that indicate other areas buried under deep Mesozoic deposits with a younger history of petroleum generation. (jones et al., 1999) Studied the depositional and tectonic settings of Qusaiba hot shale in central Saudi Arabia, they've interpreted the production of the organic-rich facies and claimed that it was produced by the rework and oxidization of the organic-rich sediments, or by the dilution of the organic matter. (Grabowski, 2005) Studied the sequence stratigraphy of the Silurian hot shales in the Arabic region and their distribution, he interpreted the basal shale sequences above the sequence boundaries as low-stand transgressive units. (Miller and Melvin, 2005) Used samples of 34 wells from central Saudi Arabia to develop the biostratigraphy of Qusaiba shale member of Qalibah formation by indicating the acritarchs, chitinozoans, and crypto spores. They've defined some new horizons and related them to sedimentology and sequence stratigraphy. (Al-Laboun, 2009) Explored the Tectonostratigraphy of the Silurian outcrops in Saudi Arabia (Qalibah group) that contains as he mentioned Qusaiba and Sharawra formations. (Faqira et al., 2010) Studied the distribution and characteristics of Qusaiba shale member considering it as a petroleum play, they spotted some light on the role of the Hercynian orogeny on the distribution of the organic-rich member, proved Qusaiba depending on the strong seismic reflectance of it, that indicates high velocity contrasts with the surroundings and indicated many other properties that consider Qusaiba as a prospective shale gas play. (Kanitpanyacharoen et al., 2011) Analyzed the texture and anisotropy of Qusaiba shale member using electron microscopy, ultrasonic velocity, micro tomography, and synchrotron X-ray diffraction measurements. (Craigie, 2016) Used five wells in eastern Saudi Arabia to study the chemo stratigraphy of Qusaiba for correlation purposes. One of the most important results of his study was the use of chemo stratigraphy in identifying Qusaiba mid-sand reservoir in all of the five wells.

## 1.6 Literature review

### 1.6.1 Fractures analysis

Fracture is the general term for all planes along which a rock has lost cohesion. Three major physical properties identify fractures; fractures have two parallel surfaces that meet at the fracture front, the displacement along the planes is relatively small when compared to the length of the fracture, and the surfaces of the fracture are planar (Pollard and Aydin, 1988).

Three principal fracture modes are defined in the literature based on the displacement vector and fracture propagation direction (Fig 1.8). Mode I represent the opening displacement fractures and is perpendicular to the surface of the fracture. Mode II and Mode III represent the shearing displacement fractures, where Mode II fractures are perpendicular, and Mode III fractures are parallel to the surface of the fracture (Nelson, 2001).

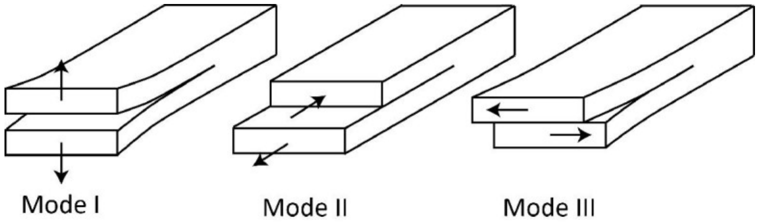

Figure 1-8 The three principal fracture modes.

Mode I fracture are usually described by joints, and Mode II and Mode III fractures are usually described by faults (Pollard and Aydin, 1988).

Regional fracture systems develop over wide areas with almost no change in orientation, they are unaffected by local tectonic events, and they are always perpendicular to the major bedding plane (Nelson, 2001).

Literature shows that the data of the fracture systems in outcrop analogs are commonly acquired from remotely sensed images or fieldwork data in the form of 2D sub-horizontal or sub-vertical maps of fracture traces. Fracture maps are statistically analyzed for specific attributes such as; length, aperture, intensity or spacing, and shape, which can be used to characterize fractures (Odling et al., 1999).

Fracture spacing in a rock mass is controlled by several geological parameters; composition, grain size, porosity, lithological layering, and structural position (Nelson, 2001). The concept of a fractures unit was introduced based on the fact that in well-stratified sequences, fractures are of systematic confinement to a single or a combination of several sedimentary layers (Underwood et al., 2003; Bertotti et al., 2007). Fracture unit is considered to be a package of one or more sedimentary layers with a relatively homogeneous fracture attribute distribution, commonly vertical extent or spacing. Fracture unit thickness is a key component in most models of fracture growth and fracture-pattern development (Laubach et al., 2009).

There are two end-member types of fractures based on the influence of the lithological layers; Strata-bound (Fig 1.9a) and non-Strata-bound (Fig 1.9b). (Odling et al., 1999).

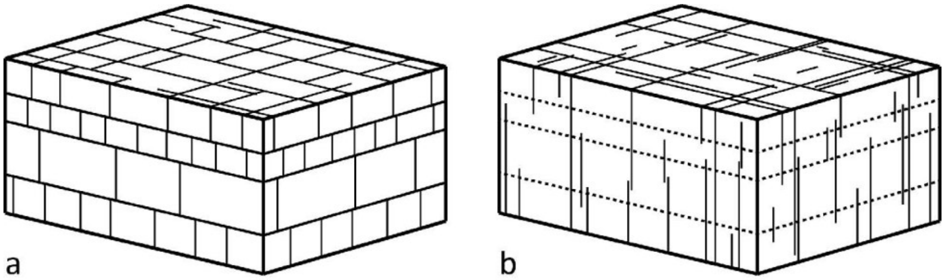

Figure 1-9 Theoretical end-member types of fractures; a) Stratabound. b) Non-Stratabound (Odling et al., 1999).

(Strijker et al., 2012) analyzed fractures from an outcrop analog in a clastic succession in western Jordan. They have used in this study high-resolution satellite images, in addition to the acquired data/photos from the field to be able to study geometry and the characteristics of the fractures system. They have found five sets of fractures in different directions, ranging from small to large scale. At the end, the researchers connected the fractures with the stratigraphy and the geology of the area and designed a three-tier hierarchical model of the fractures to reflect the control of the stratigraphy.

There are several ways to collect data for fracture characterization, the most used methods of data acquisition are; circular scanline sampling, window sampling, and linear scanline sampling. Since the previous methods are more convenience for a homogeneous network of fractures, (Watkins et al., 2015) proposed a new workflow that could be useful in characterizing heterogeneous network of fractures; Augmented circular scanline method. This study has taken place in a thrust belt area, because it’s expected to be a heterogeneous highly fractured area, and a comparison has been done between the first methods and the Augmented circular scanline method.

### 1.6.2 Geomechanical and petrophysical properties

Soil mechanics and rock mechanics are the two main branches of geomechanics, which could be defined as the geologic study of soil and rocks behavior (Jaeger et al., 2009). This study will be concerned more about rock mechanics.

The literature shows several geomechanical studies in different sedimentary rocks; Sandstones, Carbonates, and shales on different scales ranging from microscopic to outcrop scale in both surface and subsurface environments, but no studies have been conducted on Qusaiba shale member of Qalibah formation on an outcrop-scale on the surface.

Recently, producing hydrocarbons from unconventional shale gas reservoirs became more common, it’s important to characterize organic-rich shales such as Qusaiba because geomechanical properties control not only the process of hydraulic fracturing but also the change of the transport properties during production.

(Gao et al., 2014) studied Anisotropy in shale rocks and its mechanical behavior, they used for the study some samples from a shale gas rocks in Ohio, USA. SEM and EDX were obtained to study the chemical composition and microstructures of the shales. They’ve designed three different types of specimens to apply uniaxial compression test, direct and indirect tensile mechanical tests, and wave velocity measurements.

The results of this study showed that the anisotropic shales have complex failure patterns when compared to homogeneous shales, the tensile strengths of the specimens are influenced by the interlaminar failure along the bedding planes, and the shear wave speed is always low when it’s directed perpendicular to the bedding plane.

(Ameen et al., 2009) used representative samples from Ghawar oil field to study some geomechanical properties and their relations in the Arab-D reservoir. They've correlated porosity (physical property) to Vp, Vs, internal friction angle, and static and dynamic constants (mechanical properties). They were success to get a good correlation after designing a pseudo logs using sonic velocity logs and experimental laboratory logs

They've subdivided Arab-D reservoir based on mechanical properties and proved that the mechanical layering subdivision is more efficient with higher resolution than the stratigraphical zonation. Their conclusion on this study was the fact that mechanical properties can be affected not just by porosity but also by some other factors such as mineralogy and texture of rocks.

(Hsieh et al., 2008) Studied the relationships between sedimentological properties (Petrographic parameters) and mechanical behavior of sandstone rocks. They've used pounded particles method to design a simulation of how sandstone would behave on the macro scale under specific conditions. They've claimed that the uniaxial compressive strength in sandstones is inversely proportional to petrographic parameters, unlike the Young modules which is directly proportional to the same petrographic parameters, they concluded this result after conducting an experiment that resulted in constructing two plot diagrams to explain the relationships between uniaxial compressive stress (UCS) and petrographic parameters (GAR), and Young modules (€) and petrographic parameters (GAR) with the presence of porosity in both cases.

(Abdullatif, 2010) applied Rock mass rating (RMR), and Quality index (QI) to investigate some geomechanical properties in lower and middle parts of Rus formation in Dammam dome. RMR and QI are considered to be a rating systems that could be correlated with each other using many parameters such as; Uniaxial compressive strength (Point load), joint roughness, alteration, orientation and spacing in the field, and Young modules, Schmidt hammer rebound number and Poisson ratio in the laboratory. He plotted samples from both middle and lower Rus formation to show the relationships between Quality index and Rock mass rating. His results showed that lower Rus formation has a lower Quality index and Rock mass rating than middle Rus formation, after that he conducted some laboratory experiments to confirm this result.

(Arman et al., 2012) studied calcite, dolomite, quartz, and clay minerals samples from lower Oligocene Asmari formation in UAE, these samples were affected by many diagenetic processes that affect the mechanical properties. The results of the study showed that the samples with higher dolomite percentage have more strength, and the samples with higher calcite percentage have less strength. In addition to that (Arman et al., 2012)

investigated the geomechanical results and tried to correlate them, one of their conclusions was that Schmidt hammer is weakly related to indirect tensile strength, ultrasonic wave velocity, and point load index and the unit weight of the rocks showed weak to moderate correlation with the uniaxial compressive strength

(Kharusi, 2009) conducted a study in Middle Mississippian carbonates of St. Louis basin and Paradox basin in Wyoming, Utah. She correlated between a high-resolution sequence stratigraphy model and a mechanical model for an enhanced fracture characteristics prediction of an anticlinal structure.

The results of this study included many geomechanical measurements; Bulk modulus, Young's modulus, Poisson ratio, rigidity ratio, and velocity. In addition to that some statistical readings; fractures density, fractures intensity, and fractures spacing ratios, and petrophysical; Grain density, and porosity.

The conclusion of her study stated that the genetic boundaries of higher order sequences act as a mechanical boundary also, but the single mechanical unit can include more than one stratigraphic/lithological unit. She stated also that the fractures parameters can be affected by some of the bedding characteristics such as; bed thickness, and bed forms, but at the same time not affected by rock stiffness, porosity, or lithology.

(Alikrami et al, 2013) studied the geostatistical relationships in the deformed sandstone of Entrada, Utah between the physical and geomechanical properties; Uniaxial compressive strength and Young modules versus permeability, and Schmidt hammer readings versus Tiny-perm II measurements. The results of statistics in this study showed that the relationships between physical and geomechanical properties depend on calcite cementation to quartz sandstone degree and on deformation processes.

# CHAPTER 2

# Methodology

In order to achieve the objectives of this research, the following methods have been used.

## 2.1 Satellite images Analysis

Two high-resolution satellite images have been used in order to trace straight and slightly curved lineaments in the study area. Spot-7 satellite image (1572 × 1193 Pixel²) (42km²) (Figure 7) has been used to trace regional-scale lineaments of >1500m (Qusaiba member, Sara formation, and Unayzah formation), where more than 120 lineaments have been interpreted, and Landsat-ETM+ satellite image (1700 × 2200 Pixel²) (5.4km × 8.1km) (Figure (8) has been used to trace lineaments of <1500m (Qusaiba member outcrops), where more than 200 lineaments have been interpreted. The satellite images were interpreted in a GIS media using ArcMap10.2 and ArcCatalog10.2 software by tracing the line features within the images, and calculating the length and orientations of the lines. The main goal of using satellite images is to define the general orientations of the tectonic-generated fractures and their characteristics.

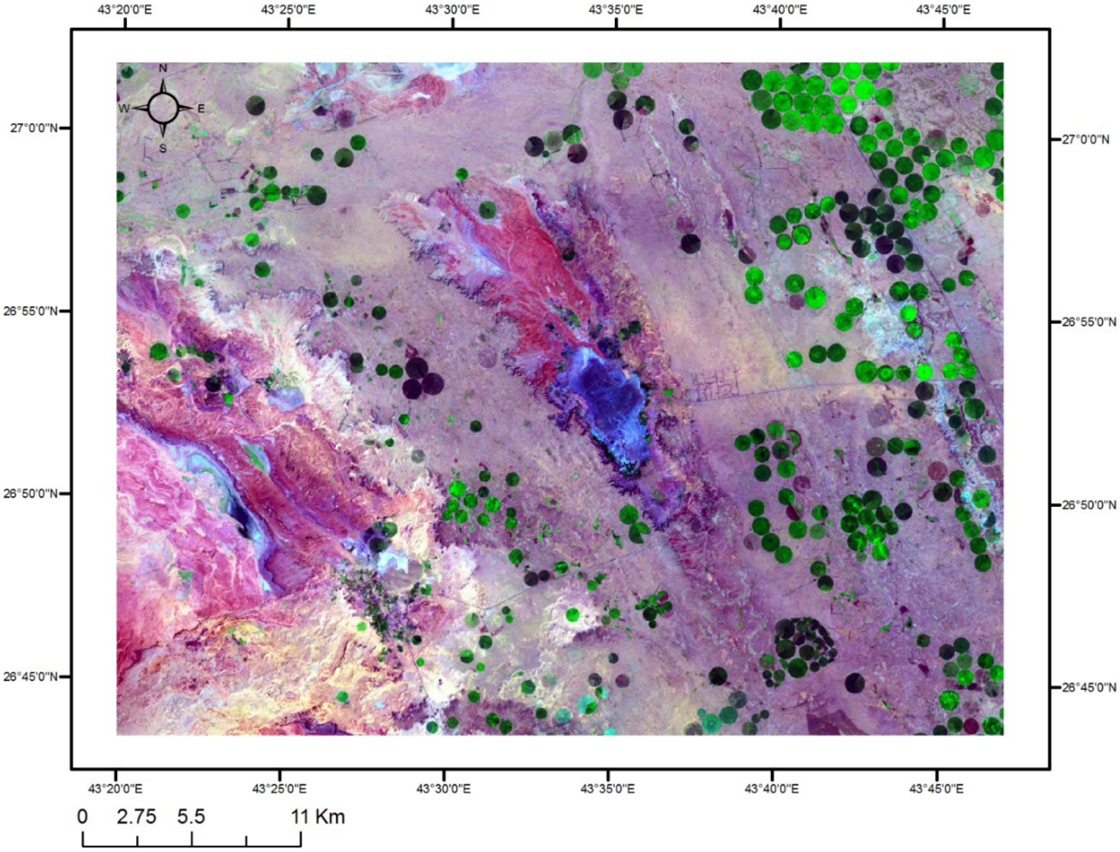

Figure 2-1 Spot-7 satellite image of the study area showing the outcrops of Qusaiba shale member, Unayzah Formation and Sarah Formation.

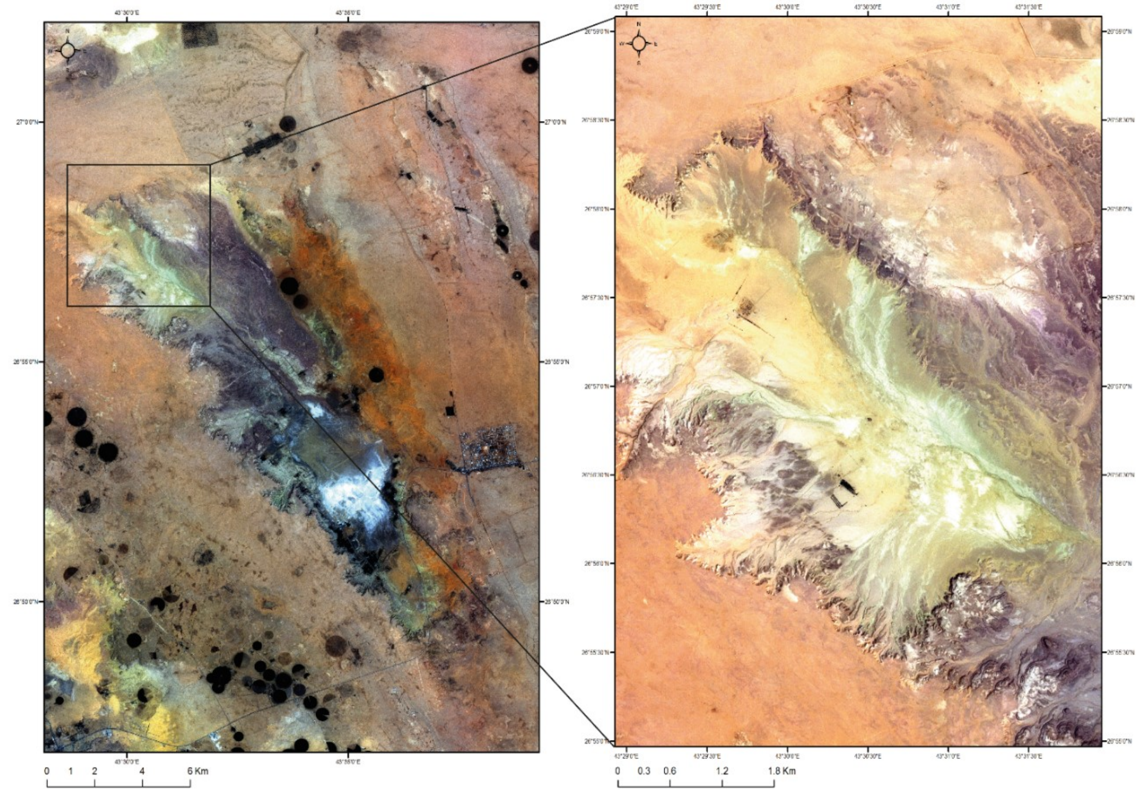

**Figure 2-2 Landsat-ETM+ satellite image of the study area showing the outcrops of Qusaiba shale member of Qalibah Formation.**

## 2.2 Field investigations

Field investigations have taken place on the cropped rocks of Qusaiba shale member of Qalibah formation in Central Saudi Arabia, to the west of Qusayba village in Al-Qasim area. Two outcrops have been selected in order to describe the different lithologies of Qusaiba member, study the fractures system within them, and collect samples for further laboratory measurements. The first outcrop is located near the coordination (26°56’23.1” N 43°31’55.6” E). The height of this outcrop is about 40 meters. (Fig 2.3). The second outcrop is located near the coordination (26°55’40.8” N 43°30’55.2” E). The height of this outcrop is about 22 meters. (Fig 2.4). Detailed stratigraphic description was conducted along the selected outcrops in order to create vertical stratigraphic sections that describe the vertical changes of the lithofacies. Spectral gamma ray tool has been used in the field to measure Gammas natural radiation that emits from the rocks, in order to detect the small variations of the lithofacies and to clarify the depositional cycles of the member. Schmidt hammer has been used along the outcrop in a vertical succession to measure the rebound number (Rn) of different lithologies, which indicates the strength of them. Fractures have been studied along the two outcrops and the area around them. Several parameters were observed and measured using scan-line method. these parameters are; fractures trend/strike, fractures scale/length, fractures density, fractures termination degree and fractures spacing.

Figure 2-3 . Outcrop-1 from the study area 40m (26°56’23.1” N 43°31’55.6” E).

Figure 2-4 Outcrop-2 from the study area 20m (26°55’40.8” N 43°30’55.2” E).

## 2.3 Laboratory measurements

60 rock samples have been collected from the two outcrops in the field. Thin sections, cores/plugs, cubes, small deformed pieces, grinded powder were taken from the rock samples. Cores/Plugs were used in measuring Porosity and Ultrasonic wave velocity (Vp). Cubes were used in measuring the strength of the rocks through Point load and Uniaxial compressive strength. Small deformed pieces were taken from the rock samples in order to conduct Scanning electron microscope (SEM) images. Grinded powder of the rock samples was used in X-ray fluorescence (XRF), and X-ray powder diffraction (XRD). The laboratory measurements that were discussed here have been carried on to help in defining different lithofacies types and geomechanical properties.

## 2.4 Methodology and preliminary results of the 3D Geostatistical modeling.

In order to construct a 3D geostatistical facies Model, 12 locations of outcrops were described based on Qusaiba shale member depositional cycles that were found in the study area, in addition to the two main outcrops. The continuity of the layers, the coordinates, and the thickness of each layer were examined in the field (Fig 2.5). Spatial correlation between the 14 stratigraphic sections was conducted using Petrel 2009 software (Fig 2.6). The surfaces of the model were defined based on the depositional cycles of Qusaiba shale member and divided the 3D model into 3 zones (Fig 2.7). Layering criteria of the 3D model was selected based on the minimum thickness of a layer in each zone, therefore, the layering was as follow: zone-1; 46 layers, zone-2; 21 layers, and zone-3; 80 layers. 3D gridding of the model was defined based on the outcrops area (2km × 1km), therefore, the cells (nI × nJ × nK) values were: (78 × 73 × 147) (Fig 2.8). The trends in the data set were determined by constructing semivariograms (Major, minor, and vertical) for each zone (Table 2.1), (Fig 2.9), (Fig 2.10), and (Fig 2.11). Sequential indicator simulation was used to model zone-2 and zone-3 and truncated Gaussian simulation was used to model zone-1. (Amour et al., 2012) suggested that the sequential indicator simulation (SIS) is the best algorithm to simulate the distribution of the mosaic-like lithofacies, since it allows to assign different semivariograms for different sedimentological lithofacies, and that's why (SIS) can capture even small changes in geological properties and depositional environments. Sequential Indicator Simulation (SIS) is one of three sequential procedures that use for different types of data the same algorithm, (SIS) uses the methodology of Sequential Gaussian simulation (SGS) to develop a gridding plan of ones & zeros. The process of Sequential Indicator Simulation as mentioned from the literature could be described as follow: (1) Normalizing the raw data. (2) choosing a node that hasn't been simulated yet. (3) Estimating the local conditional probability distribution function (lcpd) at the exact location of the node that was selected in the previous step (4) Summing the transformed data mean and the residual value in order to create a simulated value. (5) adding the new value from the previous step to the data with a specific short-scale correlation. (6) Repeating the previous steps for the rest of the nodes.

(White et al., 2003, Benson et al., 2014) suggested that the Truncated Gaussian Simulation (TGS) follows Walter's concept when simulating lithofacies models, and uses one semivariogram for different lithofacies. Truncated Gaussian Simulation (TGS) uses Truncated Gaussian algorithm that develop a group of cutoffs to partition the field to simulate the lithofacies, (TGS) works perfect with transitional facies, such as the facies that were found in the study area of Qusaiba shale member.

After generating the 3D geostatistical facies model, values of porosity, fractures density, point load index, and other geomechanical properties were assigned as values in the lithofacies model.

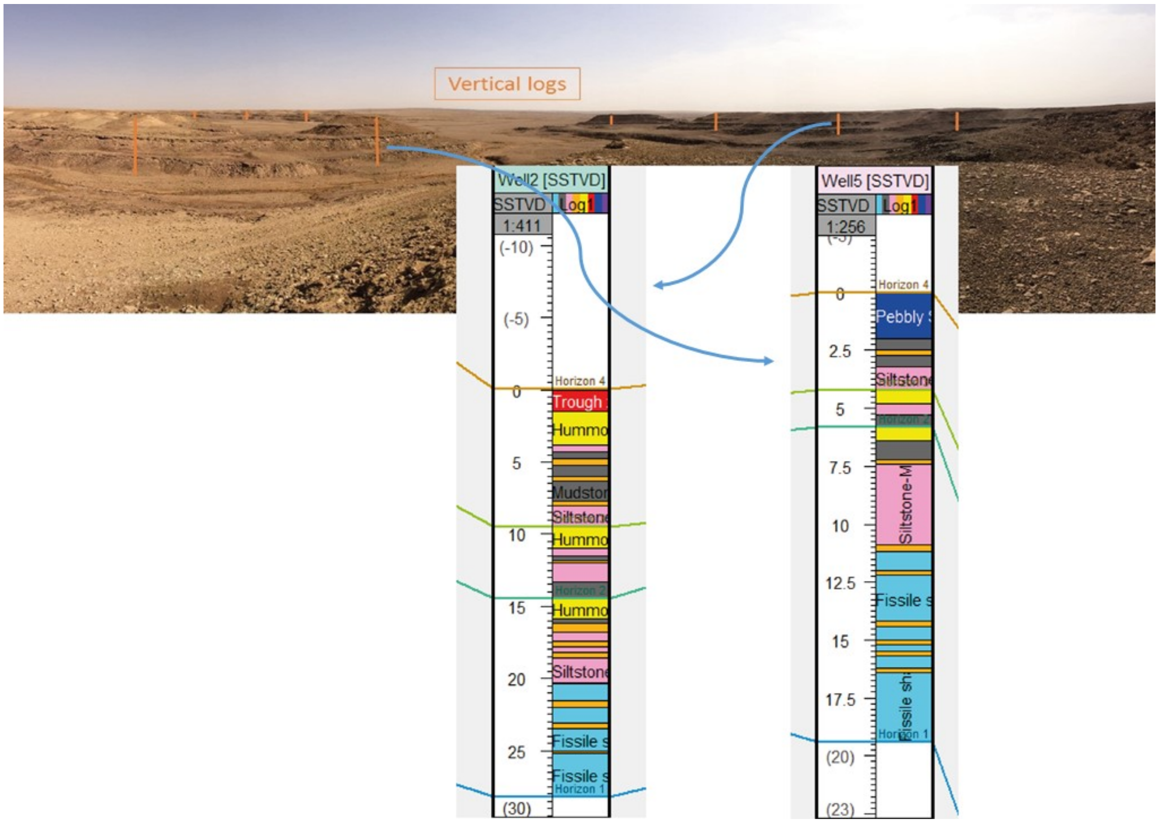

Figure 2-5 Outcrop photograph showing some of the described vertical lithostratigraphic sections, and an example of two logs with the detailed lithofacies description.

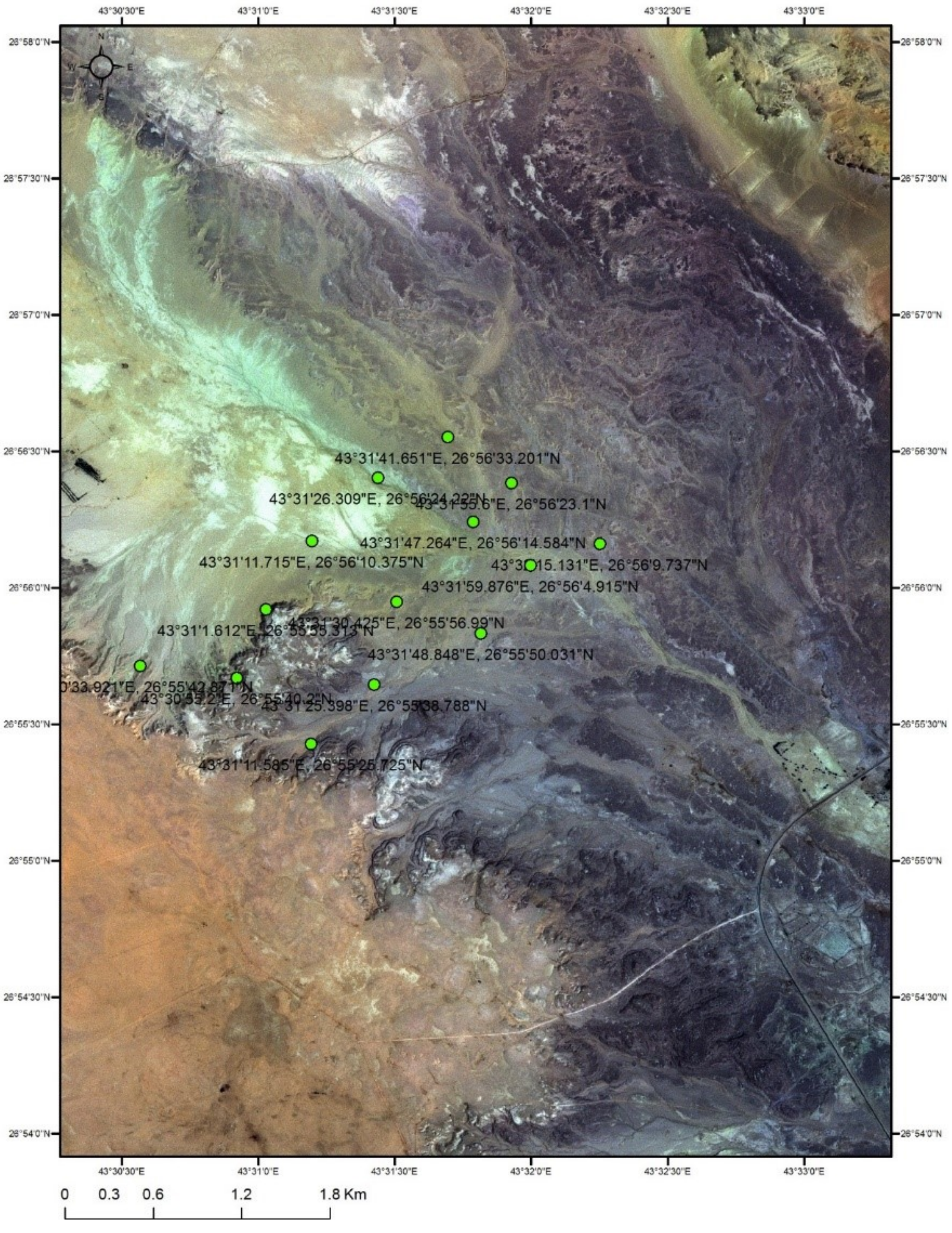

**Figure 2-6 Spot-7 satellite image showing the coordinates of the 14 vertical logs from the study area that were used in the 3D geostatistical modeling.**

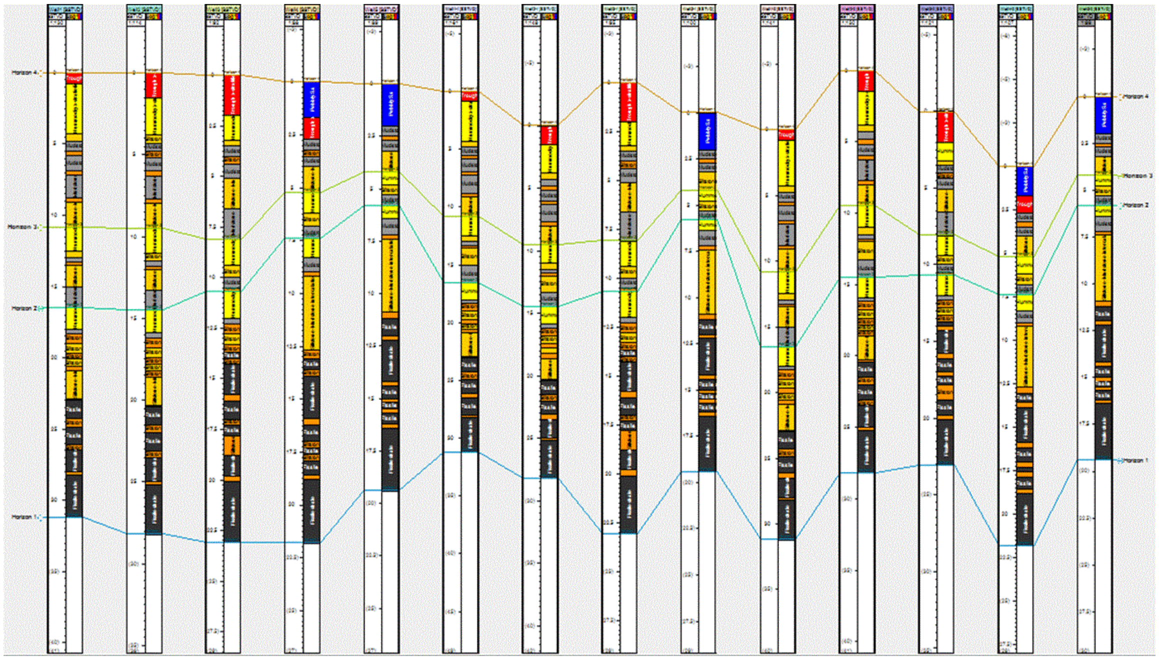

**Figure 2-7 Correlation between vertical logs based on 3 depositional cycles of Qusaiba shale member in the study area (Petrel 2009).**

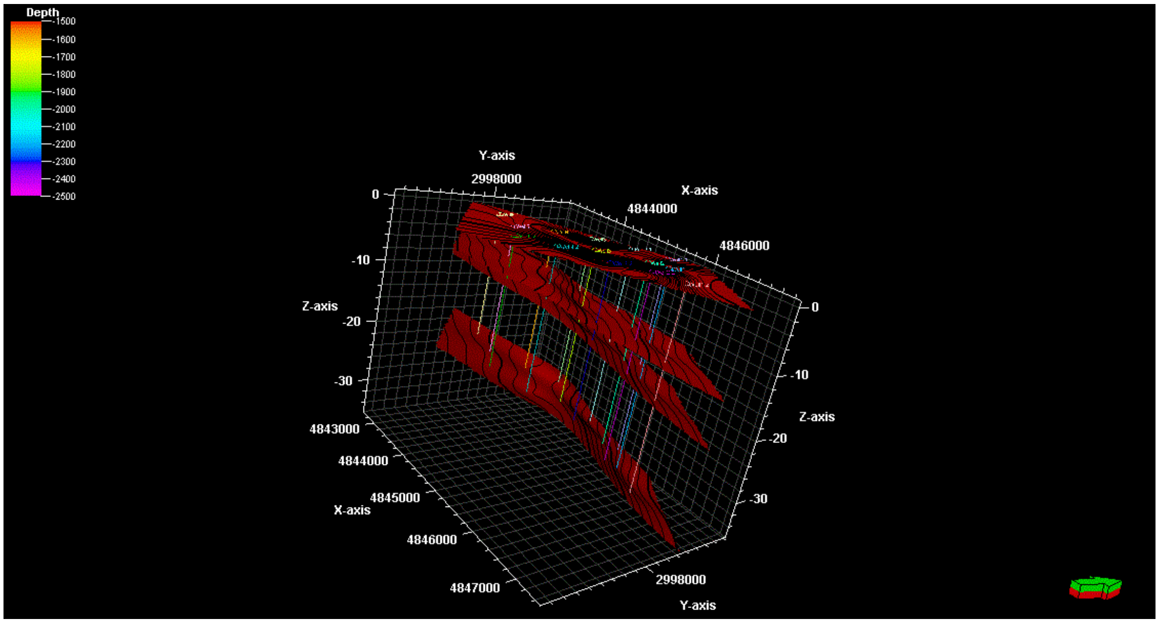

**Figure 2-8 Surfaces of the 3D model that divides it into 3 depositional zones.**

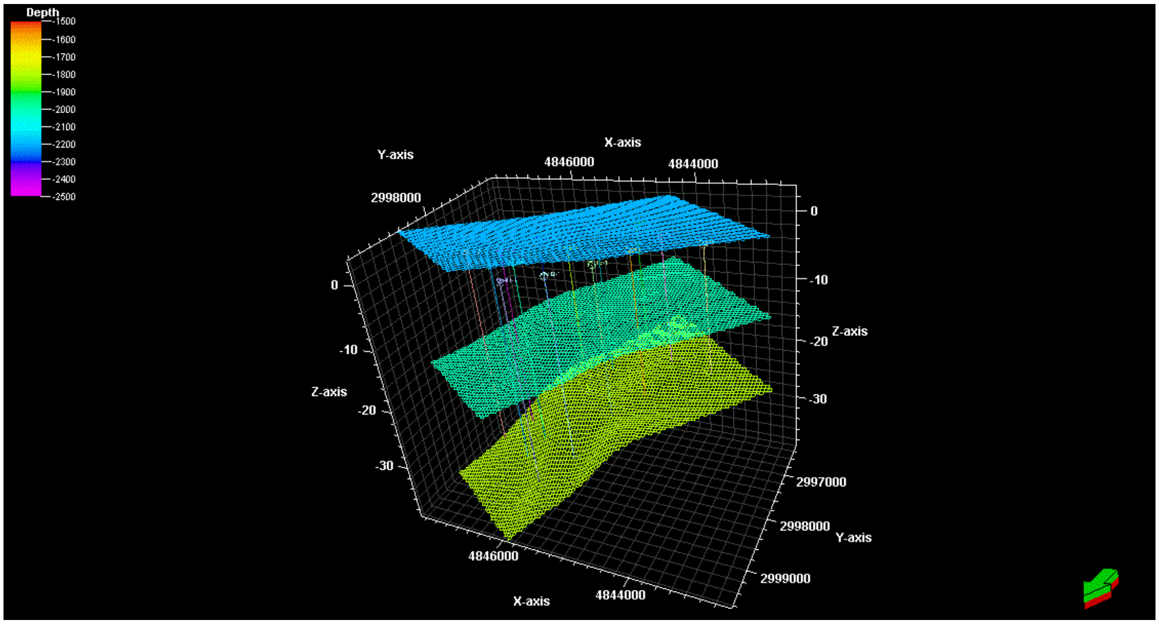

Figure 2-9 Top, middle, and base gridded surfaces of the 3D model (nI=78 × nJ=73 × nK=147).

Table 2-1 Results of the Semivariograms parameters of the three depositional zones.

| Zones | Major range | Minor range | Vertical range | Nugget | Sill | Model type |
|---|---|---|---|---|---|---|
| Zone-1 | 1200 | 557 | 1.5 | 0 | 1 | Spherical |
| Zone-2 | 1060 | 561 | 1.6 | 0.2 | 1 | Exponential |
| Zone-3 | 964 | 396 | 3.2 | 0.3 | 1 | Spherical |

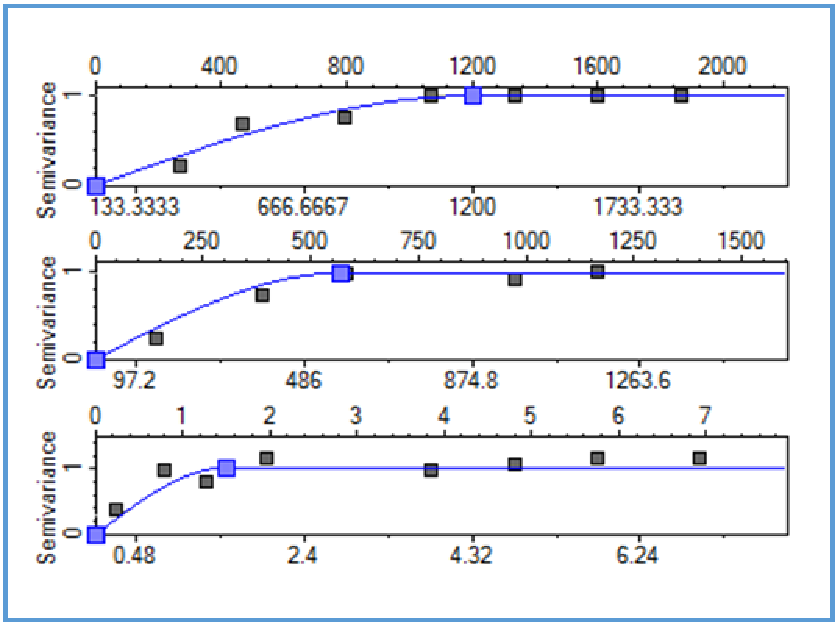

Figure 2-10 Major, minor, and vertical semivariograms of zone-1. Major semivariogram: (Direction: NE-SW, Tolerance angle: 67°, Lag tolerance: 50%, Lag distance: 292.6m). Minor semivariogram: (Direction: NW-SE, Tolerance angle: 42.7°, Lag tolerance: 50%, Lag distance: 197.3m). Vertical semivariogram: (Tolerance angle: 32.7°, Lag tolerance: 50%, Lag distance: 0.8m).

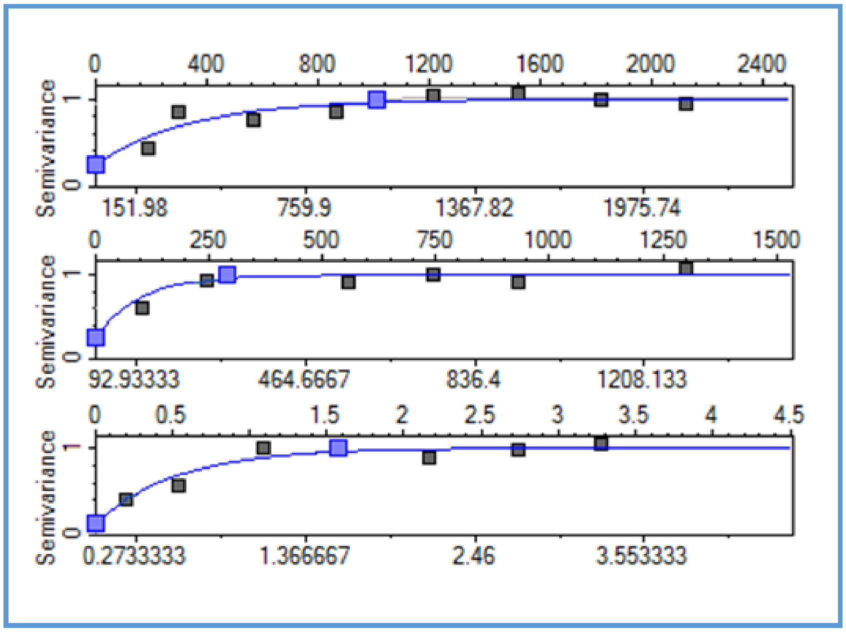

Figure 2-11 Major, minor, and vertical semivariograms of zone-2. Major semivariogram: (Direction: NE-SW, Tolerance angle: 67°, Lag tolerance: 50%, Lag distance: 292.6m). Minor semivariogram: (Direction: NW-SE, Tolerance angle: 42.7°, Lag tolerance: 50%, Lag distance: 197.3m). Vertical semivariogram: (Tolerance angle: 32.7°, Lag tolerance: 50%, Lag distance: 0.5m).

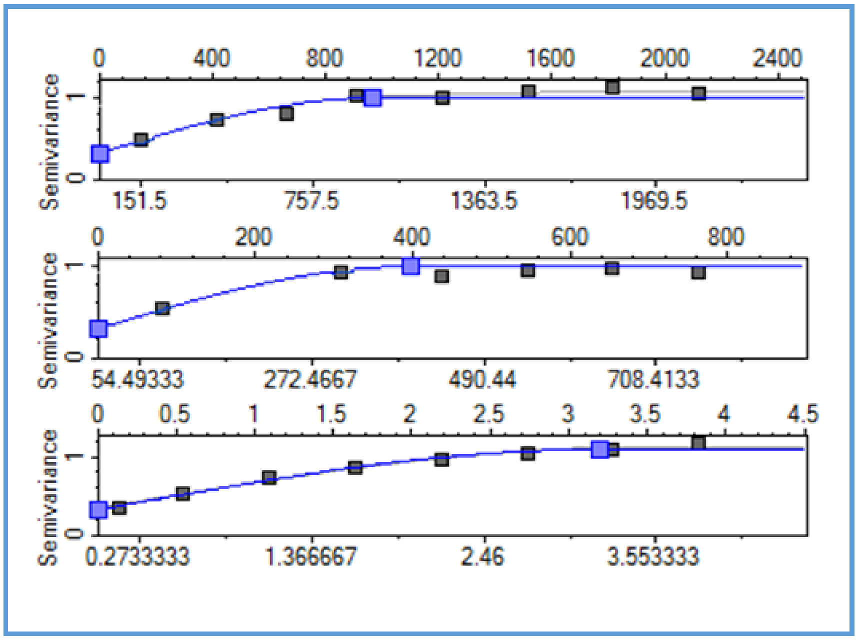

**Figure 2-12 Major, minor, and vertical semivariograms of zone-3. Major semivariogram: (Direction: NE-SW, Tolerance angle: 67°, Lag tolerance: 50%, Lag distance: 292.6m). Minor semivariogram: (Direction: NW-SE, Tolerance angle: 42.7°, Lag tolerance: 50%, Lag distance: 197.3m). Vertical semivariogram: (Tolerance angle: 32.7°, Lag tolerance: 50%, Lag distance: 0.5m).**

# CHAPTER 3

# Sedimentology and lithofacies description

## 3.1 Vertical lithostratigraphic sections

Outcrop-scale studies provide high visual and physical resolution and make it possible to witness the changes in facies, sedimentary structures, and depositional cycles (Biswas, 1999). Two lithostratigraphic sections were constructed (Fig 3.1) and (Fig 3.2) based on the detailed vertical description of two outcrops of Qusaiba shale member in the study area, these outcrops represent three depositional cycles, where each cycle starts with fissile shale and/or mudstone and ends with very fine to fine-grained hummocky cross-stratified sandstone and/or fine to medium-grained low/high angle cross-stratified sandstone. The lowermost part of all outcrops in the study area consists of thick units of fissile shale, and the uppermost part of all outcrops in the study area consists of a recent thick layer of limestone, that overlain Qusaiba member in an unconformity base.

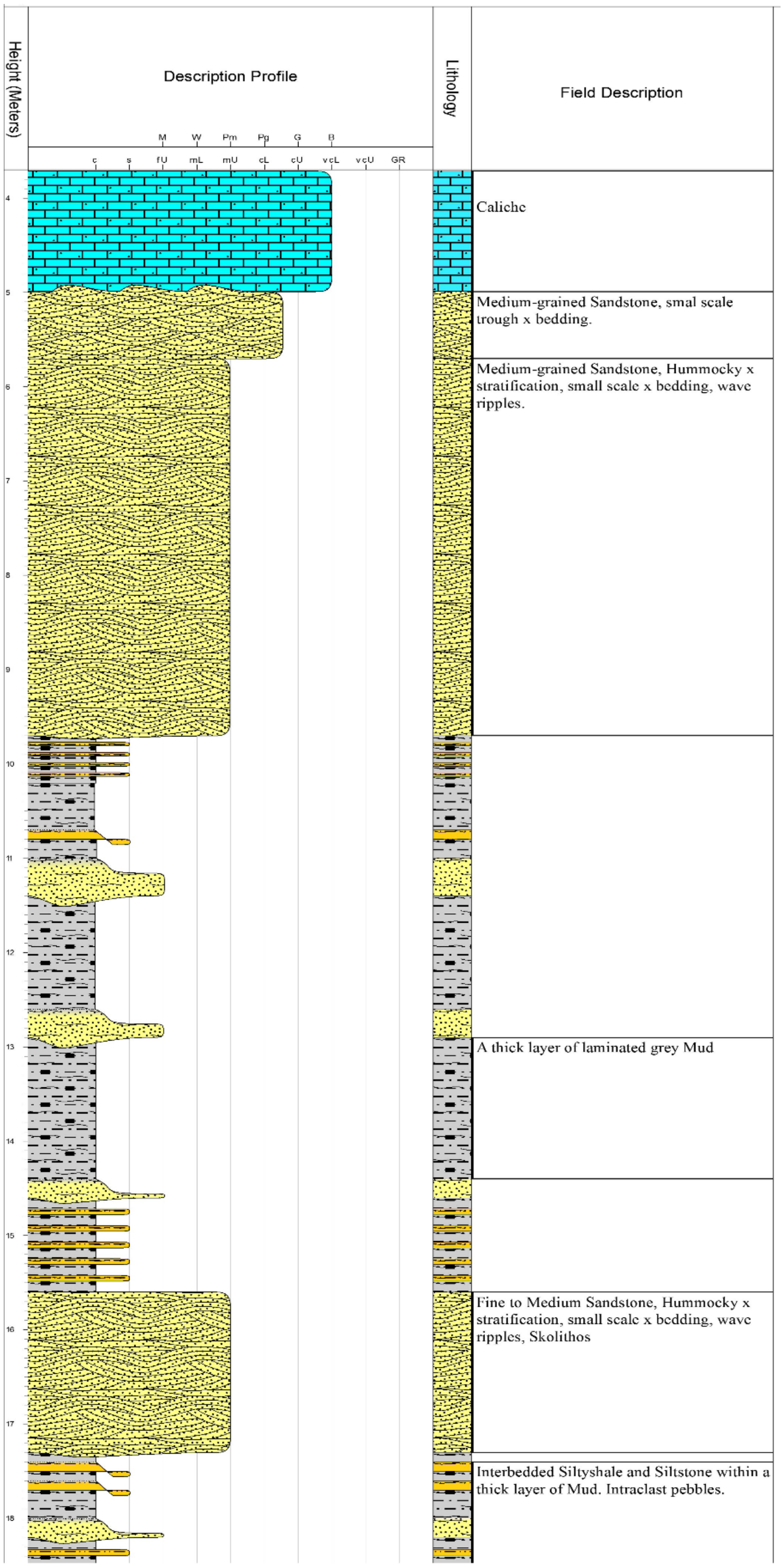

Caliche

Medium-grained Sandstone, smal scale trough x bedding.

Medium-grained Sandstone, Hummocky x stratification, small scale x bedding, wave ripples.

A thick layer of laminated grey Mud

Fine to Medium Sandstone, Hummocky x stratification, small scale x bedding, wave ripples, Skolithos

Interbedded Siltyshale and Siltstone within a thick layer of Mud. Intraclast pebbles.

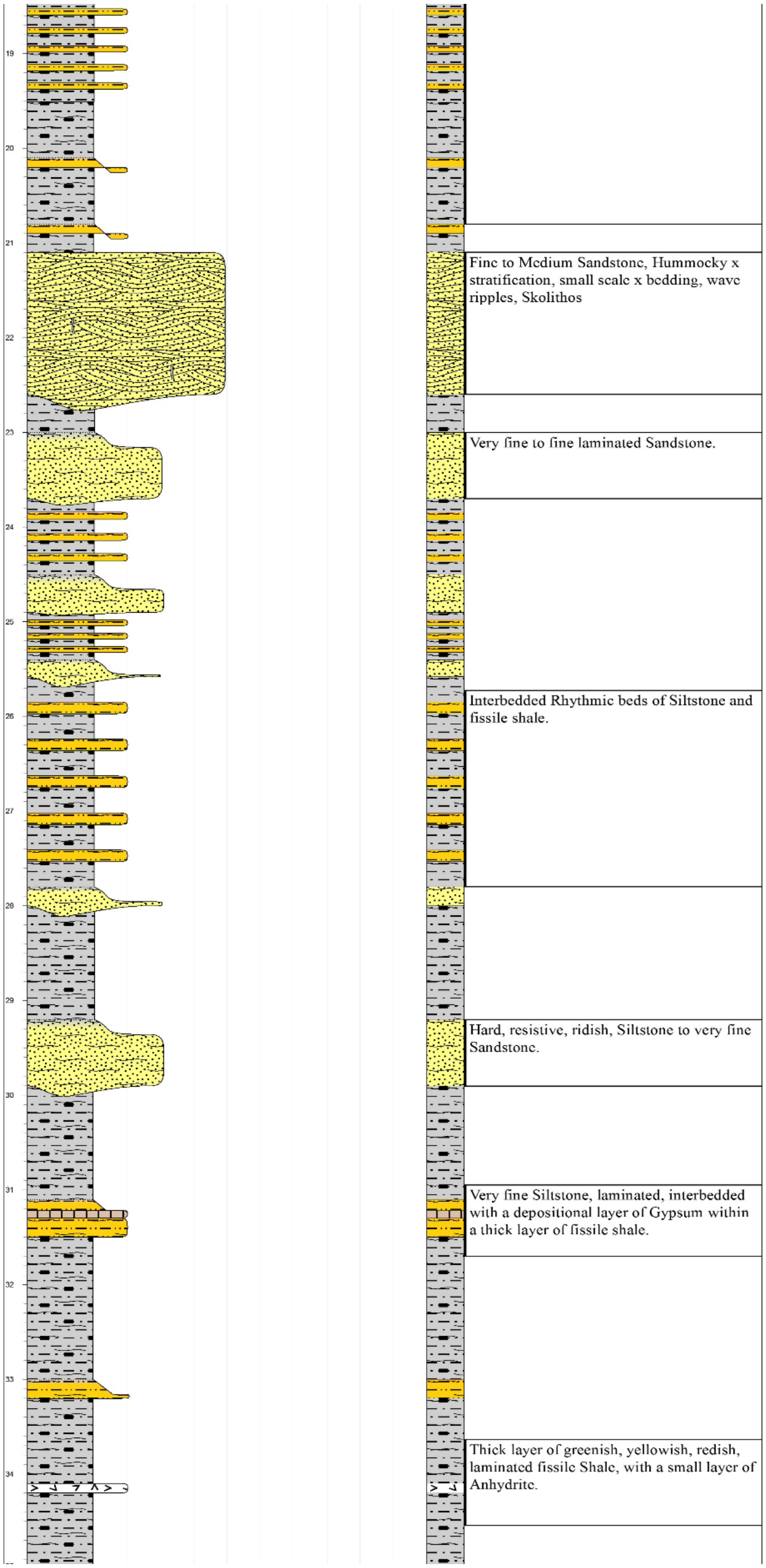

Figure 3-1 Vertical lithostratigraphic section of locality-1 showing the various lithofacies and sedimentary structures.

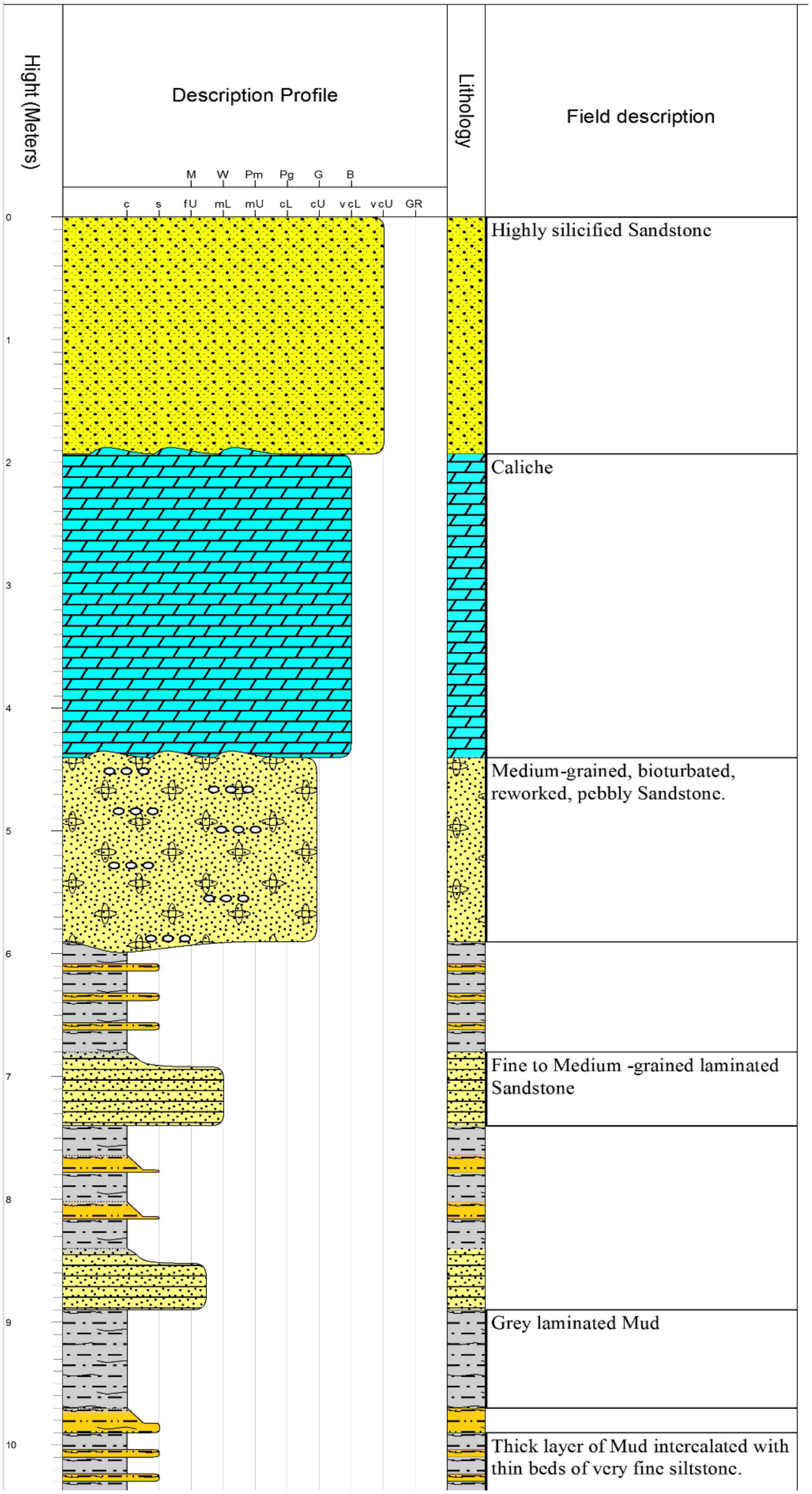

Highly silicified Sandstone

Caliche

Medium-grained, bioturbated, reworked, pebbly Sandstone.

Fine to Medium -grained laminated Sandstone

Grey laminated Mud

Thick layer of Mud intercalated with thin beds of very fine siltstone.

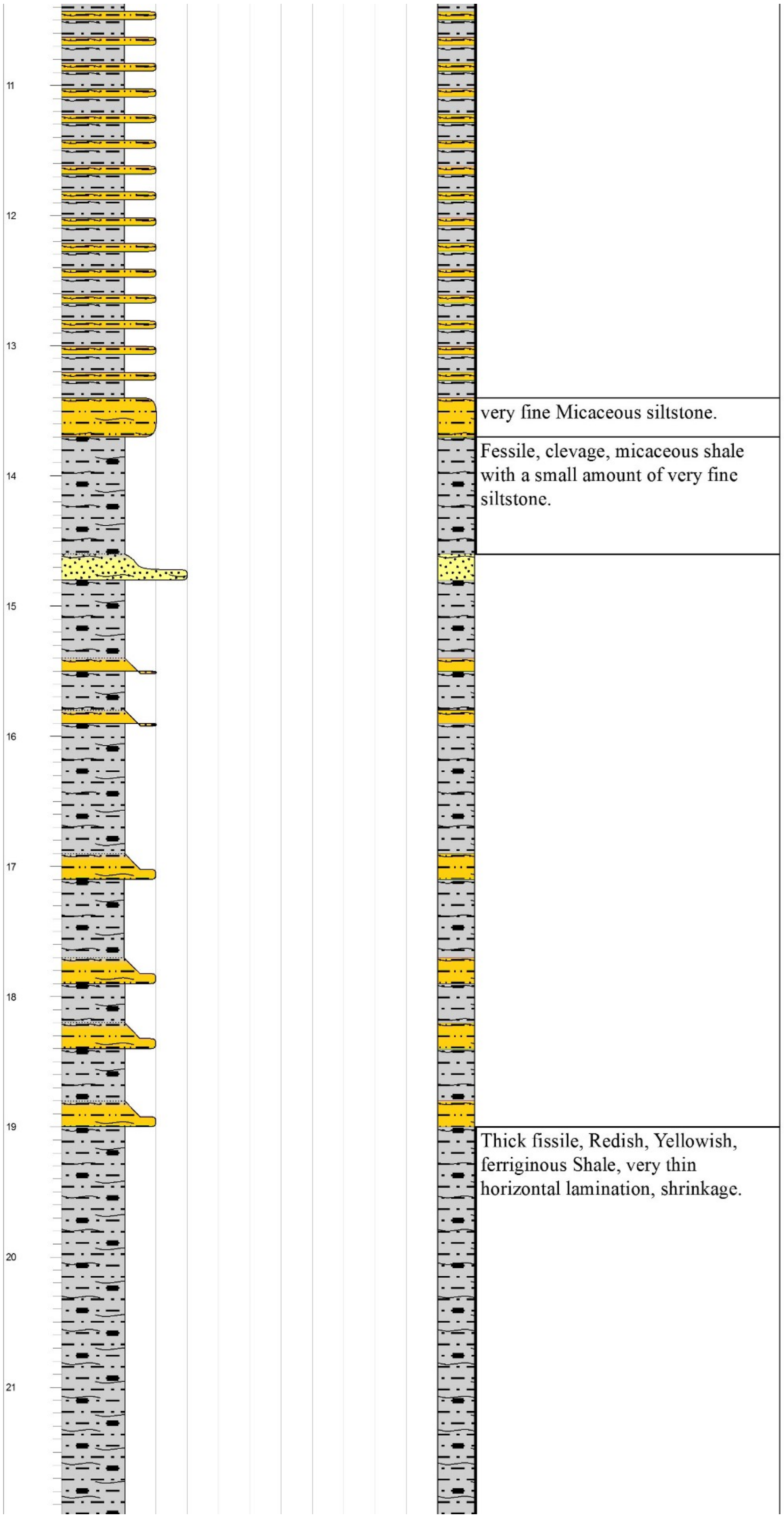

**Figure 3-2 Vertical lithostratigraphic section of locality-2 showing the various lithofacies, and sedimentary structures.**

## 3.2 Lithofacies description

According to lithological and petrophysical properties, the sedimentary facies in the study area were subdivided into 5 main lithofacies.

### 3.2.1 Fissile shale lithofacies

Fissile shale lithofacies is located in the basal parts of the outcrops in the study area. These laminated thinly bedded thick units of shale are characterized by their dark greenish, brownish and reddish colors (Fig 3.3). Thin siltstone layers are found interbedded with the fissile shale lithofacies. The thickness and density of the siltstone layers increase as we move up in the section (Fig 3.4). Diagenetic thin layers of gypsum (Fig 3.5) and anhydrite were observed interbedded with the fissile shale lithofacies in the lowermost part of vertical section-1.

The x-ray diffraction (XRD) analysis applied on samples taken from the fissile shale lithofacies shows the occurrence of quartz, kaolinite, dickite, muscovite, and halite (Fig 3.6). The scanning electron microscope (SEM) on other side were used to confirm this occurrence and to show the morphology and percentage of these minerals (Fig 3.7), (Fig 3.8), (Fig 3.9), and (Fig 3.10).

The depositional environment of the thick units of fissile shale lithofacies in the study area is probably the restricted marine offshore environment. High gamma-ray responses (Fig 3.11) may indicate high organic productivity in this environment and therefore confirms the bottom water oxygenated settings of the lower part of Qusaiba shale member in the study area. This information leads to the anoxic setting of preservation below the water column (Mahmoud et al., 1992). The siltstone layers interbedded with the fissile shale lithofacies are evidence for turbidities and storm events (Fig 3.4), that could probably indicate the transitional zone between offshore and lower shoreface environments (Mahmoud et al., 1992).

Figure 3-3 Outcrop photograph of the Fissile shale lithofacies showing that its characterized by various range of colors.

**Figure 3-4 Outcrop photograph showing the upward increase in thickness and density of the interbedded siltstone layers with the fissile shale lithofacies.**

**Figure 3-5 Outcrop photograph showing the presence of a thin diagenetic gypsum layer within a thick unit of the fissile shale.**

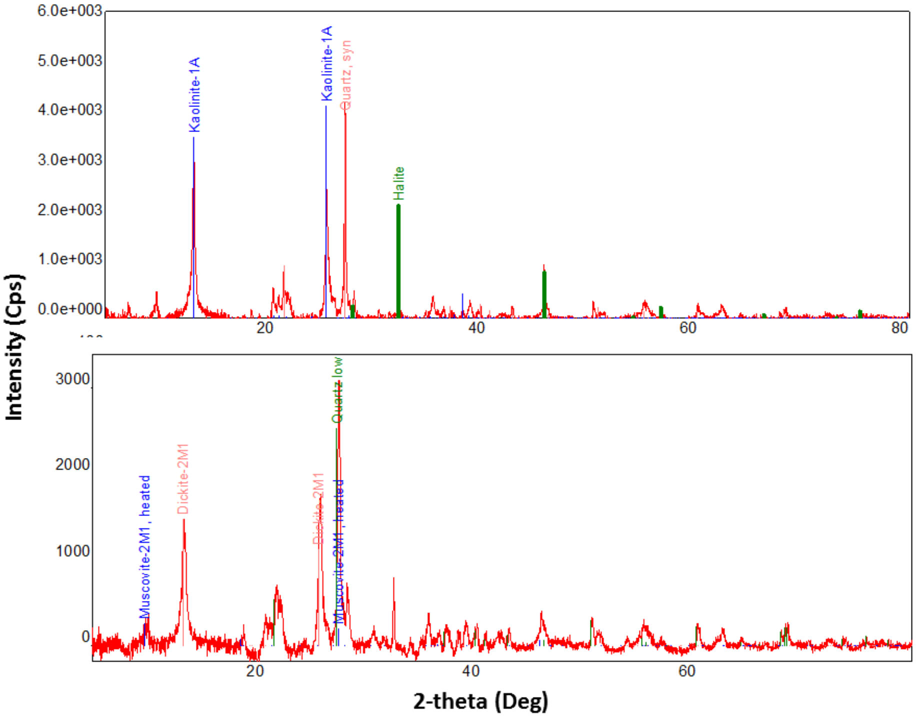

**Figure 3-6 XRD analysis of the fissile shale lithofacies showing the presence of kaolinite, quartz, muscovite, halite, and dickite that mainly form the fissile shale lithofacies.**

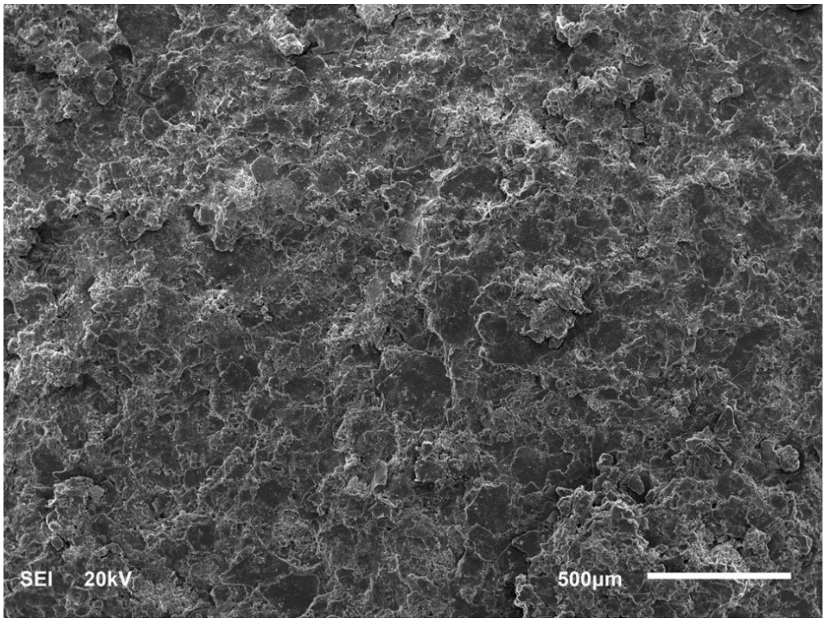

**Figure 3-7 SEM photograph of the fissile shale lithofacies showing the general morphology of the grain types.**

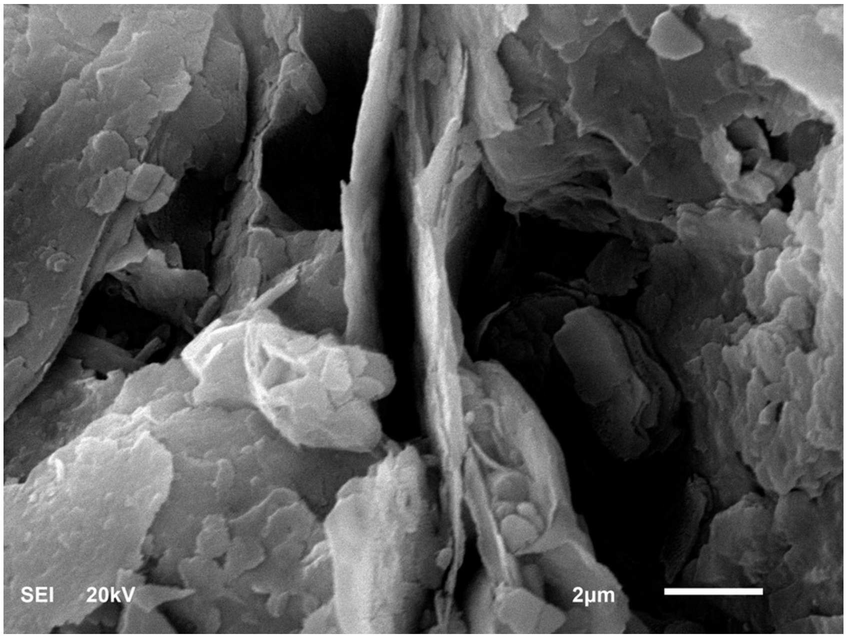

Figure 3-8 SEM photograph of the fissile shale lithofacies showing the lamination within the lithofacies.

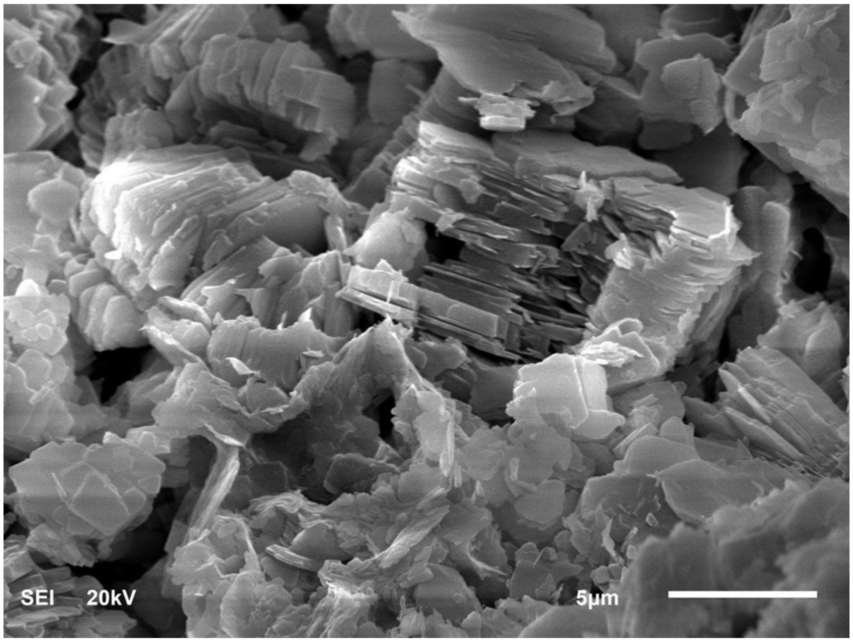

Figure 3-9 SEM photograph of the fissile shale lithofacies showing the morphology of the kaolinite as it appears within the lithofacies.

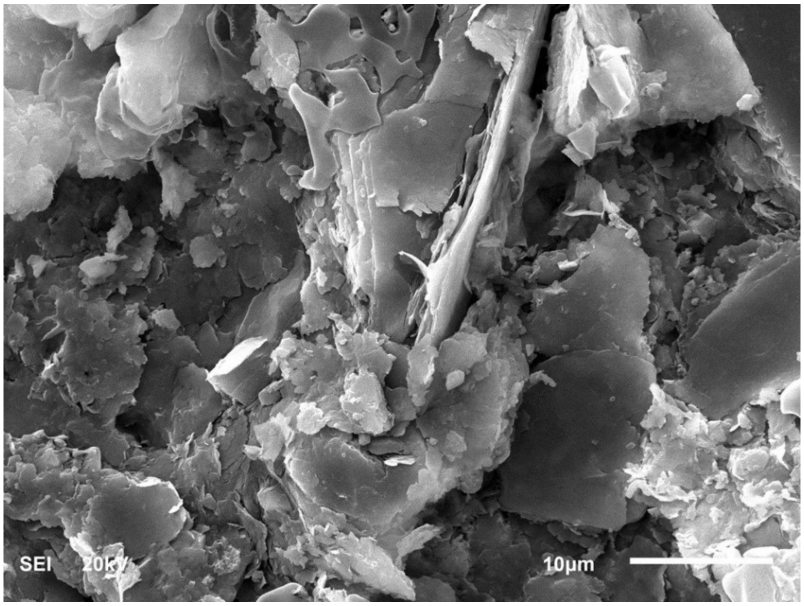

Figure 3-10 SEM photograph of the fissile shale litofacies showing the morphology of the muscovite as it appears within the lithofacies.

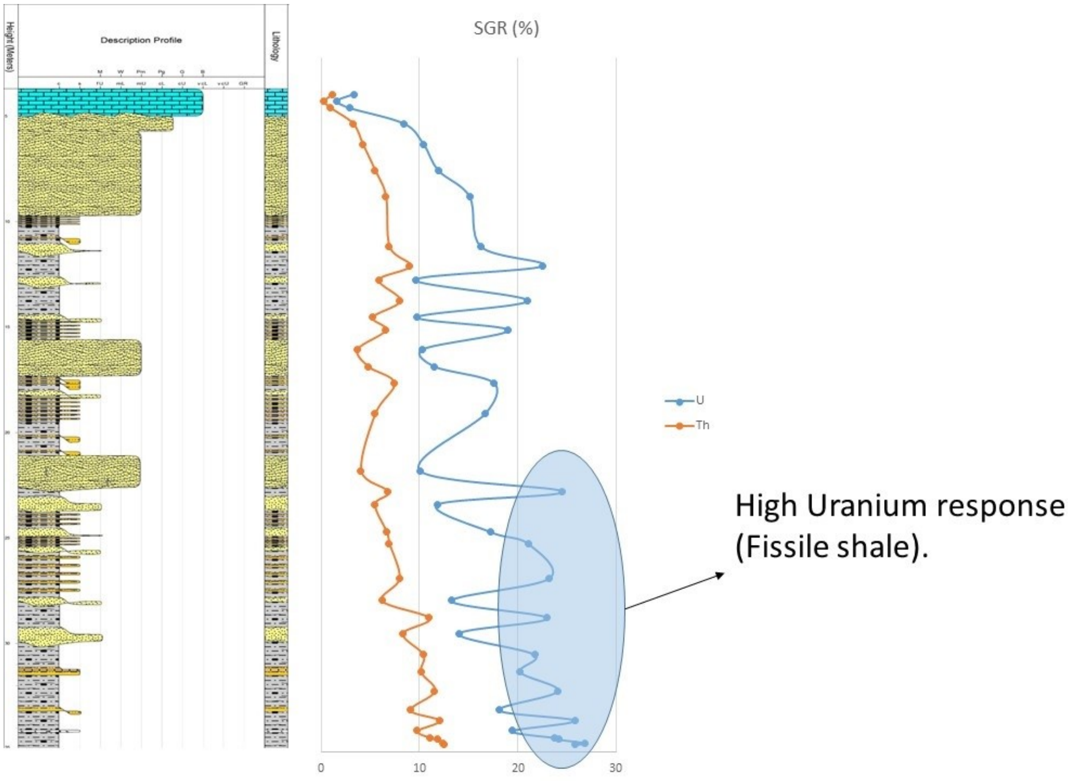

High Uranium response (Fissile shale).

Figure 3-11 Lithostratigraphic section of the first outcrop in the study area showing high readings of U* in the basal parts of the outcrop (Fissile shale lithofacies) indicating high organic matter.

### 3.2.2 Very fine grained muscovite siltstone lithofacies

The graded micaceous siltstone lithofacies thickness ranges from mm’s to cm’s per unit. The base of a siltstone unit in the outcrops is mostly graded from mudstone to laminated siltstones (Fig 3.12) with small-scale hummocky cross stratification structure. This lithofacies is located in the middle and upper parts of the vertical sections in the study area and found to be associated with the very fine to fine-grained hummocky cross-stratified sandstone lithofacies in a normal grading basis (Fig 3.13).

The very fine-grained siltstone (Fig 3.14) revealed the occurrence of Quartz, muscovite (Platy micas), and kaolinite in the x-ray diffraction (XRD) analysis (Fig 3.15) and under scanning electron microscope (SEM) (Fig 3.16) and (Fig 3.17).

The sharp bases of the hummocky cross-stratified sandstone are formed by the very fine-grained siltstone in an association thought to be deposited in marine shelf regulations in storm conditions (tempestites). This lithofacies is thought to be deposited in muddy storm conditions, due to the observation of normal grading and small-scale hummocky cross stratification structure, and the depositional environment could be interpreted as an offshore transition to distal lower shoreface (Mahmoud et al., 1992).

Figure 3-12 Outcrop photograph showing the lamination of the very fine-grained siltstone lithofacies within thick shale units.

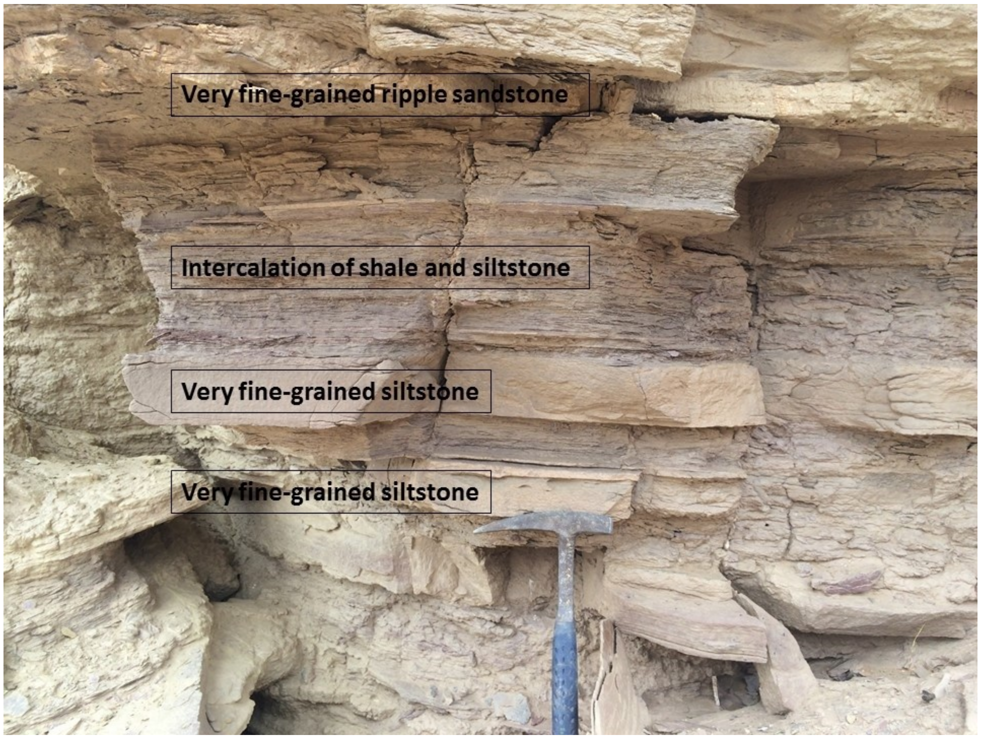

Figure 3-13 Outcrop photograph of the siltstone layers associated with the very fine to fine-grained hummocky cross-stratified sandstone lithofacies in a normal graded basis.

Figure 3-14 Thin section photograph of the very fine-grained siltstone lithofacies indicating that its mainly composed of well sorted, rounded to sub-rounded quartz grains, iron oxides, and an estimated visual porosity of about 30%.

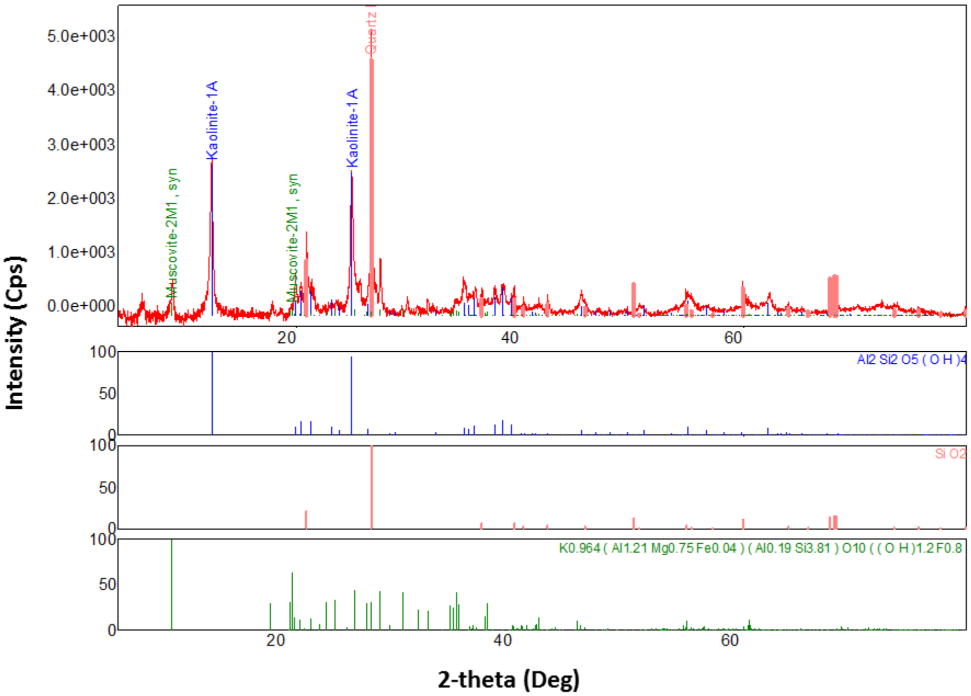

Figure 3-15 XRD analysis of the very fine-grained muscovite siltstone showing abundant quartz component, with a scattered amount of kaolinite, and muscovite.

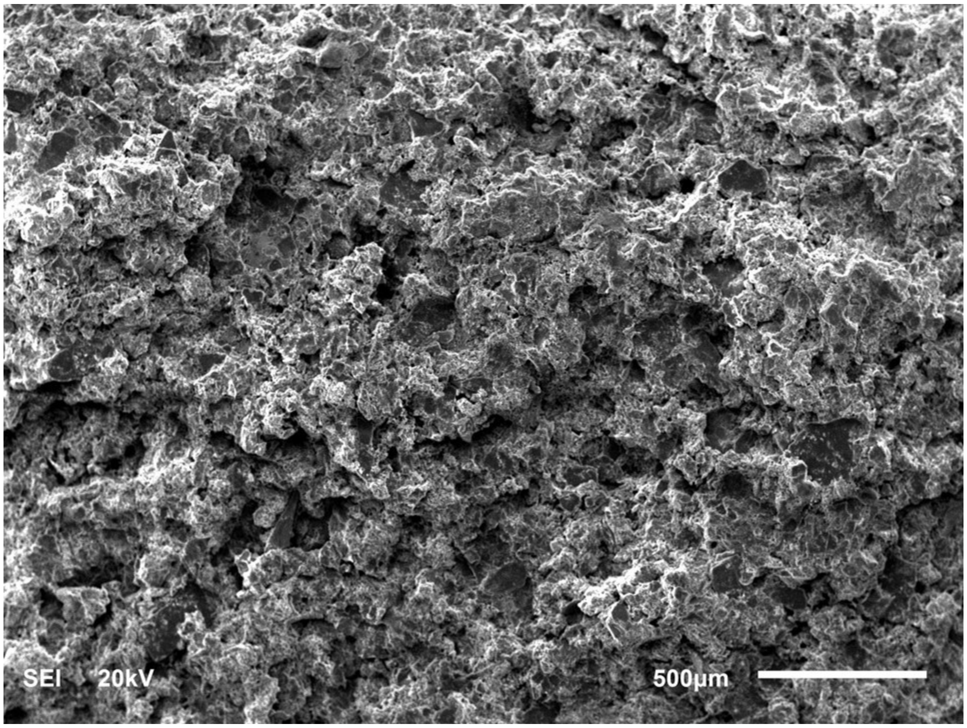

**Figure 3-16 SEM photograph of the very fine-grained muscovite siltstone showing the general morphology of the grain types.**

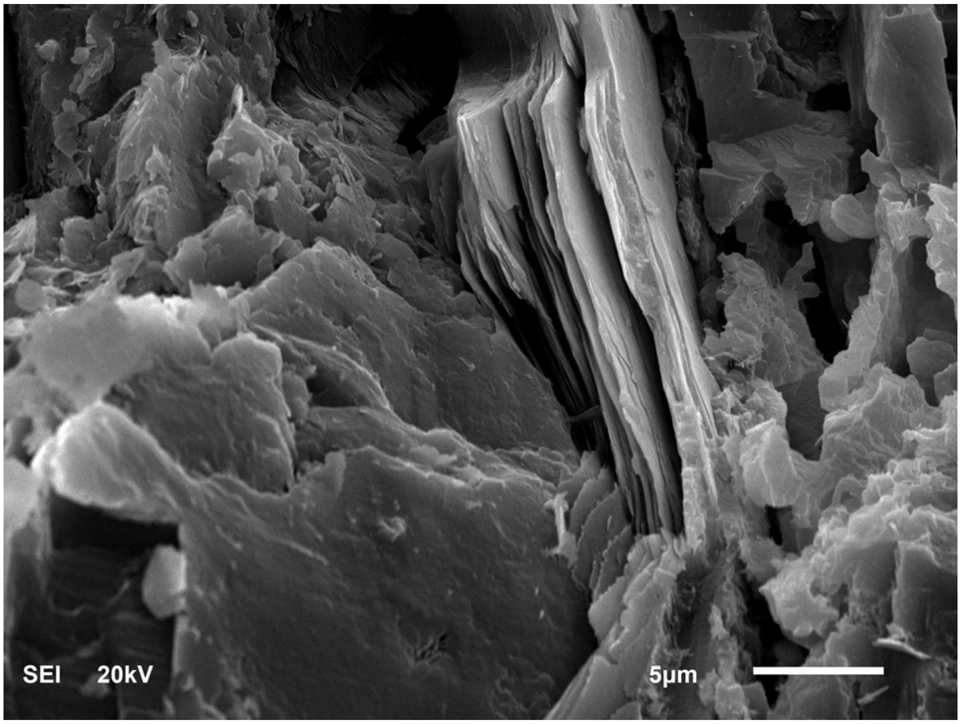

**Figure 3-17 SEM photograph of the very fine-grained muscovite siltstone showing the presence of the platy micas within the lithofacies.**

### 3.2.3 Bioturbated mudstone lithofacies

The units of mudstone lithofacies are located in the middle and upper parts of the outcrops, and they could be described as massive dark gray sub-fissile units. This lithofacies is interbedded with mm’s to cm’s thickness of laminated siltstone (Fig 3.18). Gradually on the top of mudstone units, there are very fine to fine-grained siltstone and ripple sandstone. Parallel lamination is displayed on the bioturbated mudstone lithofacies ranges in thickness from cm’s to m’s per unit, laminated with siltstones, and containing some sedimentary streaks and lenses, with moderate to high bioturbation.

X-ray diffraction (XRD) analysis showed the occurrence of low-percentage quartz, kaolinite, and dickite (Fig 3.19). Scanning electron microscope (SEM) was also used for confirmation purposes, and to show the general morphology of the lithofacies and its elements (Fig 3.20) and (Fig 3.21).

The mudstone lithofacies was probably deposited in a suspended quite water, combined with episodic storm conditions represented by the very fine-grained siltstone. The depositional environment of the mudstone facies may belong to the distal lower shoreface, and the weather of deposition is mostly normal to fair, describing the shelfal conditions of the shallow marine environment (Mahmoud et al., 1992).

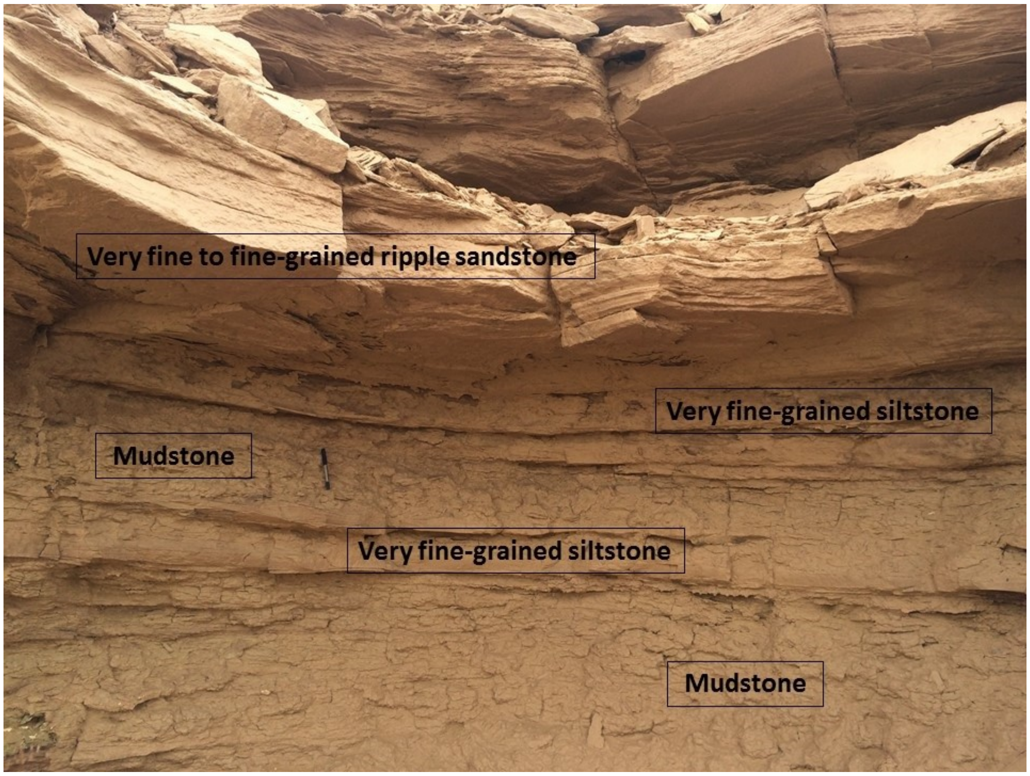

Figure 3-18 Outcrop photograph showing massive units of bioturbated mudstone lithofacies interbedded with very fine-grained siltstone as it appears in vertical section-1.

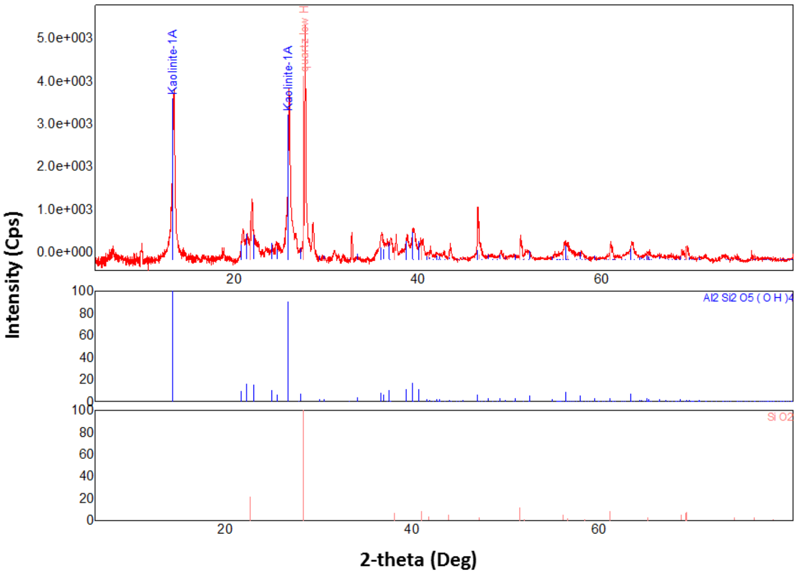

Figure 3-19 XRD analysis of the bioturbated mudstone lithofacies showing that the lithofacies is composed mainly of quartz and kaolinite.

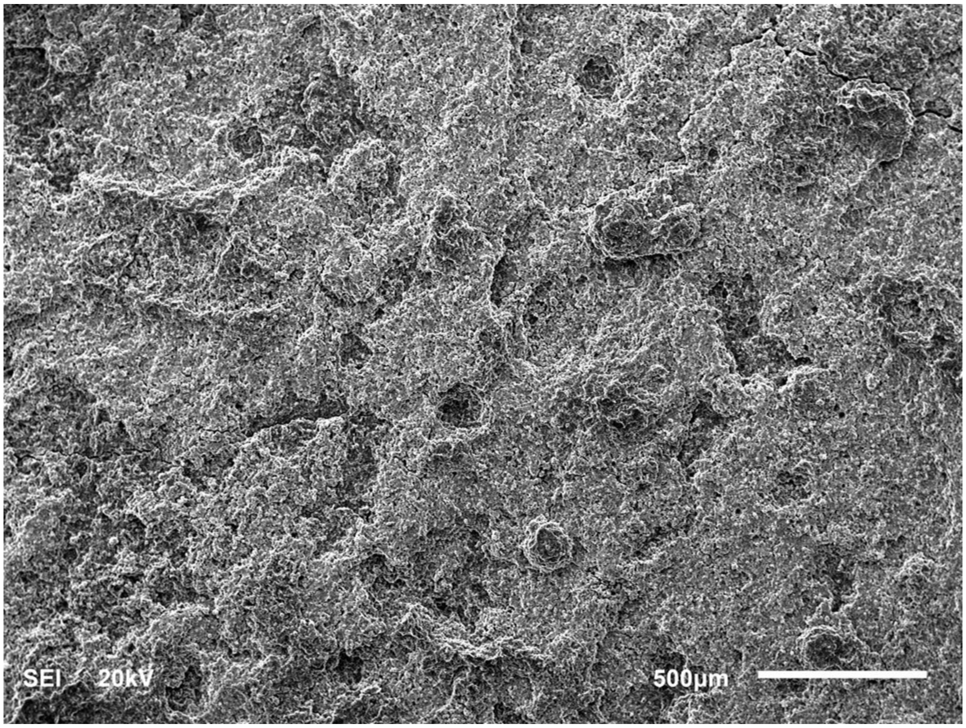

Figure 3-20 SEM photograph of the bioturbated mudstone lithofacies showing the general morphology of the grain types.

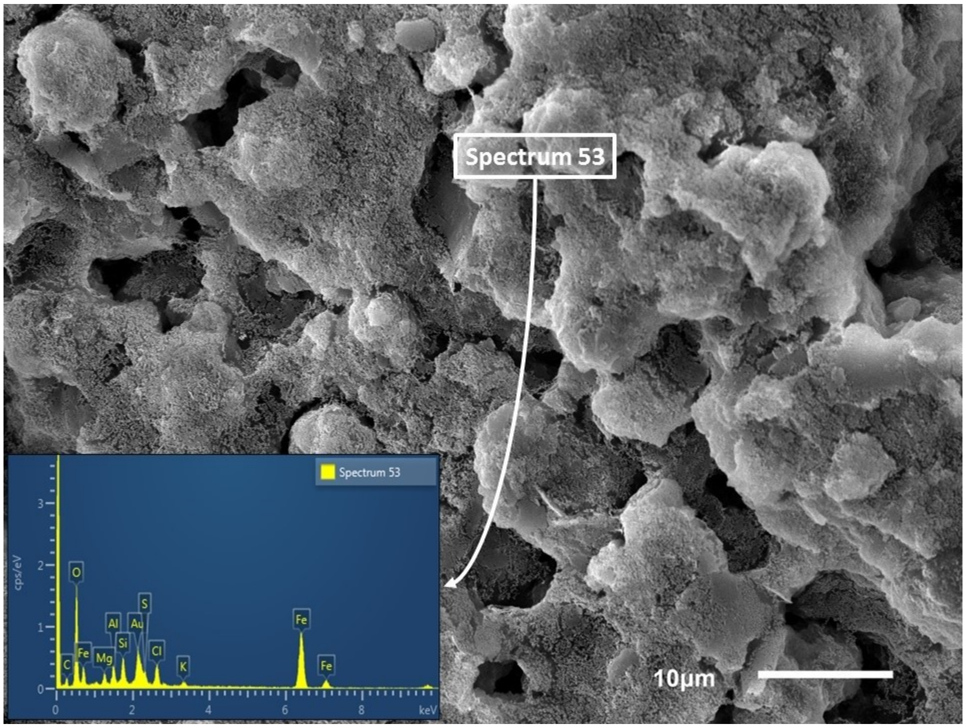

Figure 3-21 SEM photograph of bioturbated mudstone lithofacies showing the elemental composition within Spectrum 53.

### 3.2.4 Fine to very fined grained hummocky x-stratified sandstone lithofacies

Very fine to fine-grained sandstone lithofacies (Fig 3.22) is well bedded, micaceous, characterized by hummocky cross stratification (Fig 3.23) and ripple marks, and contains small pulses of mud drapes. This lithofacies occurs at the end of each depositional cycle in Qusaiba shale member, bioturbated heavily at some layers by skolithos ichnofacies (Fig 3.24). The thickness of sandstone units in this lithofacies ranges from cm's to m's.

Thin section view of the samples taken from very fine to fine-grained sandstone shows a moderate sorting for the grains (Fig 3.25). X-ray diffraction (XRD) analysis shows the occurrence of quartz, muscovite, and kaolinite (Fig 3.26). Scanning electron microscope (SEM) shows the general morphology of the minerals found in the lithofacies (Fig 3.27), (Fig 3.28), and (Fig 3.29).

Proximal lower shoreface to medium shoreface environments are usually characterized by the sedimentary structures found in this lithofacies. In proximal lower shoreface environment, the hummocky cross-stratification is mostly thinner than in other environments, it's also associated with bioturbated mudstone in many cases. The data collected from this lithofacies in the study area suggests mid to outer shelf settings of deposition (Distal) above the wave base of the storm conditions (Miller and Melvin, 2005).

The skolithos ichnofacies was thought to be an evidence for the intertidal zones only, (Benton and Harper, 1997) proposed the probability of occurrence of skolithos at the top of storm base in other sand environments. Anyhow, the skolithos represent stressful conditions for the living organisms at that time.

Figure 3-22 Outcrop photograph showing the occurrence of the Very fine to fine-grained hummocky cross-stratified sandstone lithofacies at the end of the top two depositional cycles.

Figure 3-23 Outcrop photograph of the hummocky cross-stratification sedimentary structure as it appears within the very fine to fine-grained hummocky cross-stratified sandstone lithofacies.

Figure 3-24 Outcrop photograph of the Symmetrical ripple marks within the hummocky cross-stratified sandstone lithofacies.

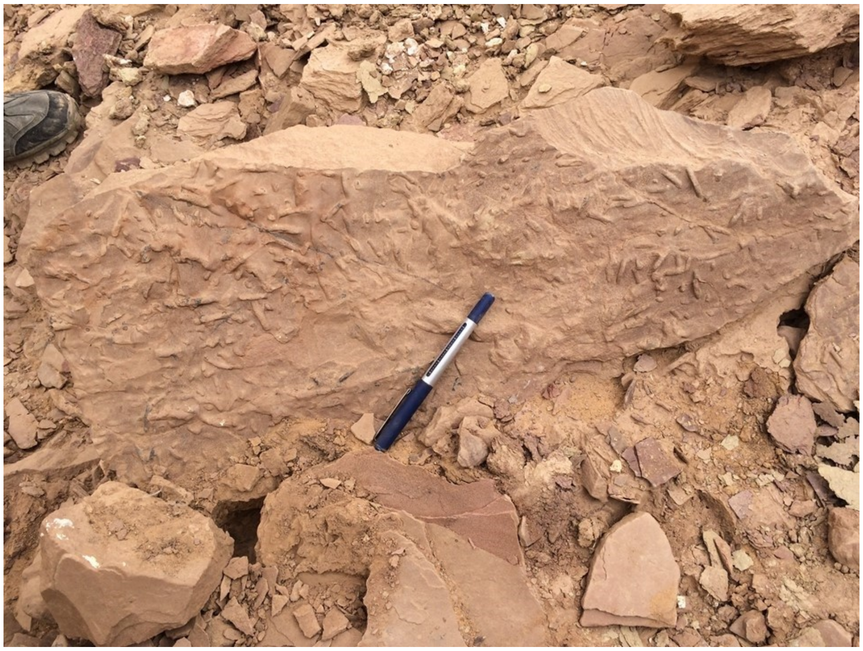

Figure 3-25 Outcrop photograph of the Skolithos ichnofacies as it appears within the hummocky cross-stratified sandstone lithofacies.

Figure 3-26 Thin section photograph of the very fine to fine-grained hummocky cross-stratified sandstone showing the presence of the well sorted quartz grains, iron oxides, and visual pores.

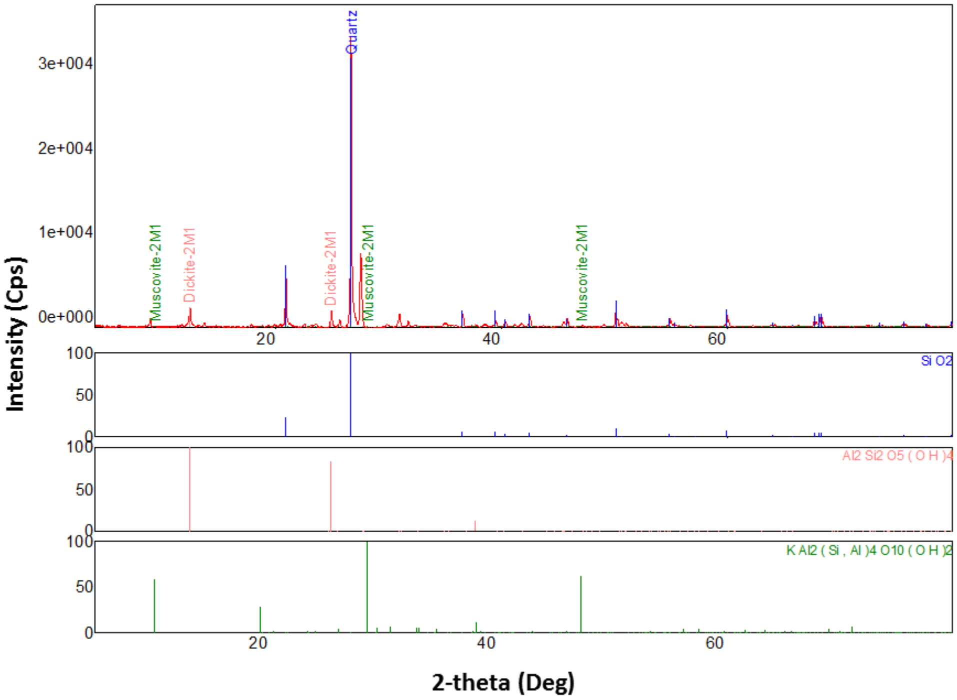

Figure 3-27 XRD analysis of the hummocky cross-stratified sandstone lithofacies showing the presence of quartz, dickite, and muscovite.

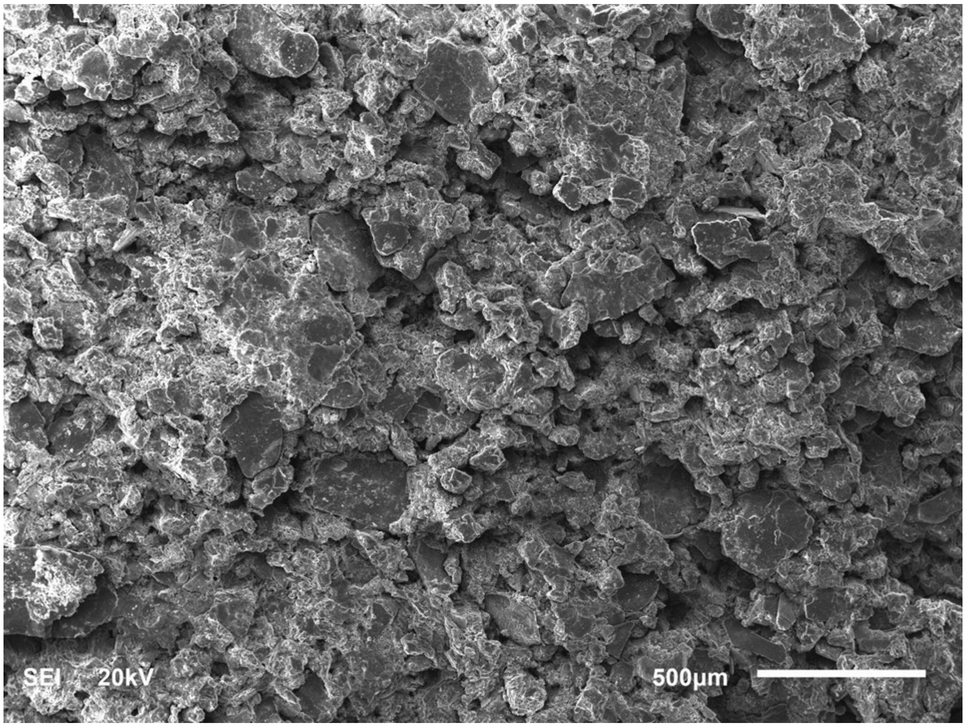

Figure 3-28 SEM photograph of the very fine to fine-grained hummocky sandstone lithofacies showing the general morphology of the different grain types.

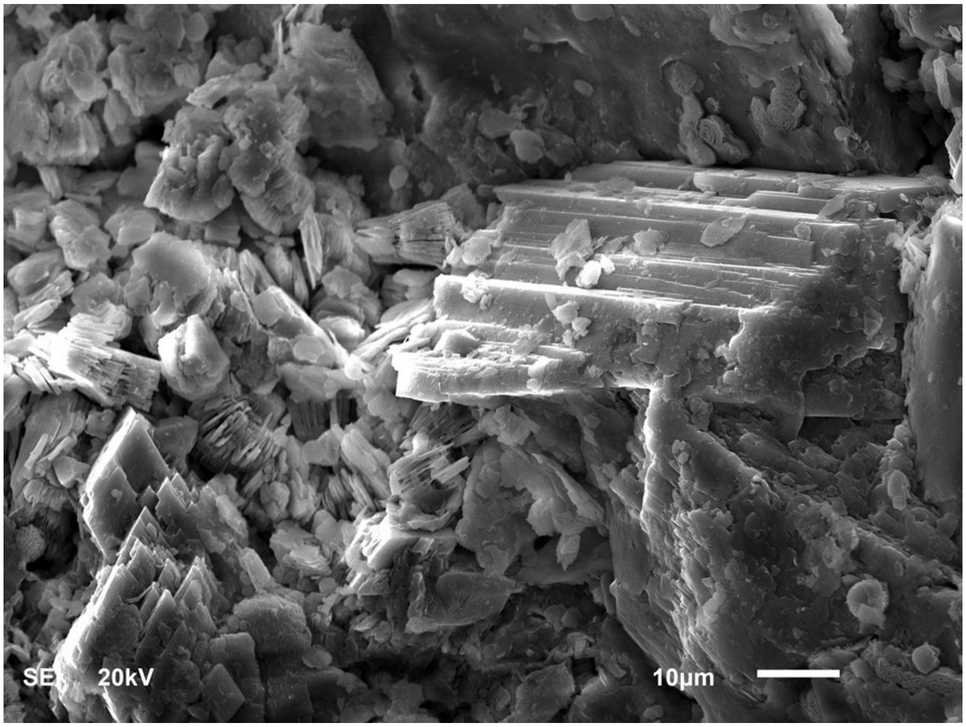

Figure 3-29 SEM photograph of the hummocky sandstone lithofacies showing the presence of Quartz and dickite within the matrix of the lithofacies.

### 3.2.5 Fined to medium grained low/high angle x-stratified sandstone lithofacies

The grain sizes of this lithofacies range from fine to medium, and the grains sorting is poor to moderate. Low angle cross-stratified sandstone lithofacies rocks are light-brown colored turning gradually into darker colors. Located in the uppermost parts of the outcrops in a gradual base with the hummocky cross-stratified sandstone lithofacies in the study area with cm’s to m’s thickness per unit, and characterized by low angle cross-bedding (Fig 3.30), high angle cross-bedding (Fig 3.31), small-scale trough cross-bedding (Fig 3.32), and wave ripples (Fig 3.33) sedimentary structures.

Thin sections of this lithofacies show the poor sorting of the grains (Fig 3.34), X-ray diffraction (XRD) analysis pronounces clearly the dominance of Quartz (Fig 3.35), and Scanning electron microscope (SEM) shows the morphology of the Quartz and clayey cementing materials (Fig 3.36) and (Fig 3.37).

The low/high angle cross-stratified sandstone lithofacies was probably deposited in middle shoreface to distal upper shoreface environments, due to the presence of low and high angle cross bedding in storm wave settings, indicating current deposition of a higher energy (Miller and Melvin, 2005).

Figure 3-30 Outcrop photograph showing the low angle cross-stratification within the fine to medium low/high angle cross-stratified sandstone lithofacies.

Figure 3-31 Outcrop photograph showing the high angle cross-stratification within the low/high angle cross-stratified fine to medium sandstone lithofacies.

**Figure 3-32 Outcrop photograph showing the thin lamination and trough cross stratification within the low/high angle cross-stratification fine to medium sandstone lithofacies.**

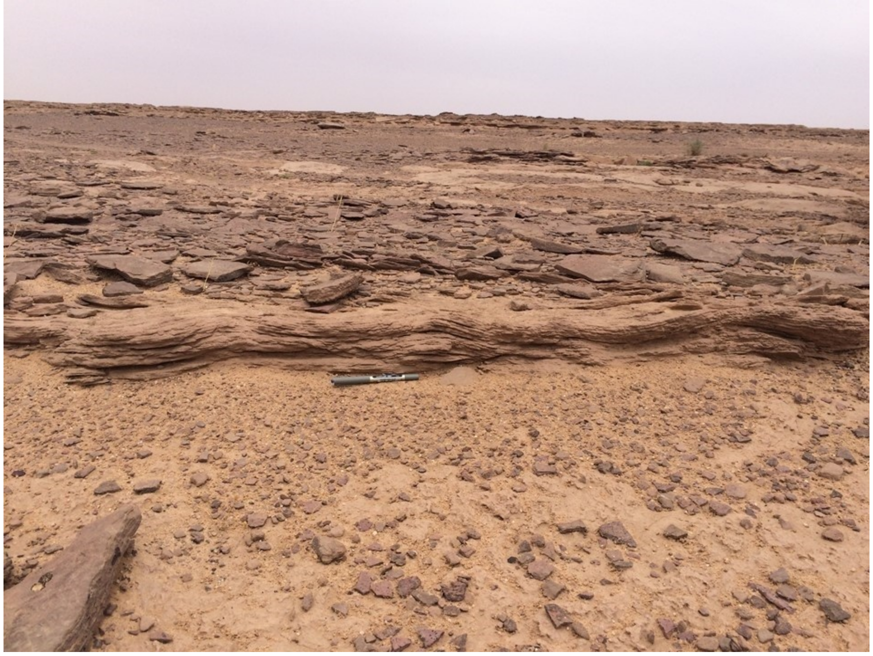

**Figure 3-33 outcrop photograph showing the symmetrical wavy ripples within the low/high angle cross-stratification fine to medium sandstone lithofacies.**

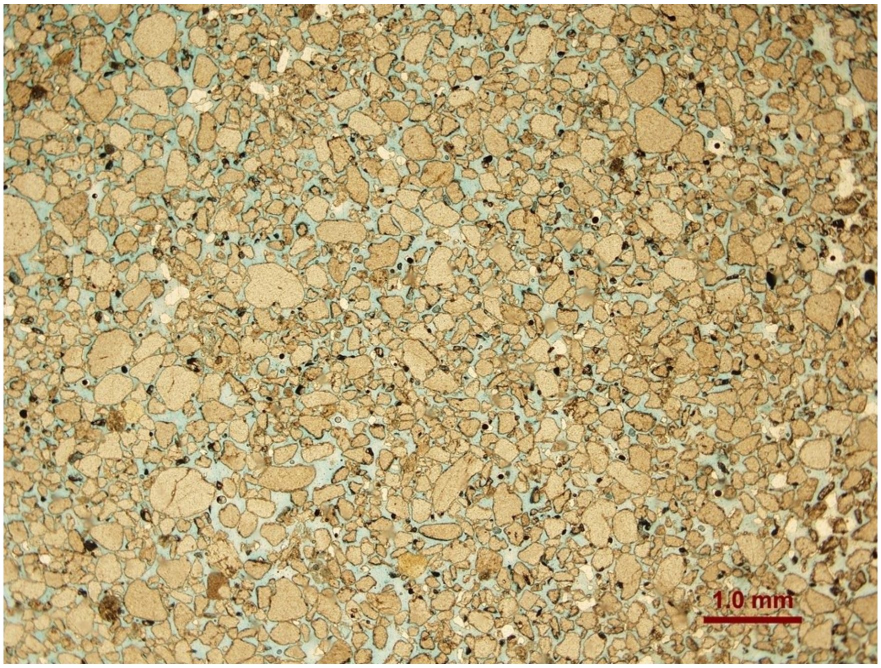

Figure 3-34 Thin section photograph image of the fine to medium Low/high angle cross-stratified sandstone shows the presence of poorly sorted, sub-angular to sub-rounded quartz grains, with high visual porosity.

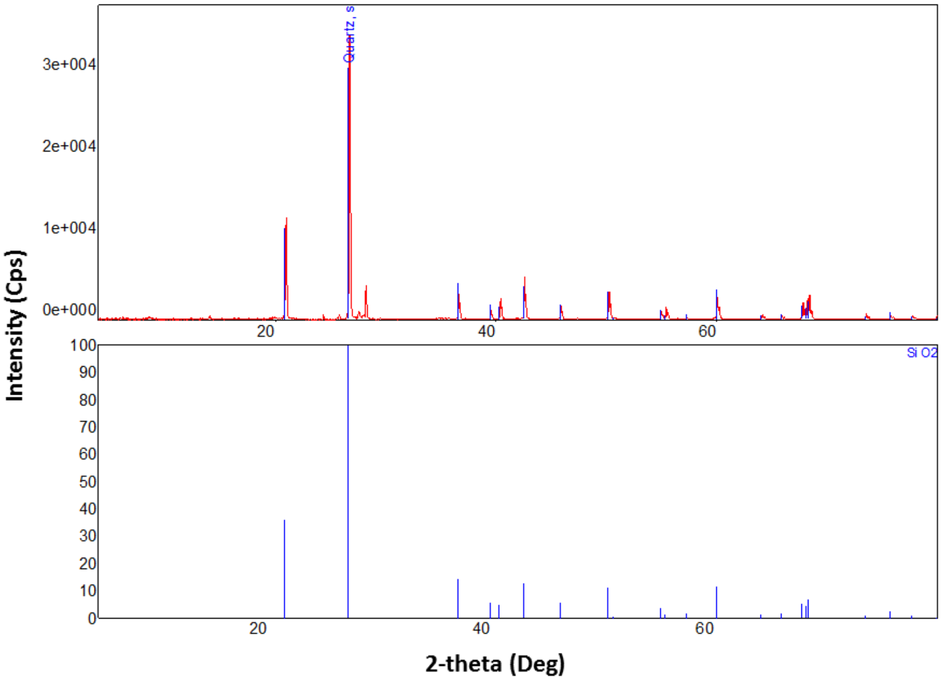

Figure 3-35 XRD analysis of low/high angle cross-stratified lithofacies showing the existence of quartz as the main component of the lithofacies.

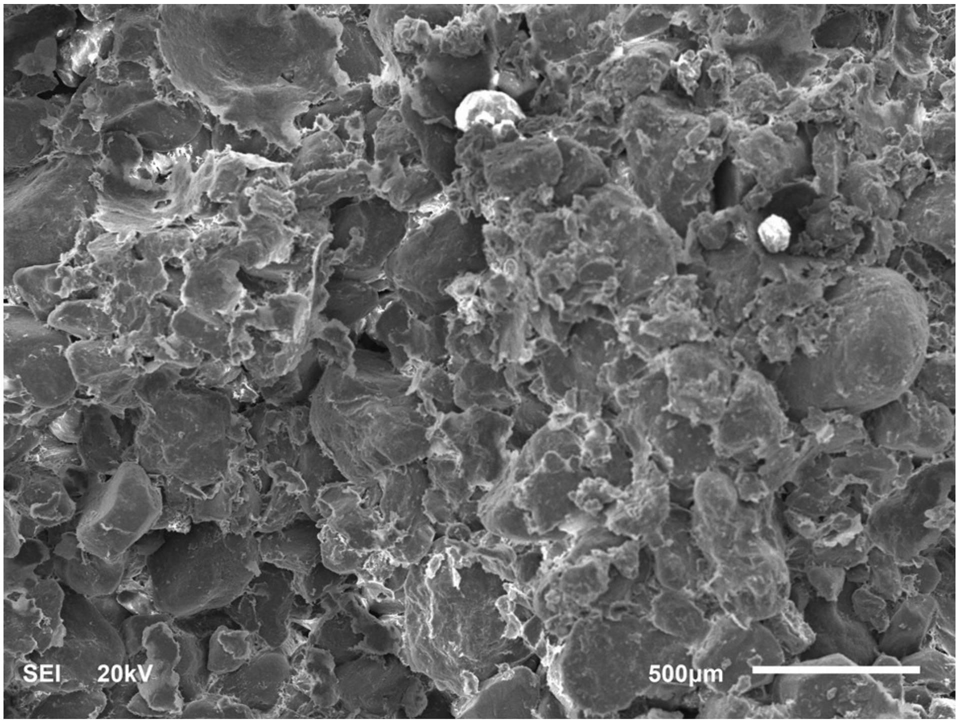

**Figure 3-36 SEM image of a sample showing the general morphology of the low/high cross-stratified sandstone lithofacies minerals.**

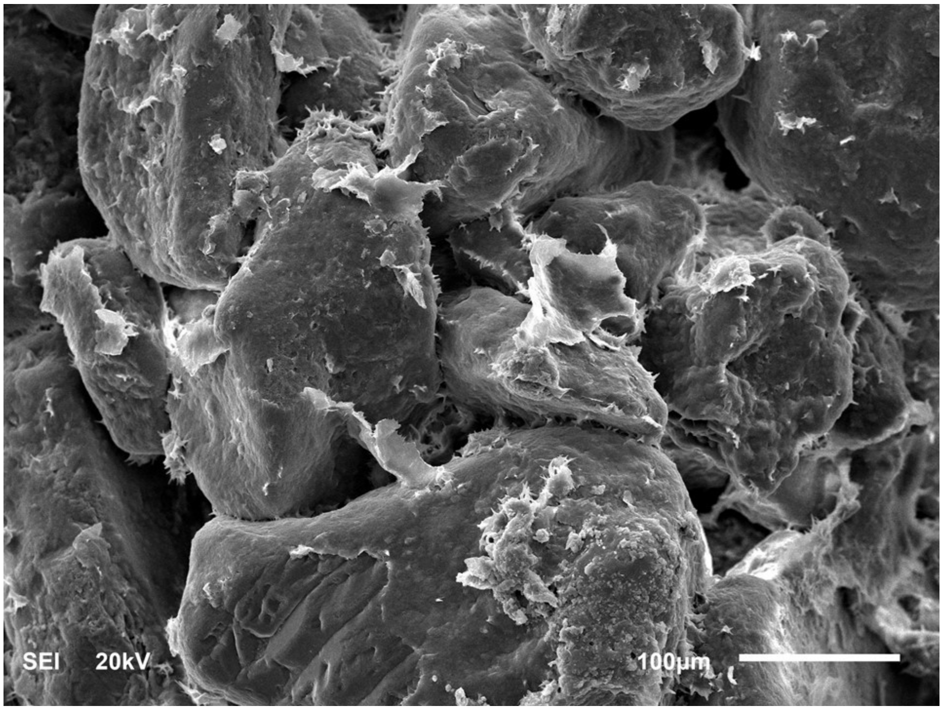

**Figure 3-37 SEM image of the low/high angle cross-stratified sandstone lithofacies showing the general morphology of Quartz.**

## 3.3 Depositional model

Fissile shale lithofacies was deposited in an offshore depositional environment controlled by quite anoxic conditions. In this study the early Silurian period, when the fissile shale of Qusaiba hot shale member deposited in Saudi Arabia, was following the major glaciation period of late Ordovician (McClure, 1988). The high sea level and climatic conditions at the Silurian period were a result of the deglaciation process of the late Ordovician glaciers. The deglaciation made it possible for a huge number of faunal groups to retrieve and resist extinction. Therefore, the shale of Qusaiba is very rich with organic matter that deposited with the shale in a deep water conditions, and the reason why it's called Qusaiba hot shale member is the fact that Qusaiba shale represents an important source rock of hydrocarbons for most of the reservoirs in the Arabian region (Mahmoud et al., 1992). Offshore to lower shoreface transitional environment is characterized in the study area by the deposition of shale and very fine-grained siltstone, where the shale represents normal to fair conditions of weather, and the siltstone represents the storm events during deposition (Dott and Bourgeois, 1982). Lower shoreface environment is characterized in this study by the deposition of the very fine to fine-grained hummocky cross-stratified sandstone, that is usually thought to be deposited in an open marine environment between the normal to fair weather and the storm bases (Dott and Bourgeois, 1982). Hummocky cross-stratified sandstone, when found accumulated, indicates coastal zones, nearshore to shoreface depositional environments. Low angle cross-stratification and wave ripples sedimentary structures can also be found in these conditions as the deposition process moves toward the continental shelf (Mahmoud et al., 1992). Middle shoreface to upper shoreface depositional environments are characterized in this study by the occurrence of fine to medium low/high angle cross-stratified sandstone and trough cross-stratified sandstone, which is believed to be deposited above the storm base (Mahmoud et al., 1992)

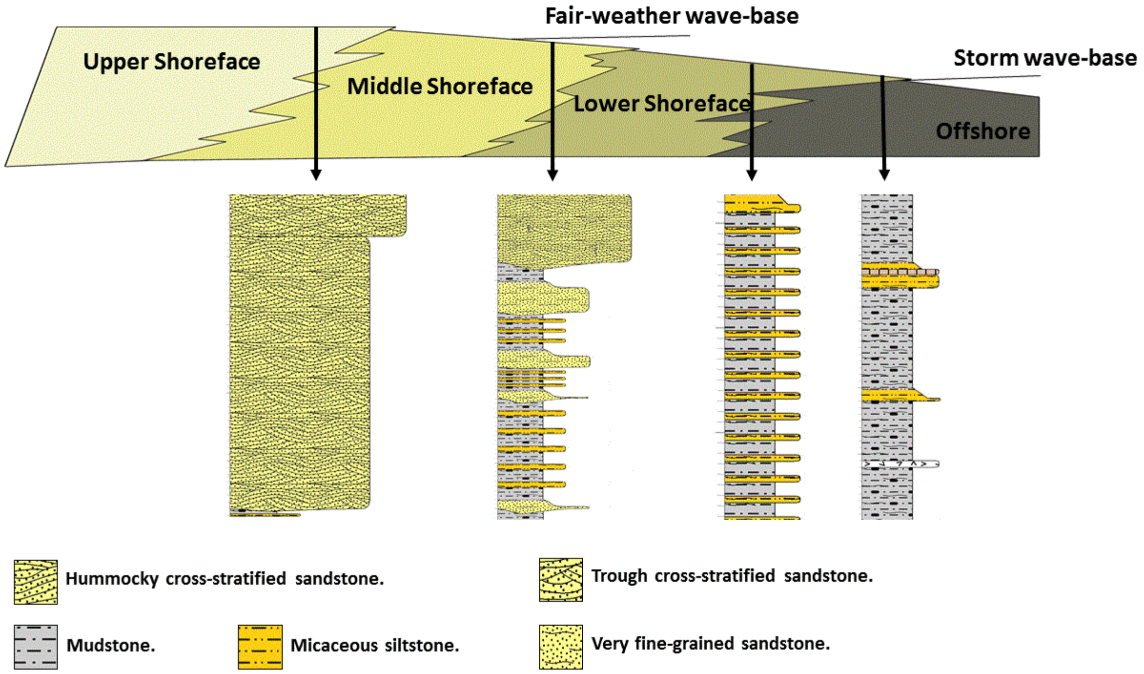

Figure 3-38 Qusaiba Silurian shale member was deposited in an offshore, lower shoreface, middle shoreface, and upper shoreface lithofacies.

## 3.4 3D lithofacies modeling

(1km ×2km) area 3D geostatistical model has been generated in order to show the distribution of the lithofacies and their average porosity values as calculated from the samples of Qusaiba shale member of Qalibah formation in the study area. The 3D model (Fig 3.39), (Fig 3.40), (Fig 3.41), and (Fig 3.42) shows the decrease of the depositional cycles thickness away from the deeper part of the basin.

Zone-1 was modeled using sequential indicator simulation, and it represents the first depositional cycle of Qusaiba shale member in the study area, which consists of 52% of fissile shale, 17% of micaceous siltstone intercalated with the fissile shale, 3.5% of Mudstone, 18.5% of laminated siltstone to very fine-grained sandstone, and 9% of very fine to fine-grained hummocky cross-stratified sandstone at the top of the zone. Zone-1 reflects high percentage values of porosity due to the high percentage of high porosity fissile shale.

Zone-2 was modeled using sequential indicator simulation, and it represents the second depositional cycle of Qusaiba shale member in the study area, which consists of 26% of bioturbated mudstone, 30% of micaceous siltstone, 4% of laminated siltstone to very fine-grained sandstone, and 40% of very fine to fine-grained hummocky cross-stratified sandstone at the top of the zone. Laminated siltstone to very fine-grained sandstone lithofacies is pinched out in the middle of the zone and ended in the hummocky cross-stratified sandstone. Zone-2 reflects high porosity percentage values in the hummocky cross-stratified sandstone, and that could be an effective element for reservoir quality assessments.

Zone-3 was modeled using truncated Gaussian simulation, and it represents the third depositional cycle of Qusaiba shale member in the study area, which consists of 26% of bioturbated mudstone,

22% of siltstone-mudstone intercalation, 7% of siltstone to very fine-grained sandstone, 15% of very fine to fine-grained hummocky cross-stratified sandstone, 15% of fine to medium-grained low/high angle cross-stratified sandstone, and 15% of medium to coarse-grained pebbly sandstone. As we move toward the shallower part of the basin, it's recognized that the sandstone in zone-3 gets coarser when it turns from fine to very fine-grained hummocky cross-stratified sandstone in the deeper part of the basin into fine to medium-grained low/high angle cross-stratified sandstone into medium to coarse pebbly sandstone in the shallower part of the basin. The 3 types pf sandstone show clear horizontal interfingering between them. Regarding reservoir quality assessments, the 3 types of sandstone could be potential spots for hydrocarbon assemblages if other petroleum elements are found

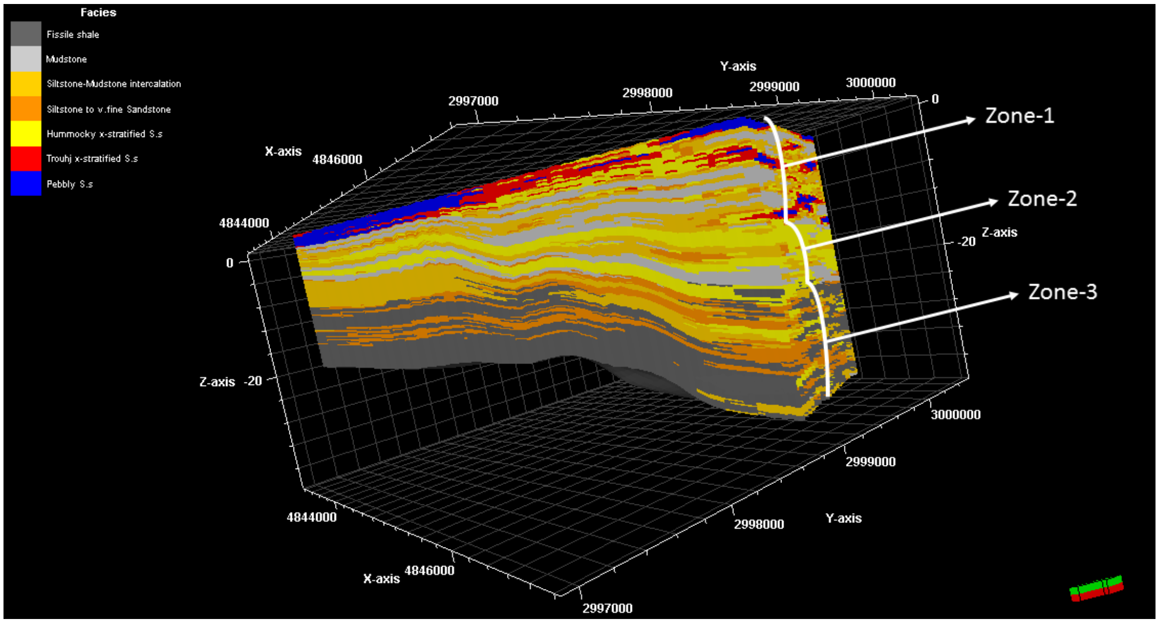

**Figure 3-39 The 3D geostatistical model viewed from the South-East shows the lithofacies distribution of Qusaiba shale member in the study area.**

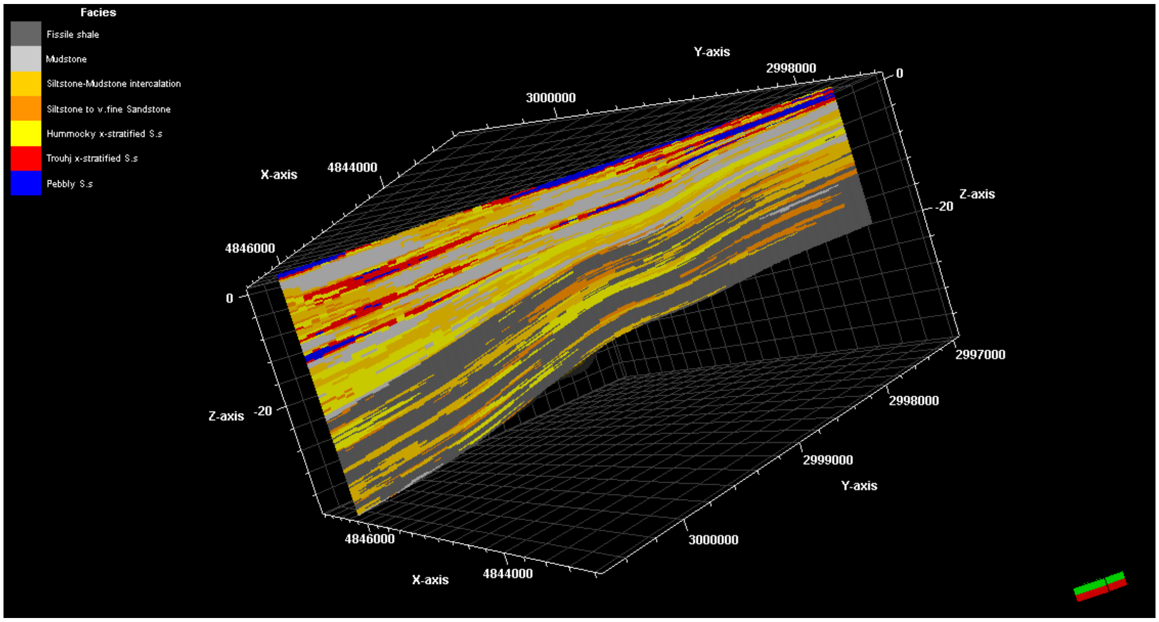

**Figure 3-40 The 3D geostatistical model viewed from the North-West shows the lithofacies distribution of Qusaiba shale member in the study area.**

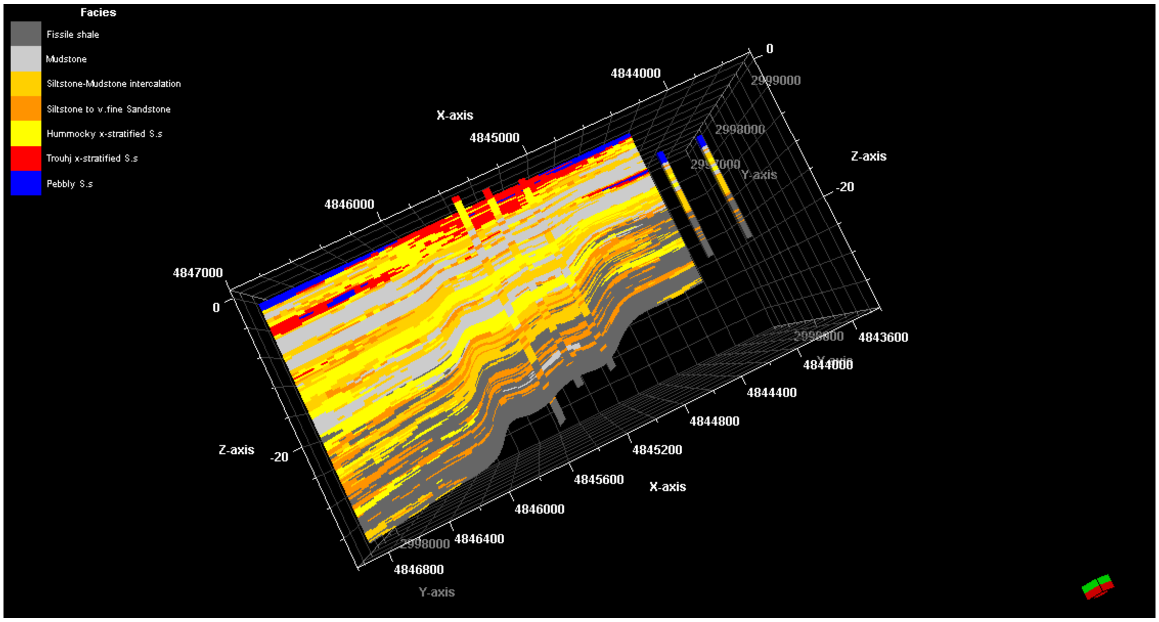

Figure 3-41 North slice view of the 3D geostatistical model shows the lithofacies distribution of Qusaiba shale member in the study area.

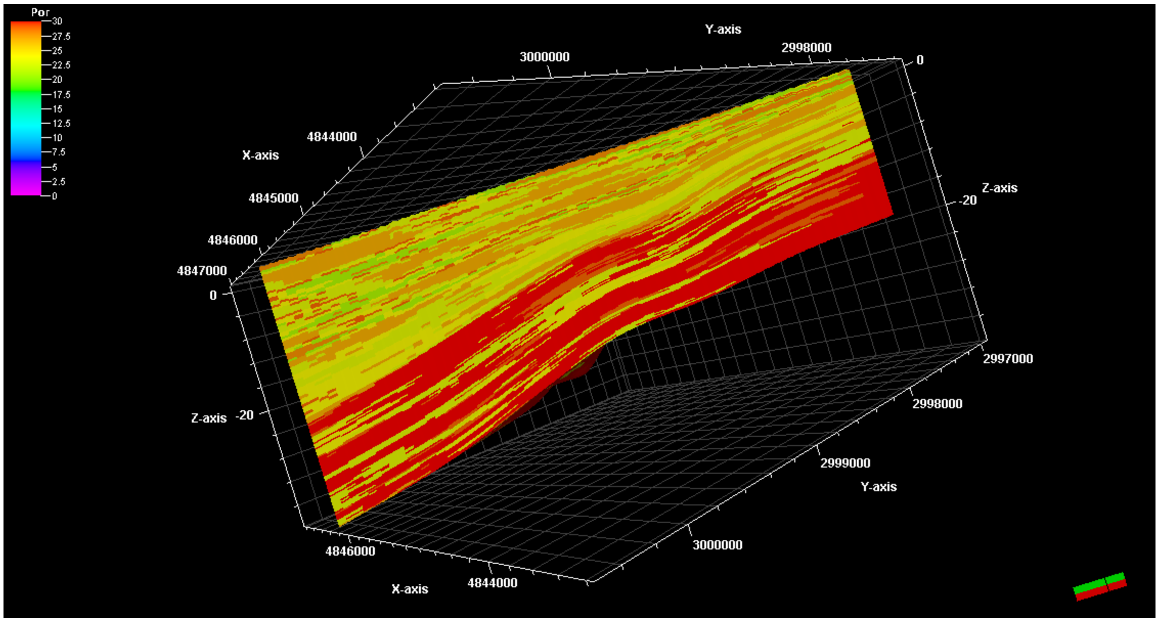

Figure 3-42 3D geostatistical model viewed from the North-West shows the distribution of porosity percentage values in the study area. (porosity were assigned as numeric values into the lithofacies model).

# CHAPTER 4

# Fractures system within Qusaiba shale member

## 4.1 Lineaments interpretation and analysis

Interpreted Landsat-ETM+ map (42km × 42km) of the study area (Fig 4.1) showed that the mean length of the lineaments is 3km (Fig 4.5), and interpreted Spot-7 map (5.4km × 8.1km) (Fig 4.2) showed that the mean length of the lineaments is 400m (Fig 4.6). Descriptive statistics tables were generated for lineaments lengths in the study area to summarize the observations of the interpreted satellite images (Table 4.1) and (Table 4.2). Spot-7 and Landsat-ETM+ satellite images revealed two major trends of lineaments; 300°-330° and 15°-40°, and two minor direction sets of lineaments with a smaller length; 270°-285° and 60°. Different orientations of lineaments from the interpreted satellite images in the study area were represented in rose diagrams (Fig 4.3) and (Fig 4.4). The two satellite images used in this study were interpreted in two different scales. Landsat-ETM+ satellite image is of a larger scale than Spot-7 satellite image. Amar collision has generated fracture patterns trending NE and NW, which can be identified along the Arabian plate basement. Najd fault system trending NW is thought to be formed as a younger feature after the collision (Al-Husseini, 2000). The main fracture patterns in the study area; NW and NE directions might be linked to the post-Amar collision fractures (NE trend) and Najd fault system (NW trend).

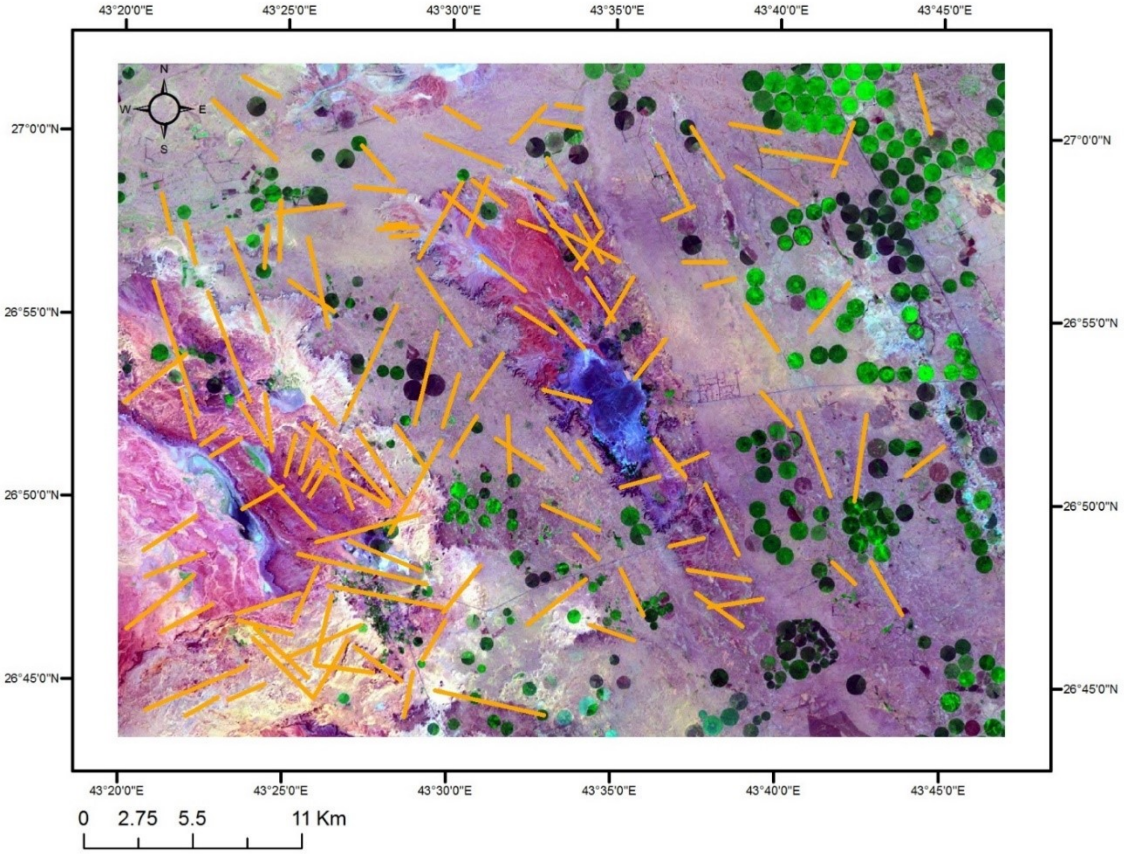

Figure 4-1 Lineaments interpretation of the Landsat-ETM+ satellite image.

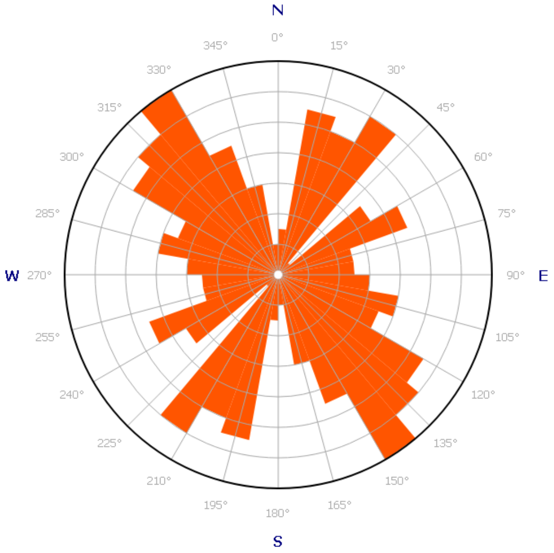

Figure 4-2 Rose diagram of the lineaments from Landsat-ETM+ satellite image showing the two major directions in the study area; NE-SW and NW-SE.

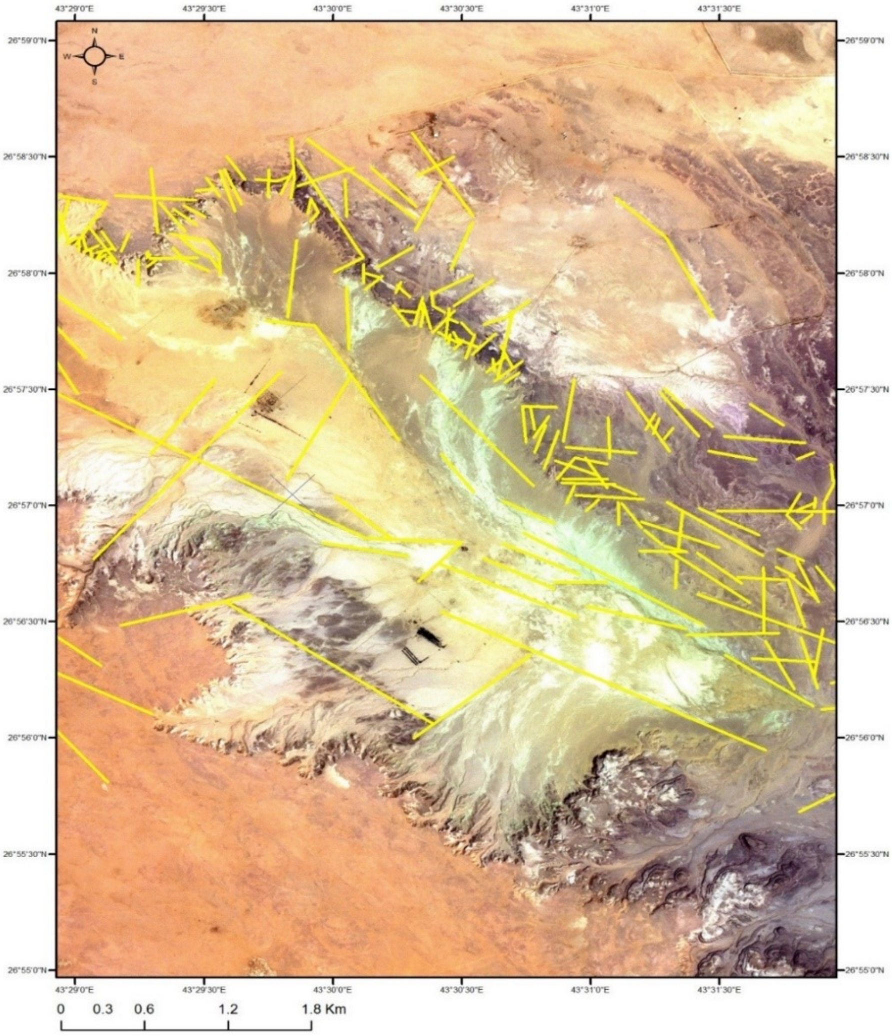

Figure 4-3 Lineaments interpretation of Spot-7 satellite image.

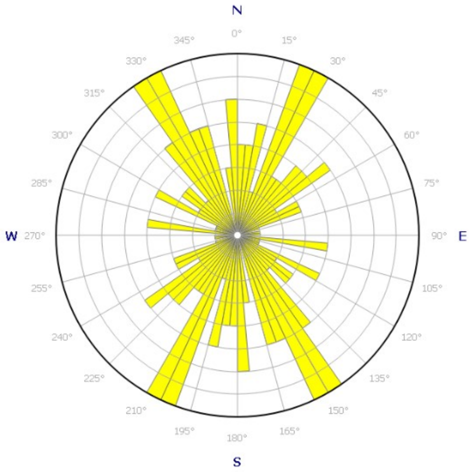

Figure 4-4 Figure 4 6 Rose diagram of lineaments from Spot-7 satellite image showing the two major directions in the study area; NE-SW and NW-SE.

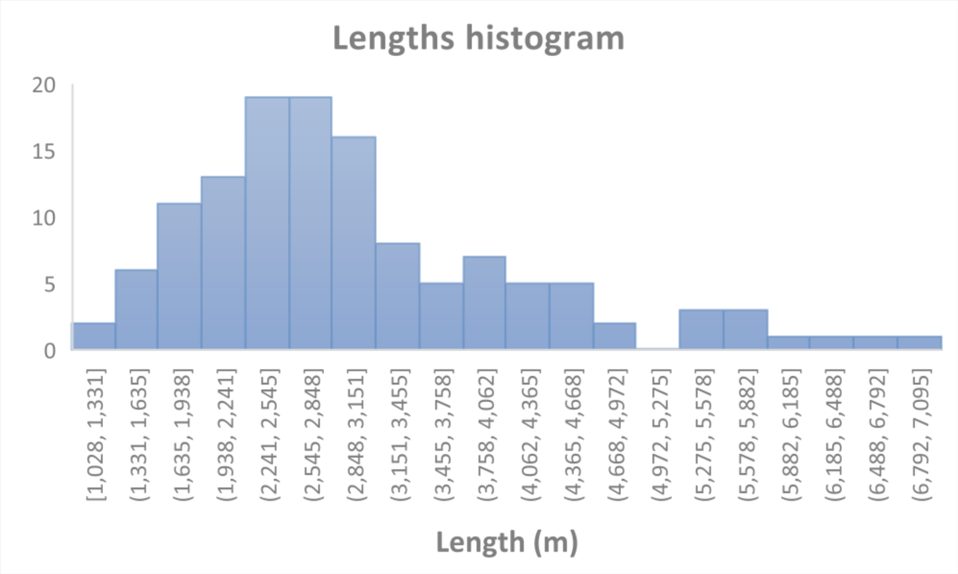

Figure 4-5 Histogram of lineaments lengths from Spot-7 satellite image.

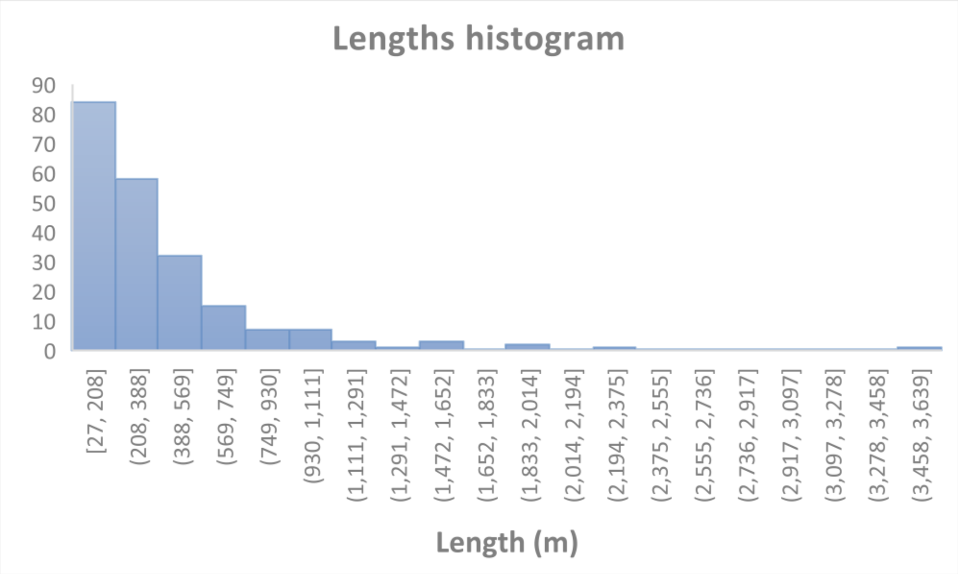

Figure 4-6 Histogram of lineaments lengths from Landsat-ETM+ satellite image.

Table 4-1 Descriptive statistics summary of lineaments lengths from Spot-7 satellite image.

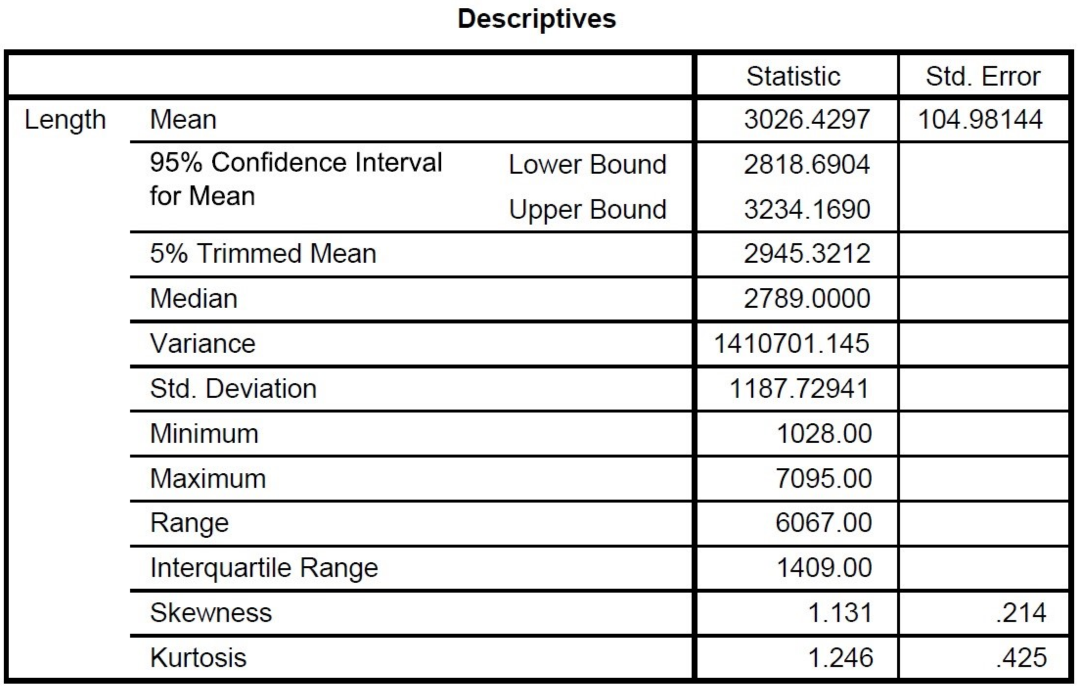

**Descriptives**

| | | | Statistic | Std. Error |
|---|---|---|---|---|
| Length | Mean | | 3026.4297 | 104.98144 |
| | 95% Confidence Interval for Mean | Lower Bound | 2818.6904 | |
| | | Upper Bound | 3234.1690 | |
| | 5% Trimmed Mean | | 2945.3212 | |
| | Median | | 2789.0000 | |
| | Variance | | 1410701.145 | |
| | Std. Deviation | | 1187.72941 | |
| | Minimum | | 1028.00 | |
| | Maximum | | 7095.00 | |
| | Range | | 6067.00 | |
| | Interquartile Range | | 1409.00 | |
| | Skewness | | 1.131 | .214 |
| | Kurtosis | | 1.246 | .425 |

Table 4-2 Descriptive statistics summary of lineaments lengths from Landsat-ETM+ satellite image.

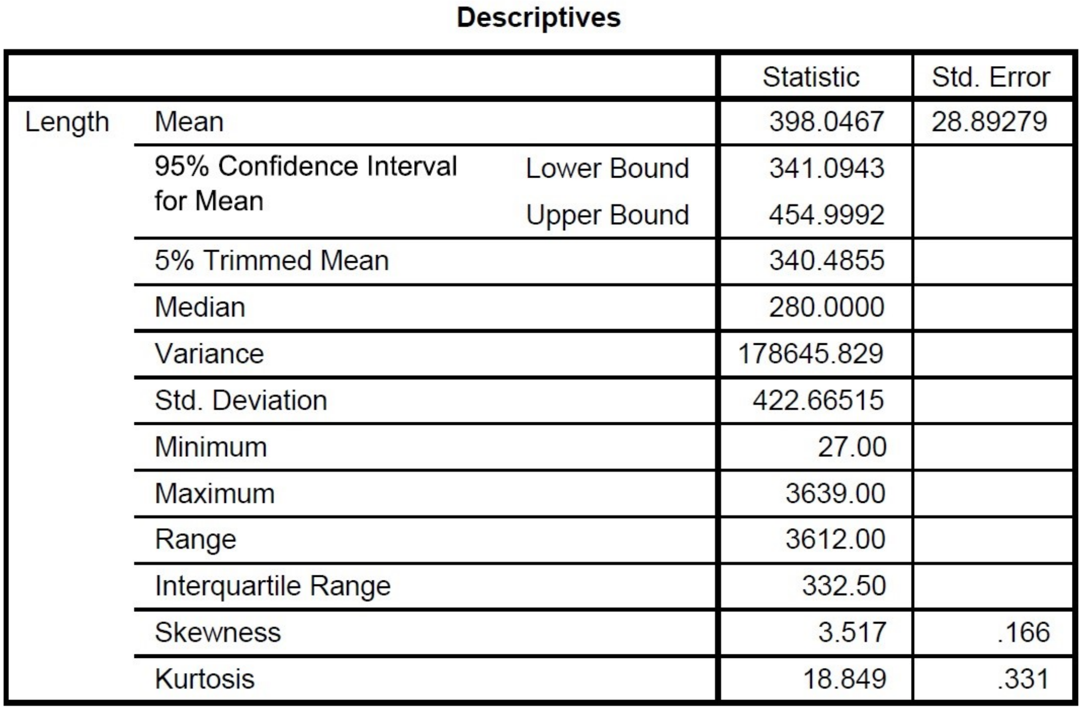

**Descriptives**

| | | | Statistic | Std. Error |
|---|---|---|---|---|
| Length | Mean | | 398.0467 | 28.89279 |
| | 95% Confidence Interval for Mean | Lower Bound | 341.0943 | |
| | | Upper Bound | 454.9992 | |
| | 5% Trimmed Mean | | 340.4855 | |
| | Median | | 280.0000 | |
| | Variance | | 178645.829 | |
| | Std. Deviation | | 422.66515 | |
| | Minimum | | 27.00 | |
| | Maximum | | 3639.00 | |
| | Range | | 3612.00 | |
| | Interquartile Range | | 332.50 | |
| | Skewness | | 3.517 | .166 |
| | Kurtosis | | 18.849 | .331 |

## 4.2 Field data characteristics

Fractures have been studied in 4 different locations in the area, The first two locations represents the siltstone and shale of Qusaiba shale member from top view, these locations - 26°56’18” N 43°32’08” E (Location-1) and 26°56’23.1” N 43°31’55.6” E (Location-2) – are almost having the same main direction sets of the Satellite view; 20° and 320°, and the spacing pattern is almost the same in the two locations; 2.5m space between the 20°NE fractures, and 1.5m space between the 320° fractures (Fig 4.7), (Fig 4.8), and (Fig 4.9).

### 4.2.1 Location 3

Location-3 represents the location of the first vertical section (26°56’23.1” N 43°31’55.6” E). The results show that the density of fractures depends on the lithological and geomechanical properties of each bed. Fissile shale and mudstone have the maximum number of fractures per meter, Siltstone units have a moderate number, and Sandstone units have the least number of fractures per meter. Only one set appeared in this vertical section because of the direction; 320°. Different scanlines were used in Location-3 in order to determine fractures density. Applying a certain scanline is dependent on lithology and bed thickness.

The end of the first depositional cycle in the first stratigraphic section shows different fracture densities for Mudstone lithofacies, Siltstone lithofacies, and fine to medium hummocky cross-stratified Sandstone lithofacies. 3.7m scanline was used in order to determine the fractures density (Fig 4.10). The average fractures spacing of the 320° set that appears in this section ranges from 17cm in the Mudstone to 80cm in the fine sandstone (Fig 4.11).

Moving up in the vertical section reveals almost the same trend of fractures with different lithologies. Same lithology units with different fractures density is a result of grain size and bed thickness, therefore spacing between fractures in a lithological bed is the result of bed thickness, where the relation between spacing and bed thickness is inverse.

The end of the second and third depositional cycles in the first section reveals almost the same number of fractures per meter as the end of the first depositional cycle, where the lithology is fine to medium hummocky cross-stratified Sandstone. The very fine to fine sandstone below the end of each depositional cycle reveals more number of fractures per meter due to finer grain size and smaller bed thickness (Fig 4.12). The average fractures spacing in the 320° set that appears in this section ranges from 16cm in the very fine-grained sandstone to 32cm in the fine to medium-grained sandstone (Fig 4.13).

At the top of location-3 outcrop the second set of fractures; 20°NE appeared again next to the set; 320° Showing the two main sets of fractures that developed in the study area (Fig 4.14).

1D fractures density model has been generated against the vertical stratigraphic section of location-3 (Fig 4.15), to clarify the relationship between fractures and different lithologies. The 1D model shows that the fissile shale and Mudstone facies have the most number of fractures per meter, after them comes the siltstone facies, then the hummocky cross-stratified sandstone, and the trough cross bedding sandstone. Bed thickness as shown in the 1D model also affects the fractures trend.

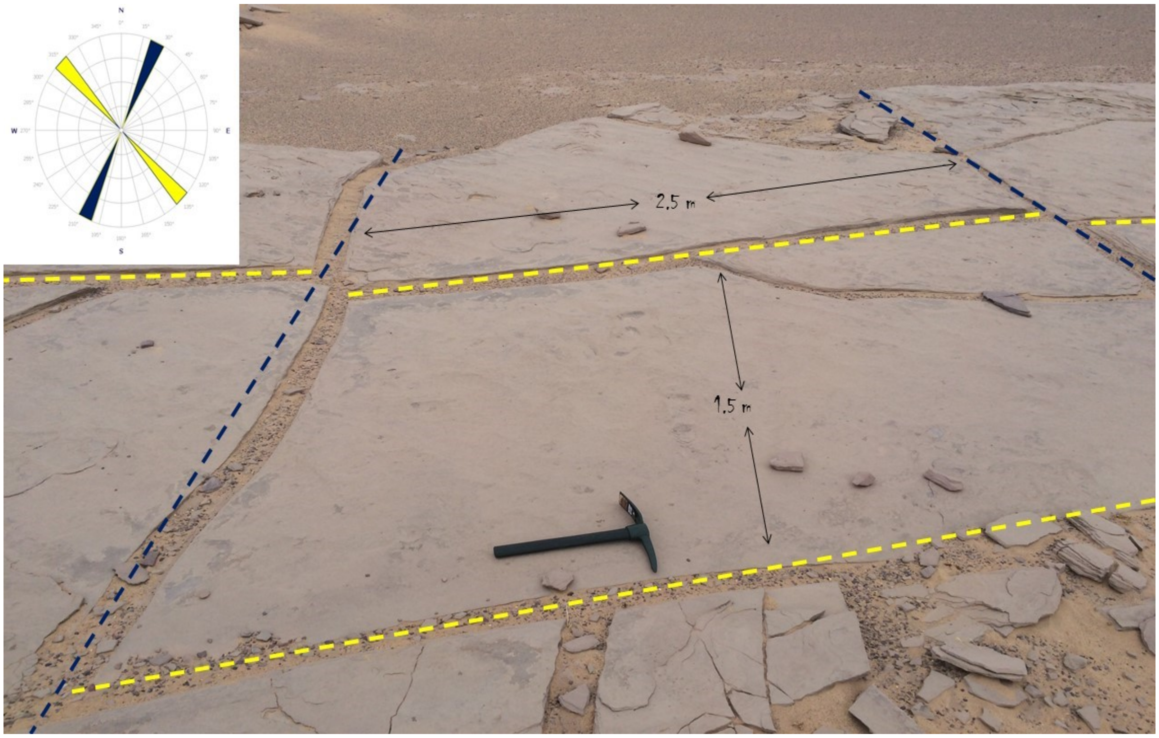

Figure 4-7 Fractures pattern in location-1 (26°56’18” N 43°32’08” E) (Top view).

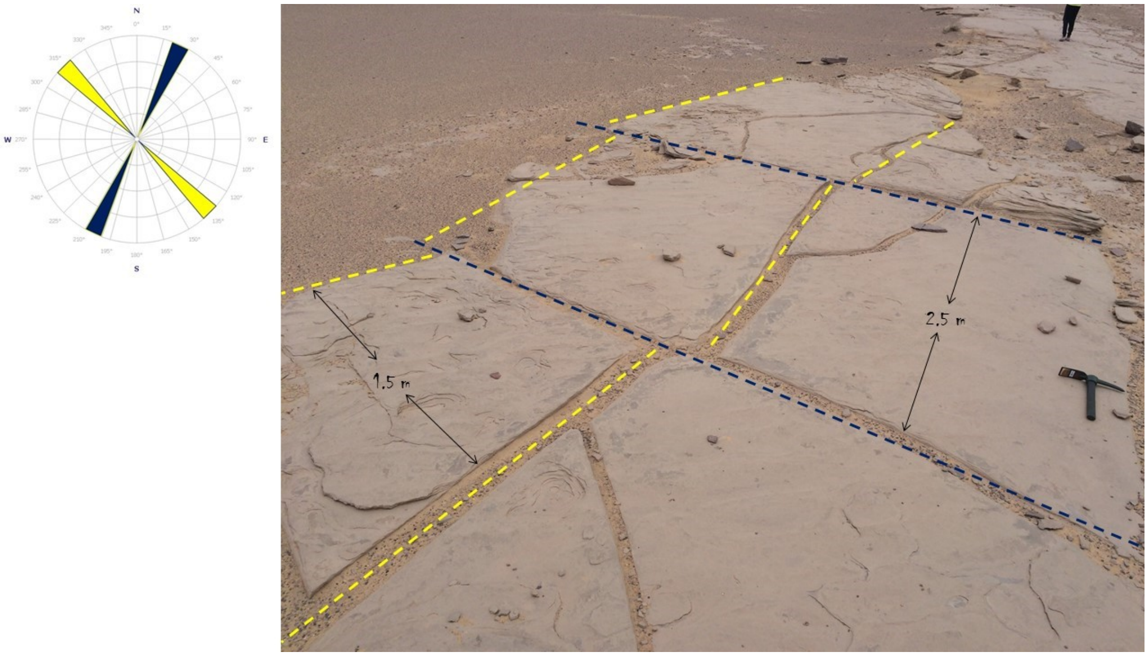

Figure 4-8 Fractures pattern in location-1 (26°56’18” N 43°32’08” E) (Top view).

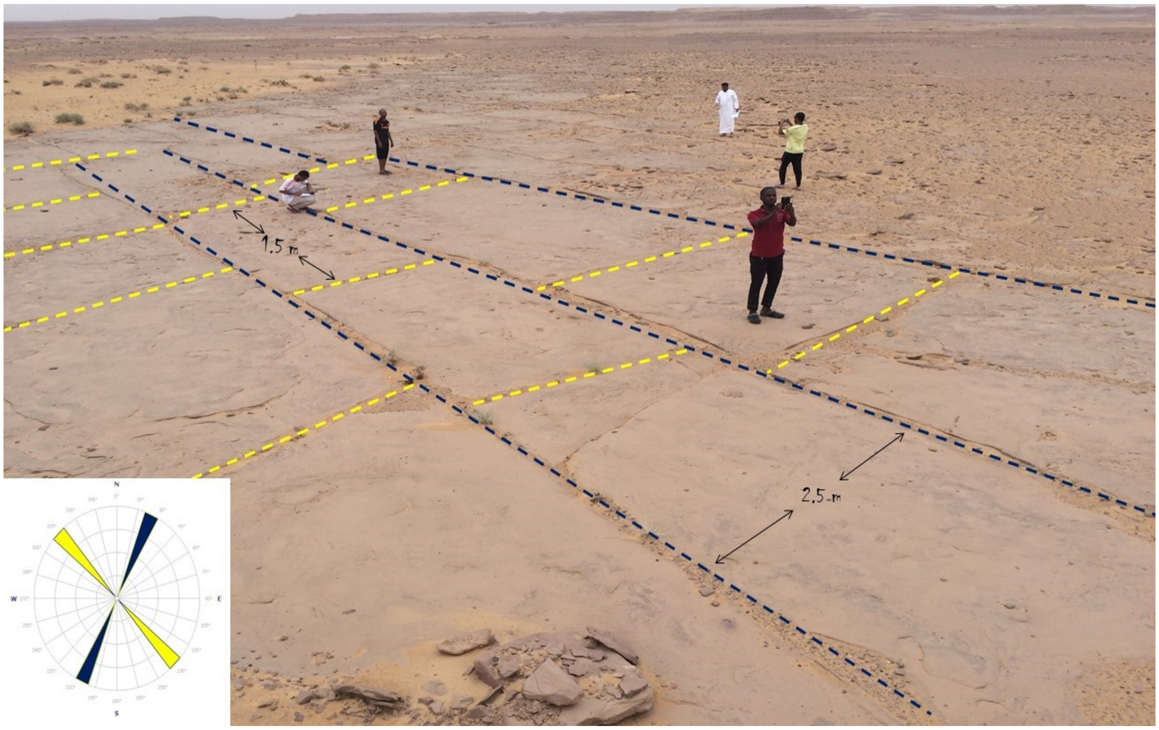

Figure 4-9 Fractures pattern in location-2 (26°56’23.1” N 43°31’55.6” E) (Top view).

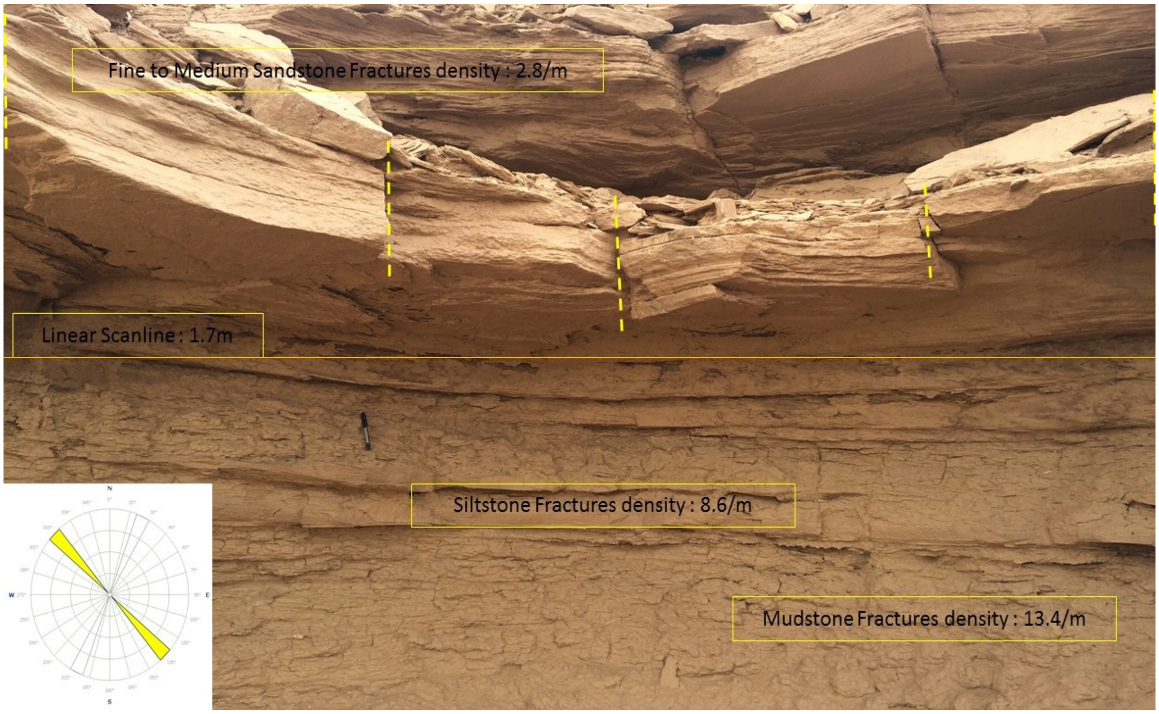

Figure 4-10 Fractures density within different lithologies at the end of the first depositional cycle.

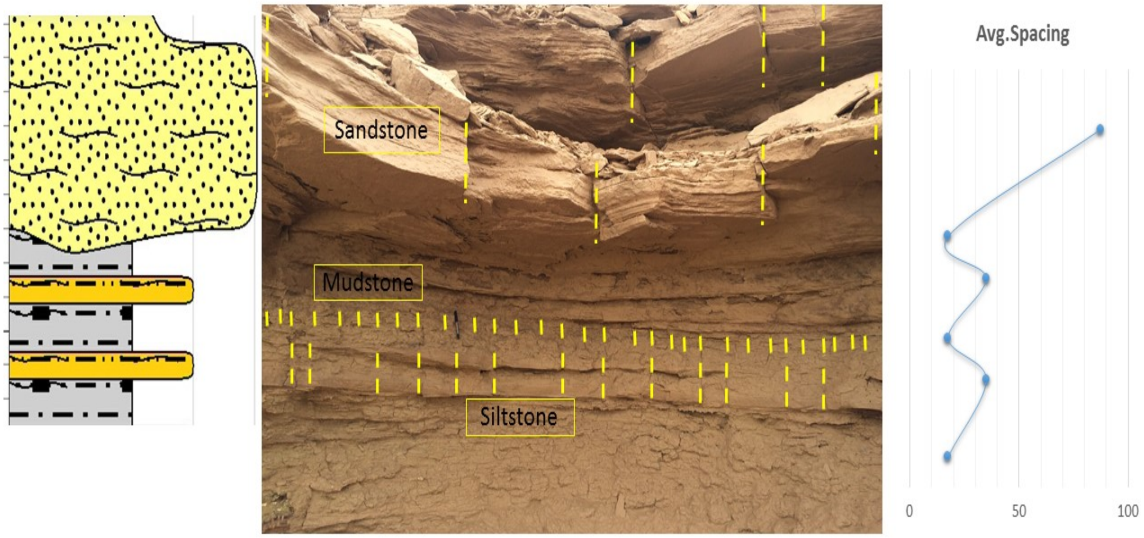

Figure 4-11 Fractures Average spacing within different lithologies at the end of the first depositional cycle.

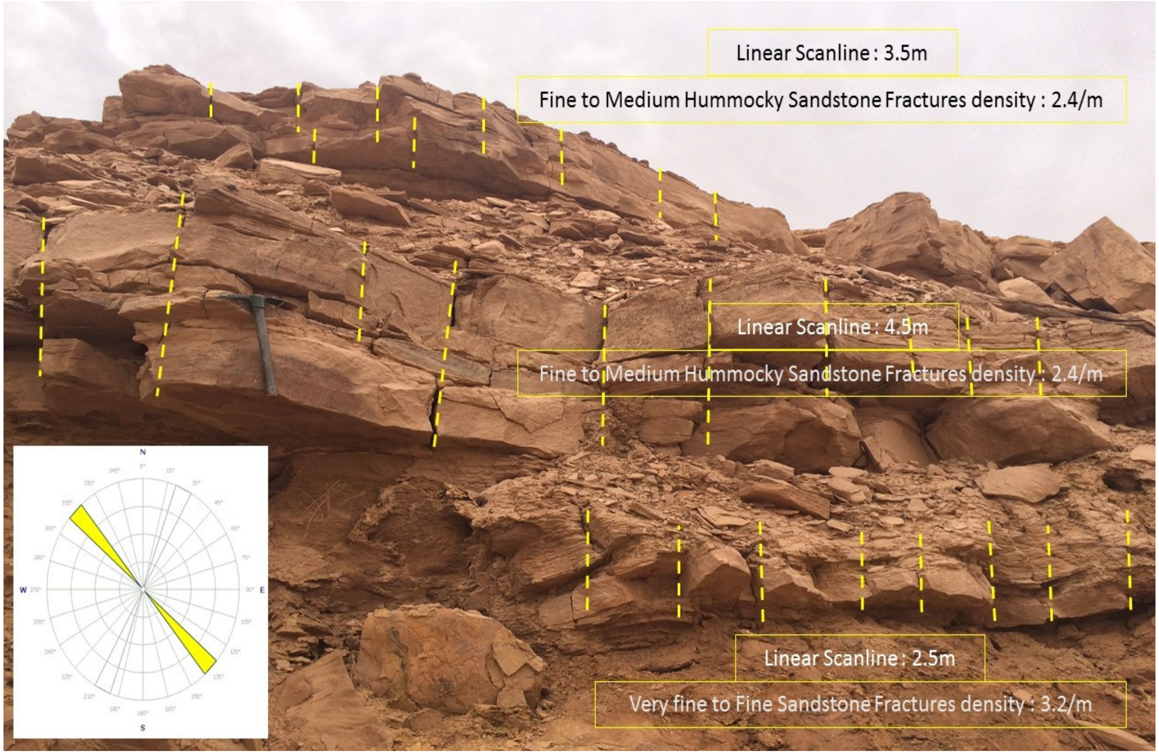

Figure 4-12 Fractures density within same lithology beds with different grain size and bed thickness.

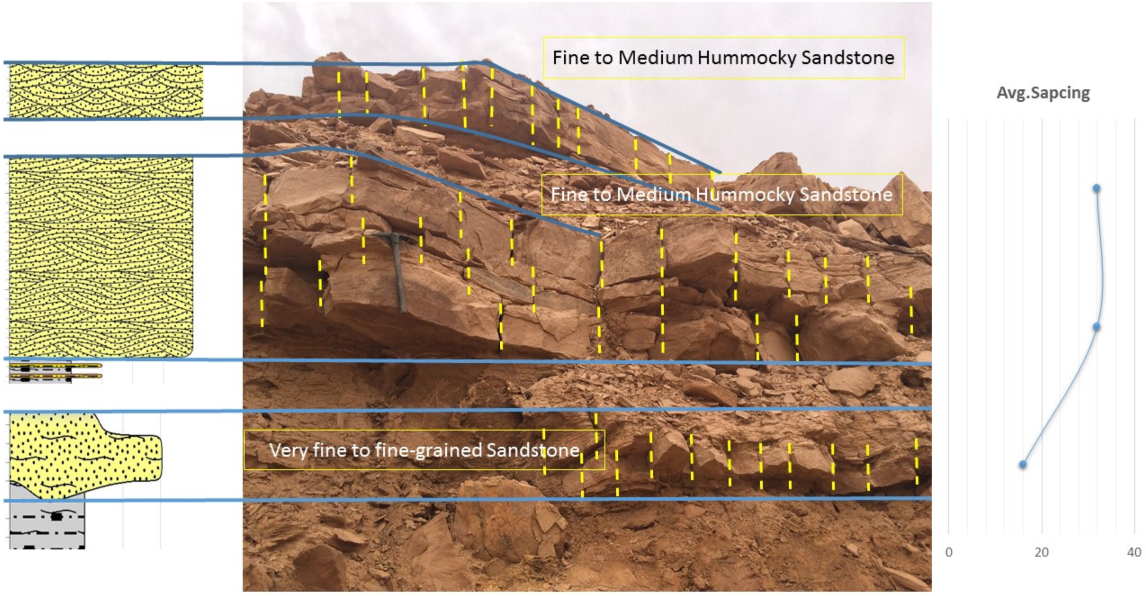

Figure 4-13 Fractures Average spacing within same lithology beds with different grain size and bed thickness.

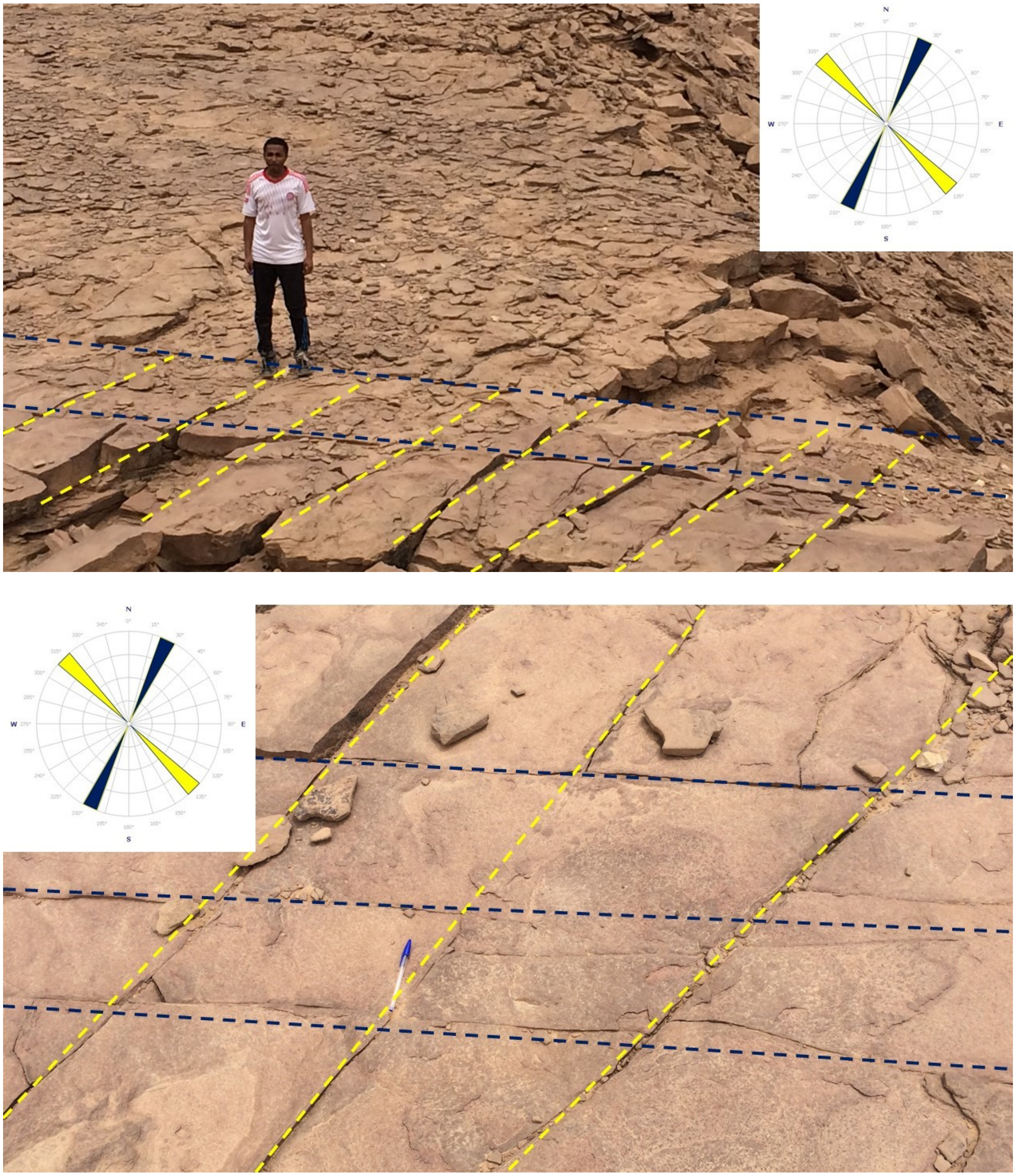

Figure 4-14 The two fracture sets at the top of location-3 outcrop

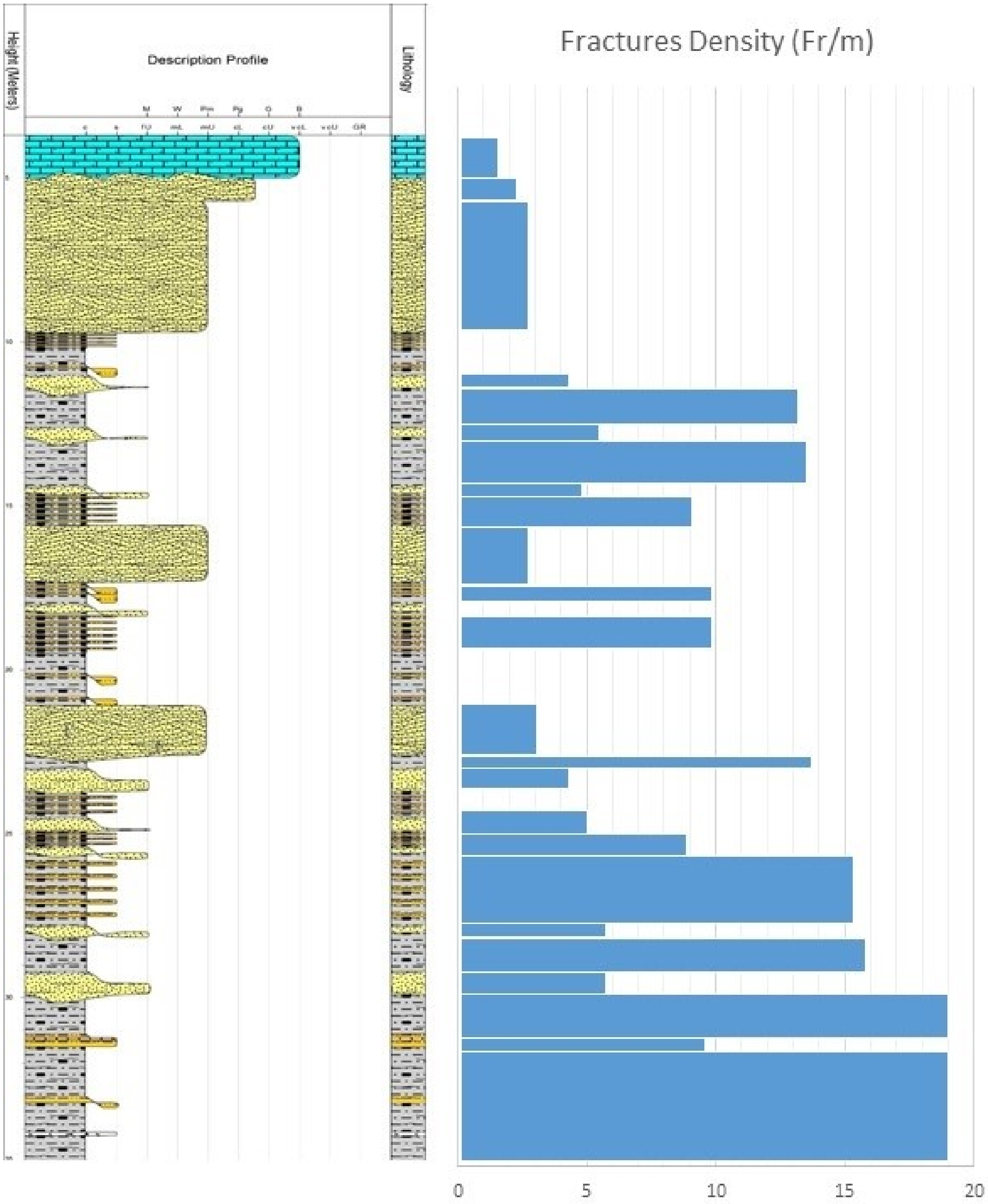

Figure 4-15 1D model of fractures density (320°) correlated to the lithostratigraphic section in location-3.

### 4.2.2 Location 4

Location-4 represents the location of the second vertical section (26°55’40.8” N 43°30’55.2” E). The basal part of location-4 outcrop represents the fissile shale intercalated in some areas with very thin beds of siltstone facies. The fissile shale fractures density is 18.7 fracture per meter, and the thin siltstone beds fracture density is 9.2 fracture per meter (Fig 4.16). The termination degree of fractures between the fissile shale and the siltstone is 54%, and it means that more than half of the fractures are terminated within the fissile shale beds since the fractures per meter are more in these beds. The huge relative number of fractures in these two lithofacies in comparison to the other facies in the upper parts of the outcrop is due to the grain size and/or bed thickness.

In the middle of location-4 outcrop the siltstone facies fracture density becomes a little bit fewer than at the basal part of the outcrop, the fractures density of the siltstone in the middle part of the outcrop is 6.6 fracture per meter in a 2.4m scanline used, and the termination degree of fractures within the siltstone beds is about 30%, where 70% of the fractures are continuing to the other beds with different lithology (Fig 4.17).

The upper parts of location-4 outcrop have been studied from two different direction views in order to see the two main sets in the area; 320° (Fig 4.18) and 20° (Fig 4.20). The sandstone facies in the outcrop shows different trends depending on the grain size and/or the bed thickness, where the very fine-grained sandstones have more number of fractures than the coarser ones. The average fractures spacing in the 320° set ranges from 20cm in the fine-grained sandstone to 30cm in the fine to medium-grained sandstone (Fig 4.19), and the average fractures spacing in the 20° set ranges from 20cm in the very fine-grained sandstone to 120cm in the medium to coarse-grained sandstone (Fig 4.21).

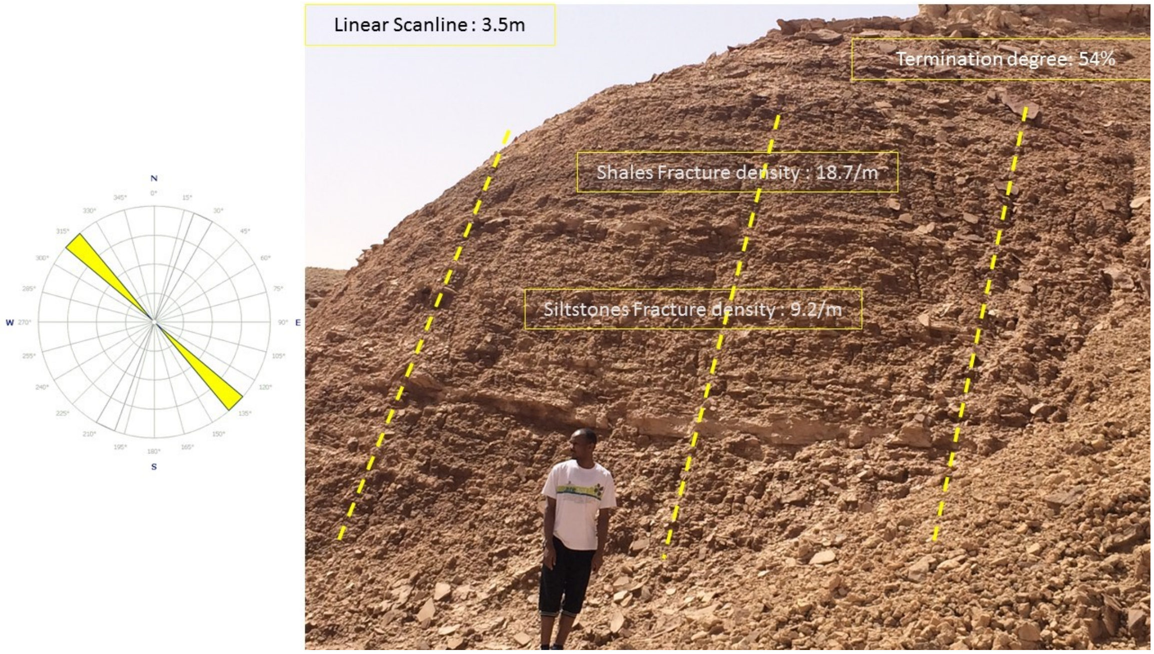

**Figure 4-16 The basal part of location-4 outcrop showing the fractures density within fissile shale and siltstone lithofacies.**

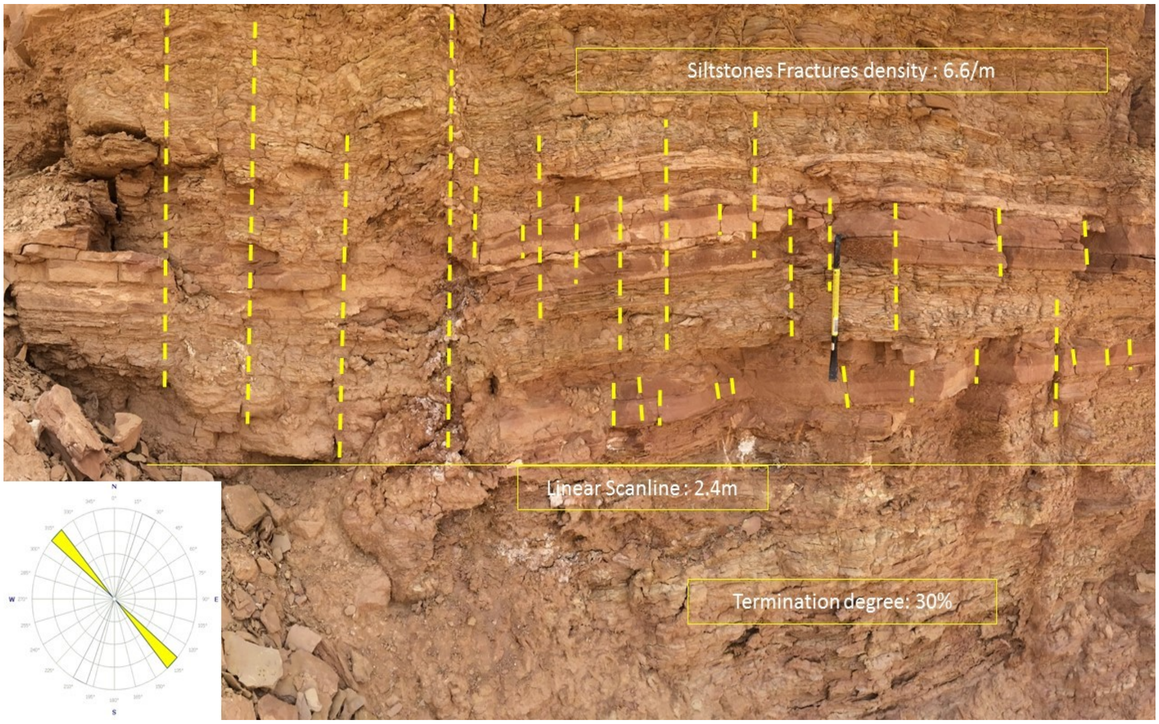

**Figure 4-17 The middle part of location-4 outcrop showing the fractures density within the siltstone lithofacies.**

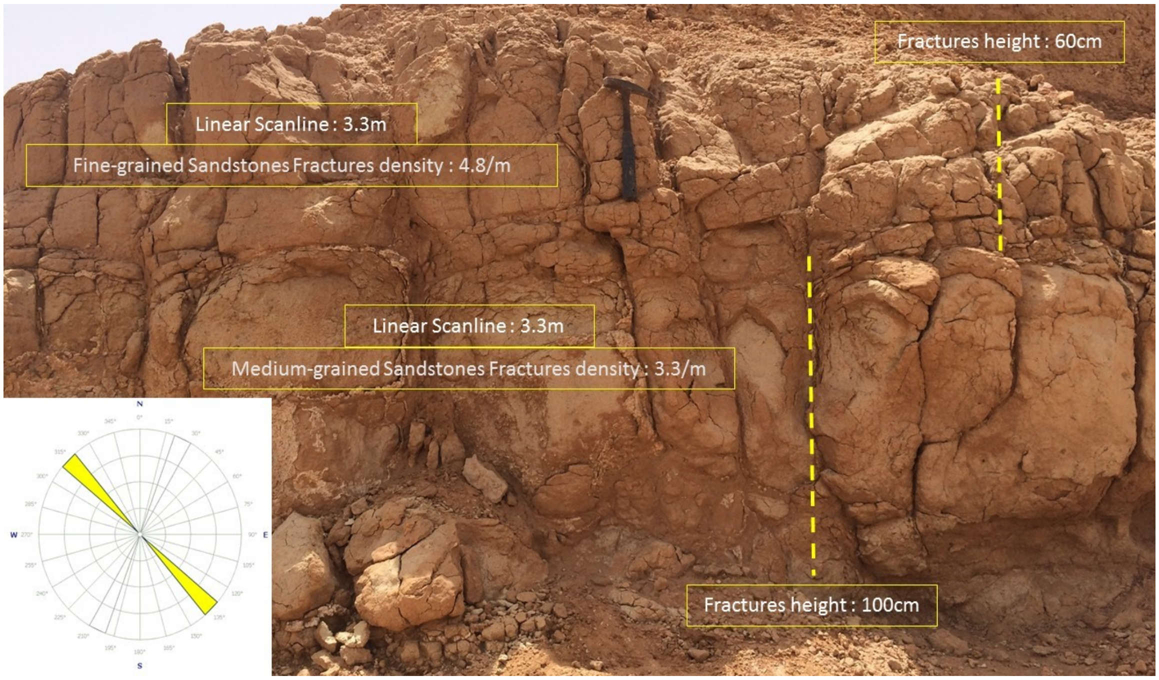

Figure 4-18 The upper part of location-4 outcrop showing the 320NW set within different sandstone lithofacies.

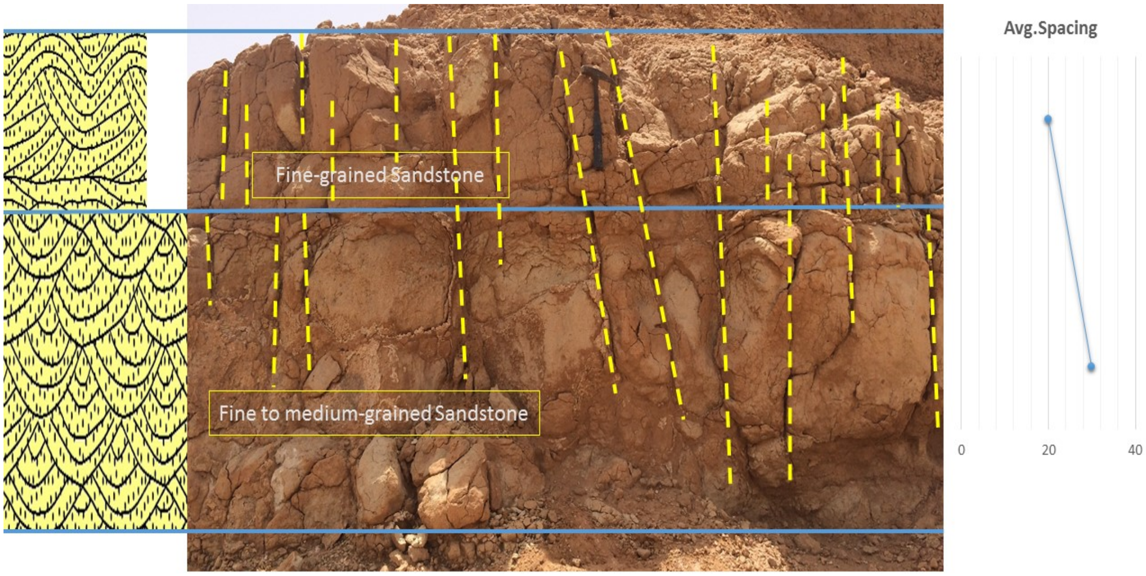

Figure 4-19 Fracture spacing of the 320NW upper part of location-4 outcrop

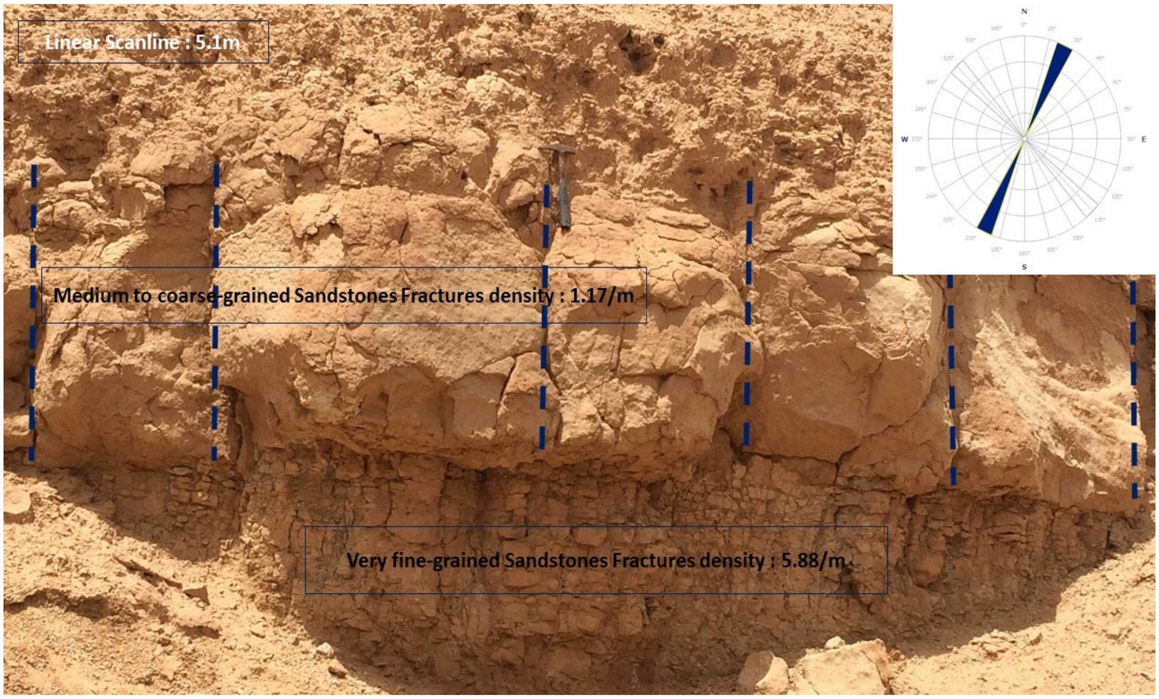

Figure 4-20 The upper part of location-4 outcrop showing the 20NE set within different sandstone lithofacies.

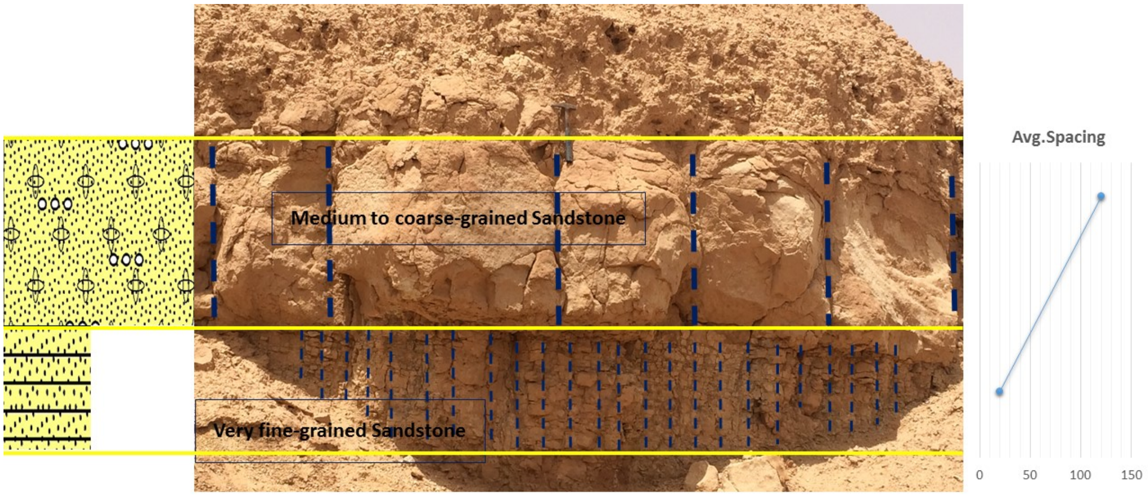

Figure 4-21 . Fracture spacing of the 20NE upper part of location-4 outcrop.

The uppermost part of location-4 outcrop shows the major fracture set; 320° with 0% termination degree, where all fractures are not bounded by any stratigraphic base. The spacing between the major fractures is 1.5m, and the fractures are cutting in all Silurian lithofacies in the study area (Fig 4.22).

1D fractures density model has been generated against the vertical stratigraphic section of location-4 (Fig 4.23), to clarify the relationship between fractures and different lithologies. The 1D model shows that the fissile shale and Mudstone facies have the most number of fractures per meter. Bed thickness as shown in the 1D model also affects the fractures trend.

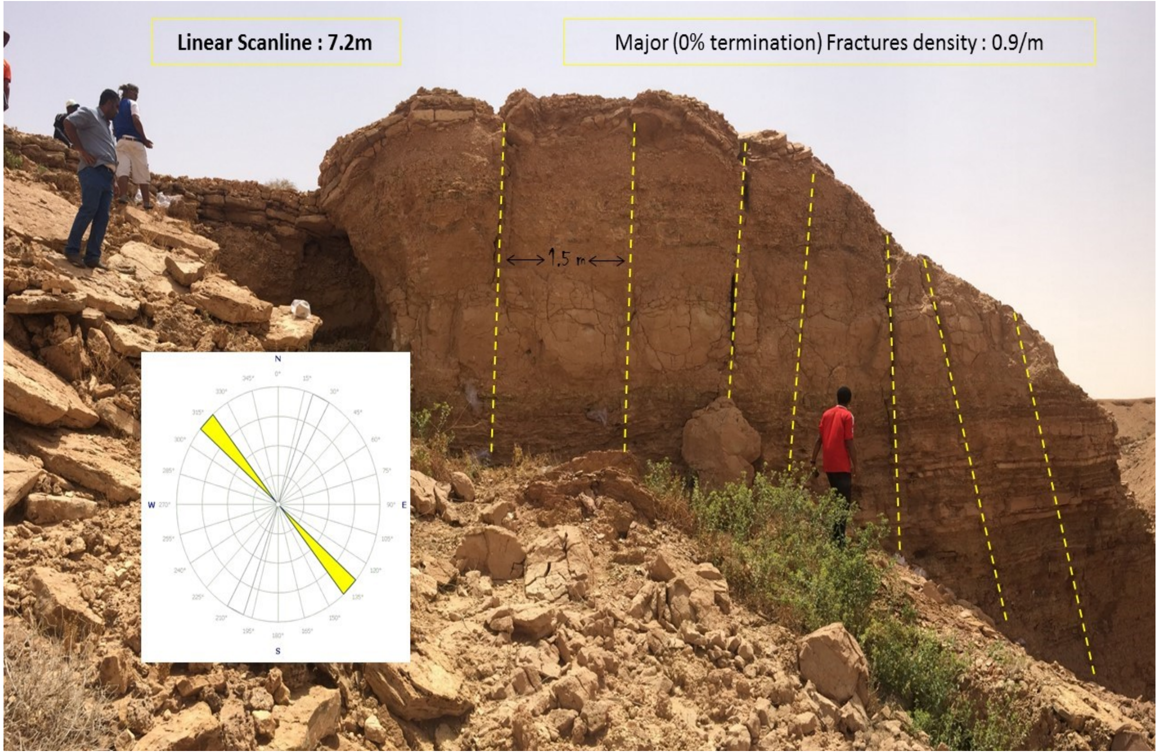

Figure 4-22 The uppermost part of location-4 outcrop showing the major 320° fractures in the study area.

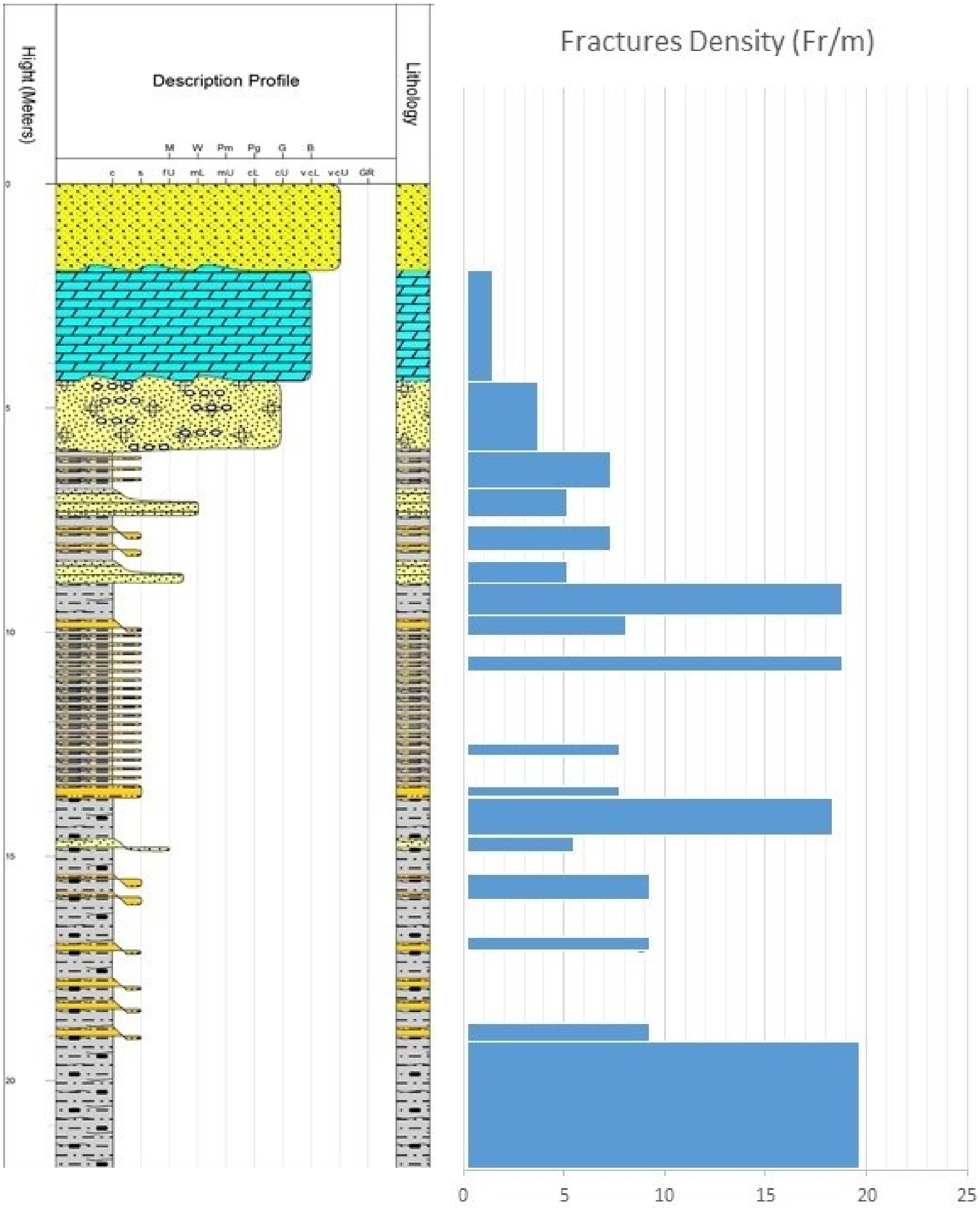

**Figure 4-23 1D model of fractures density (320°) correlated to the lithostratigraphic section in location-4.**

## 4.3 Multi-scale fractures model

The fractures network in the study area has a wide range of properties related to fractures density, length, spacing, height, and termination degree. The conceptual multi-scale model divides the fractures in the study area into 4 orders, it depends on the available data that have been observed from satellite images and field. The model was constructed using the main two sets of fractures in the study area; 320° and 20º, in addition to the other properties discussed earlier in this chapter. The multi-scale model proposes that the fractures in the area are scale-dependent, where the large-scale fractures (Lineaments) are cutting through different lithologies, formations, and members in the study area and the small-scale fractures are not necessarily cutting through different lithologies. Stratigraphic units affect the fractures as described in the (strata-bound vs. non strata-bound) concept described by (Odling et al., 1999).

### 4.3.1 1st order zone

The lineaments that have been traced and interpreted from the Landsat-ETM+ satellite image with a length more than 1000m and regular spacing pattern are defined in the multi-scale model as the first order fractures. The two main sets of fractures in the Landsat-ETM+ satellite image are distributed almost equally along Qusaiba member, Sara formation, and Unayza formation, proposing that the fractures in this regional area are not affected by stratigraphic differences (Non-stratabound), and supposing that the area is a one large mechanical unit (Fig 4.24a).

### 4.3.2 2nd order zone

The fractures that have been traced and interpreted from both spot-7 and Landsat-ETM+ satellite images with a length less than 1000m and regular spacing pattern are defined in the multi-scale model as the second order fractures. The two main sets of fractures in the Spot-7 satellite image are distributed along Qusaiba member, where some few fractures are bounded by stratigraphic bases and most of the fractures are not (Fig 4.24b).

### 4.3.3 3rd order zone

The major fractures that have been observed in the field with a length range from 10 to 40 meters, and cutting through all stratigraphic units are defined in the multi-scale model as the third order fractures. The two main sets in the area; 320º and 20º are clearly observed along the vertical outcrops in this zone, with a larger spacing pattern between the 20º fractures set (Fig 4.24c).

### 4.3.4 4th order zone

The small-scale fractures that have been observed and studied in the field with a length range from cm's to m's, and strongly affected and controlled by stratigraphic boundaries (Strata-bound) are defined in the multi-scale model as the fourth order fractures. These fractures are concentrated in the fissile shale and mudstone lithofacies in the lower part of the stratigraphic sections, and they propose different mechanical units in the area. Sandstone units, when compared to other units regarding the distribution of the forth order fractures, are found to be more homogeneous, with a highly systematic pattern (Fig 4.24d) and (Fig 4.25).

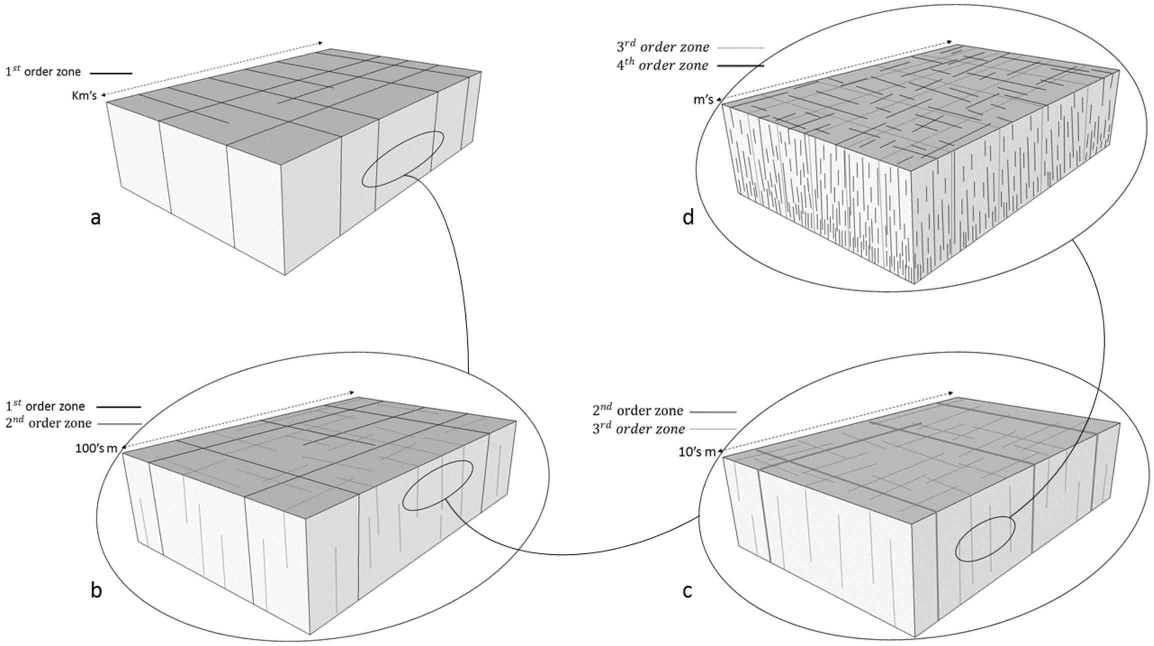

**Figure 4-24 Multi-scale model showing the relationships between: a) First order fractures, b) Second order fractures, c) Third order fractures, and d) Fourth order fractures.**

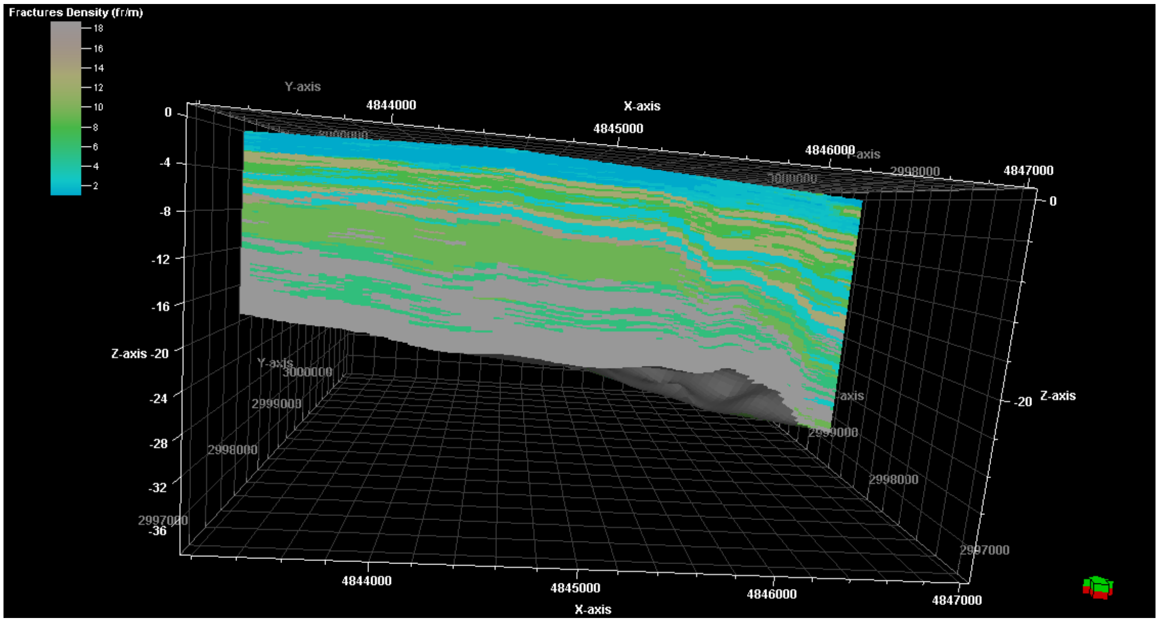

**Figure 4-25 3D geostatistical model viewed from the South shows the distribution of the small-scale Stratabound fractures (320°) in Qusaiba shale member in the study area. (Fractures density were assigned as numeric values into the lithofacies model).**

## 4.4 Local fault-propagation fold

In the North-eastern part of the study area, a local fault-related fold was observed in the satellite image, where same age rocks were not all deformed (Fig 4.27). Faulting evidences have been observed in the field; heavy fault-breccia (Fig 4.29) and (Fig 4.30), horizontal and dipping layers of the same rocks near each other (Fig 4.31), and the existence of ferruginous rocks (Fig 4.32). Fault-propagation fold is a fold associated with the fault tip (Fossen, 2010). The fold in the study area is most likely related to Najd Fault System.

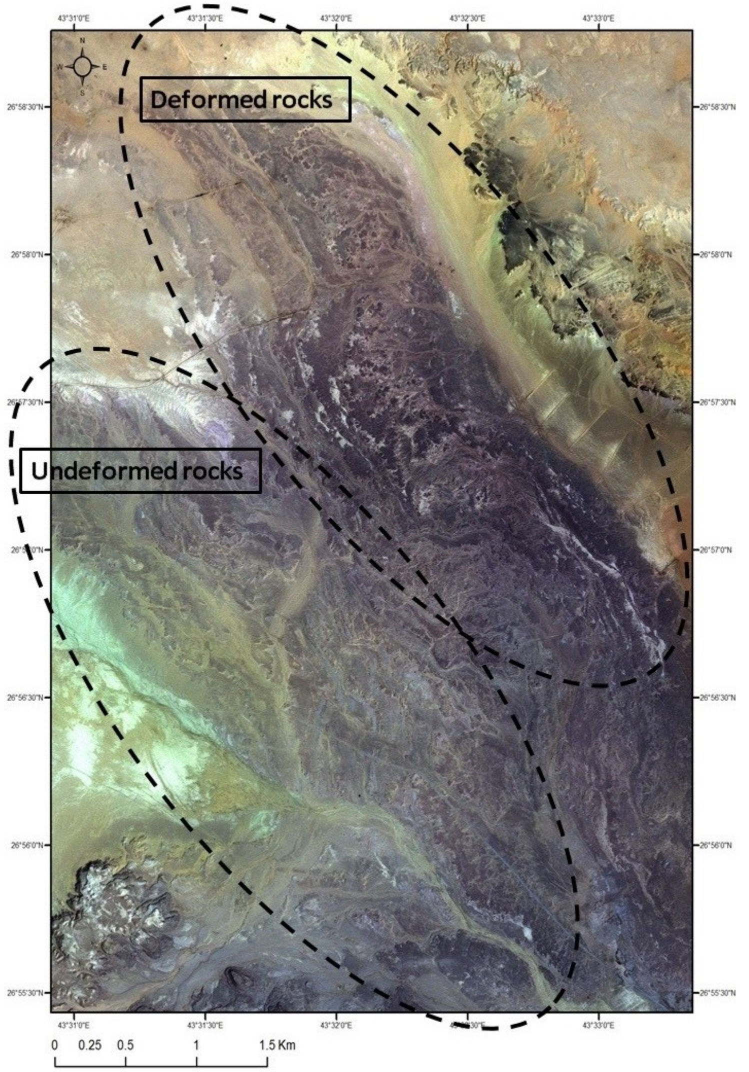

Figure 4-26 The border between deformed and undeformed rocks of Qusaiba shale member in the study.

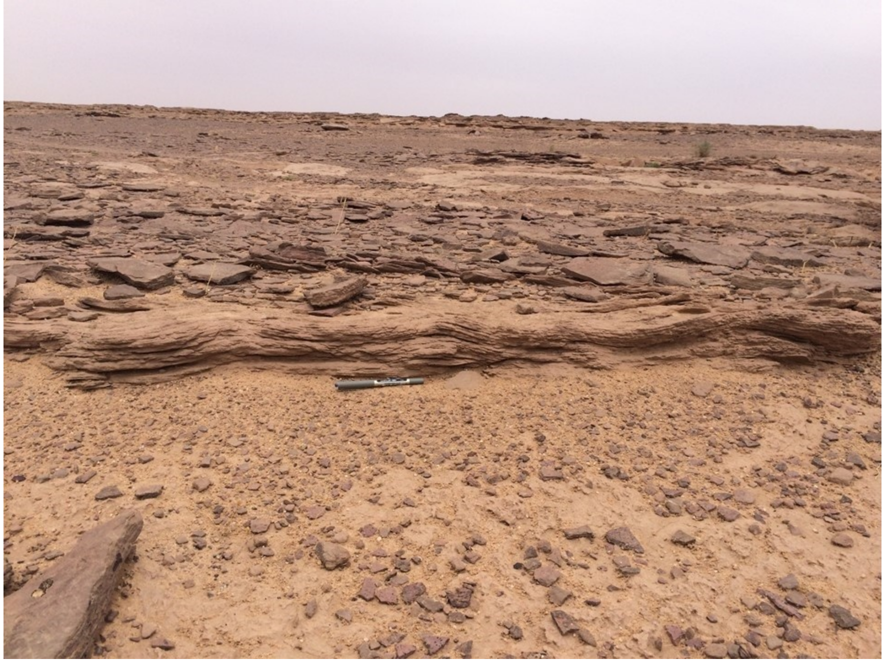

Figure 4-27 Fault-related breccia in the deformed part of the study area.

Figure 4-28 Fault-related breccia in the deformed part of the study area.

Figure 4-29 Horizontal and dipping layers of the same rocks near the fault line in the study area.

Figure 4-30 Ferruginous sandstone rock near the fault line in the study area.

Field investigations confirmed the existence of the fold that was observed in the large scale Spot-7 satellite image, by finding many different scales mimic folds in the study area near the fault line (Fig 4.33) to (Fig 4.36). Geological compass has been used in order to read trend and plunge directions in 12 locations of dipping layers (Fig 4.37) and (Fig 4.38) in the deformed part of the study area (Table 4.3). Constructing a stereonet diagram confirmed the fold axis that was read in the large (satellite image) and small (Mimic) folds as 40º North-East (Fig 4.39).

Table 4-3 Trend and plunge directions of 12 dipping layers in the study area.

| Trend direction | Plunge direction | Coordinates |
|---|---|---|
| 240 | 42 | 43°32'38.926"E 26°57'11.985"N |
| 260 | 51 | 43°32'48.178"E 26°57'17.81"N |
| 230 | 43 | 43°32'33.444"E 26°57'24.32"N |
| 165 | 52 | 43°32'15.969"E 26°57'23.292"N |
| 150 | 65 | 43°32'27.962"E 26°57'39.396"N |
| 140 | 73 | 43°32'14.599"E 26°57'34.599"N |
| 210 | 40 | 43°32'21.109"E 26°57'48.99"N |
| 220 | 42 | 43°31'54.726"E 26°57'55.5"N |
| 250 | 48 | 43°32'14.599"E 26°58'5.094"N |
| 145 | 70 | 43°31'44.104"E 26°57'34.257"N |
| 155 | 60 | 43°32'34.129"E 26°57'34.942"N |
| 160 | 60 | 43°32'39.954"E 26°57'5.132"N |

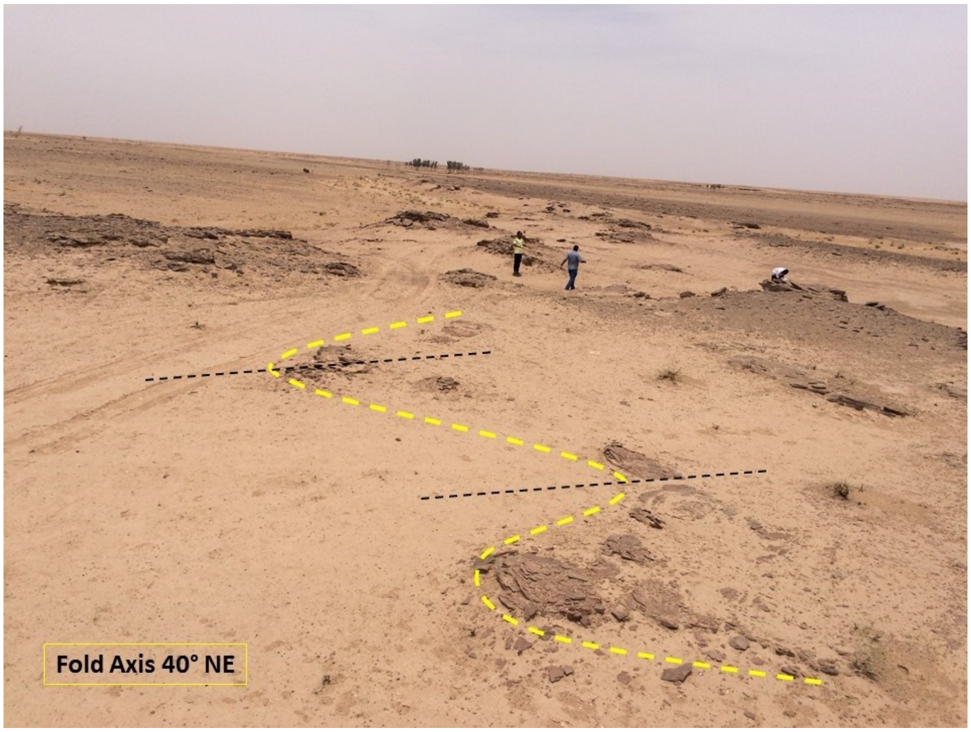

Figure 4-31 Folded shale rocks in the deformed part of the study area.

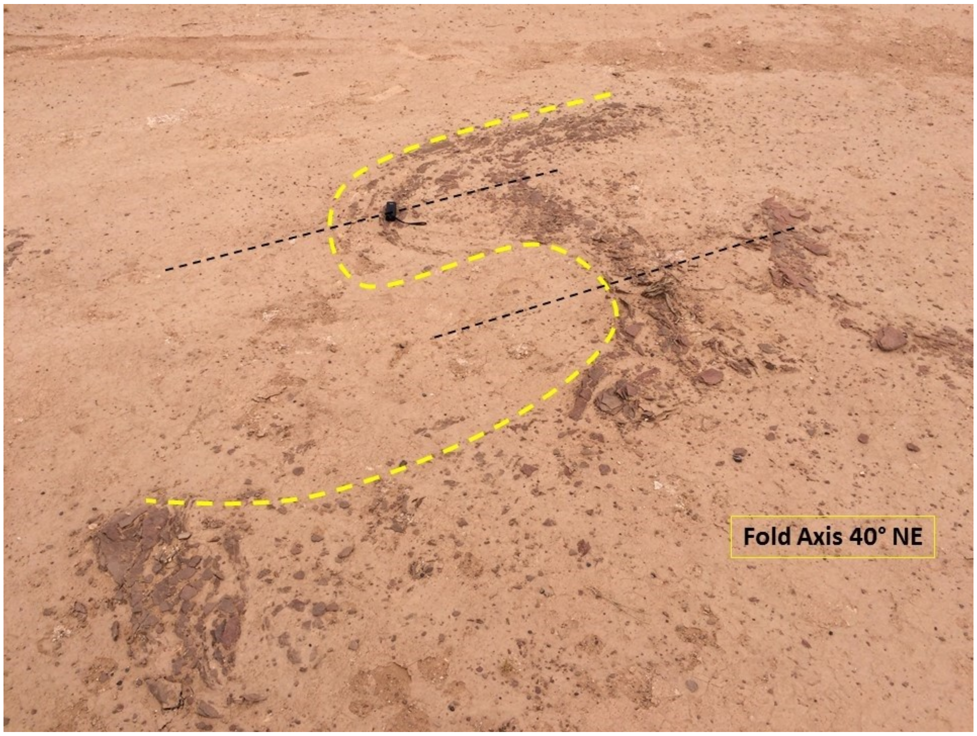

Figure 4-32 .36. Folded shale rocks in the deformed part of the study area.

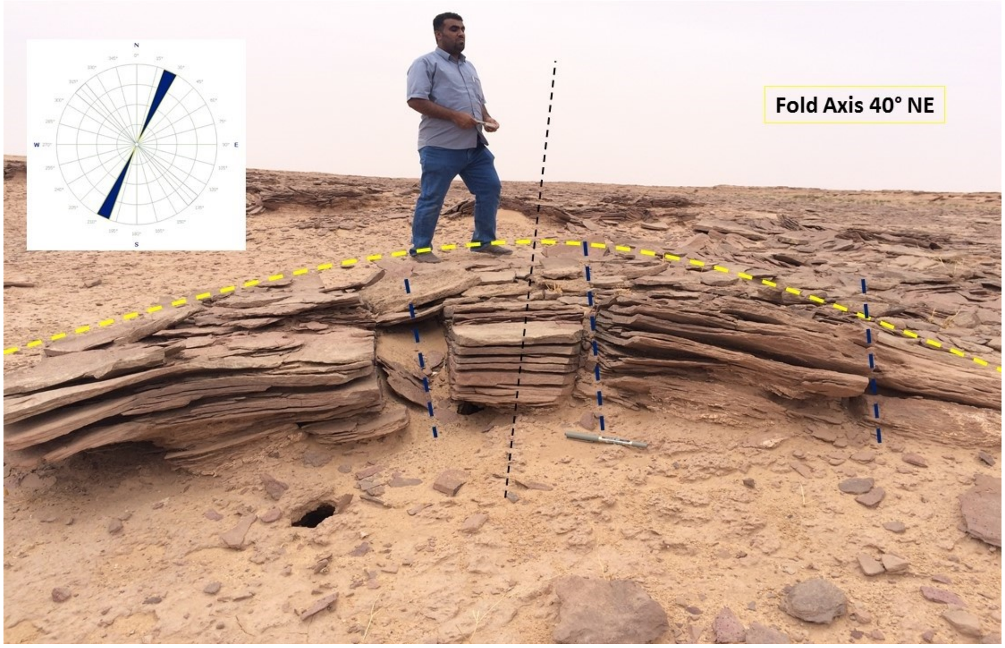

Figure 4-33 Folded shale rocks in the deformed part of the study area.

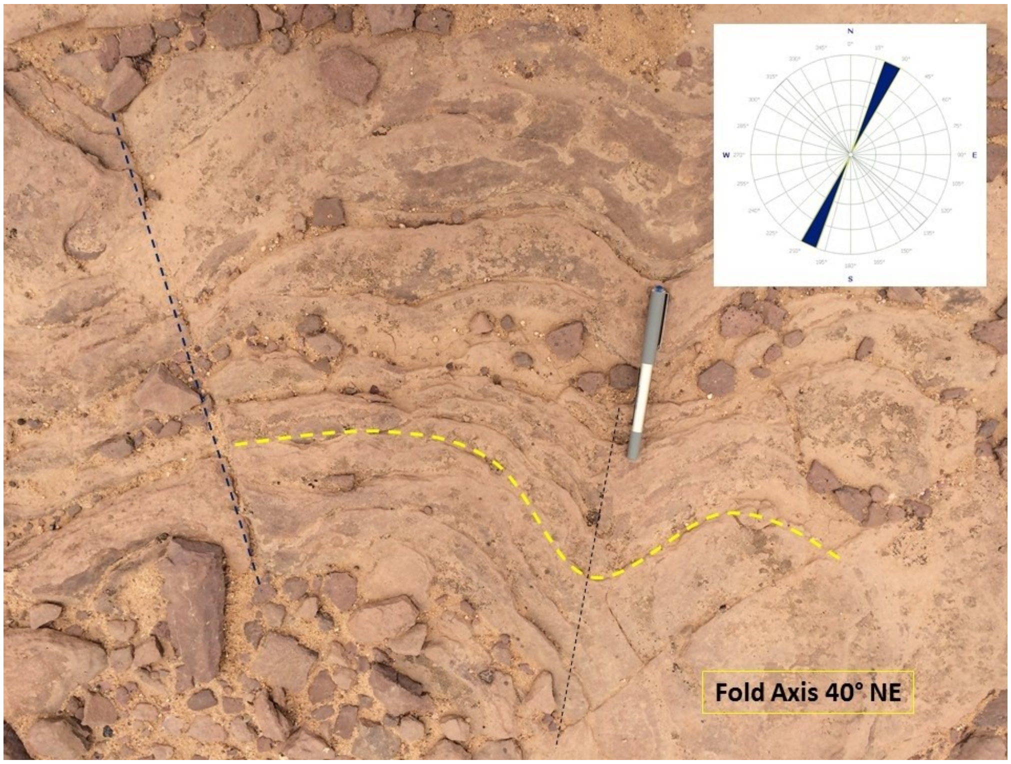

Figure 4-34 Small scale folds in the deformed part of the study area.

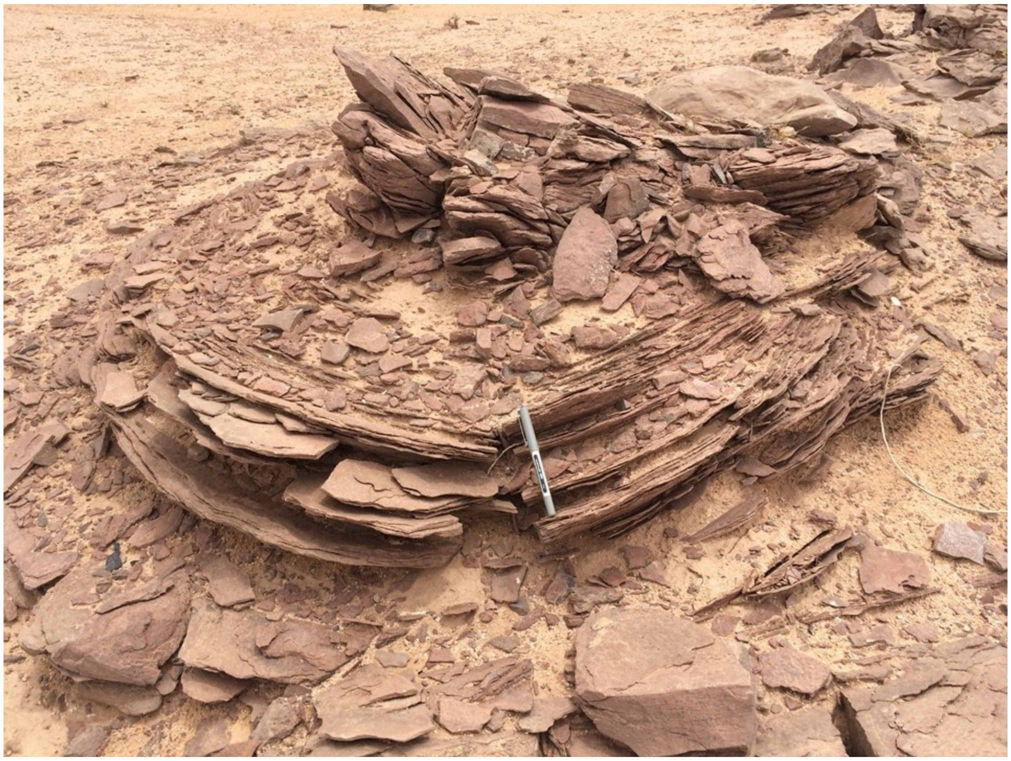

Figure 4-35 Dipping shale layers in the deformed part of the study area.

Figure 4-36 Dipping shale layers in the deformed part of the study area

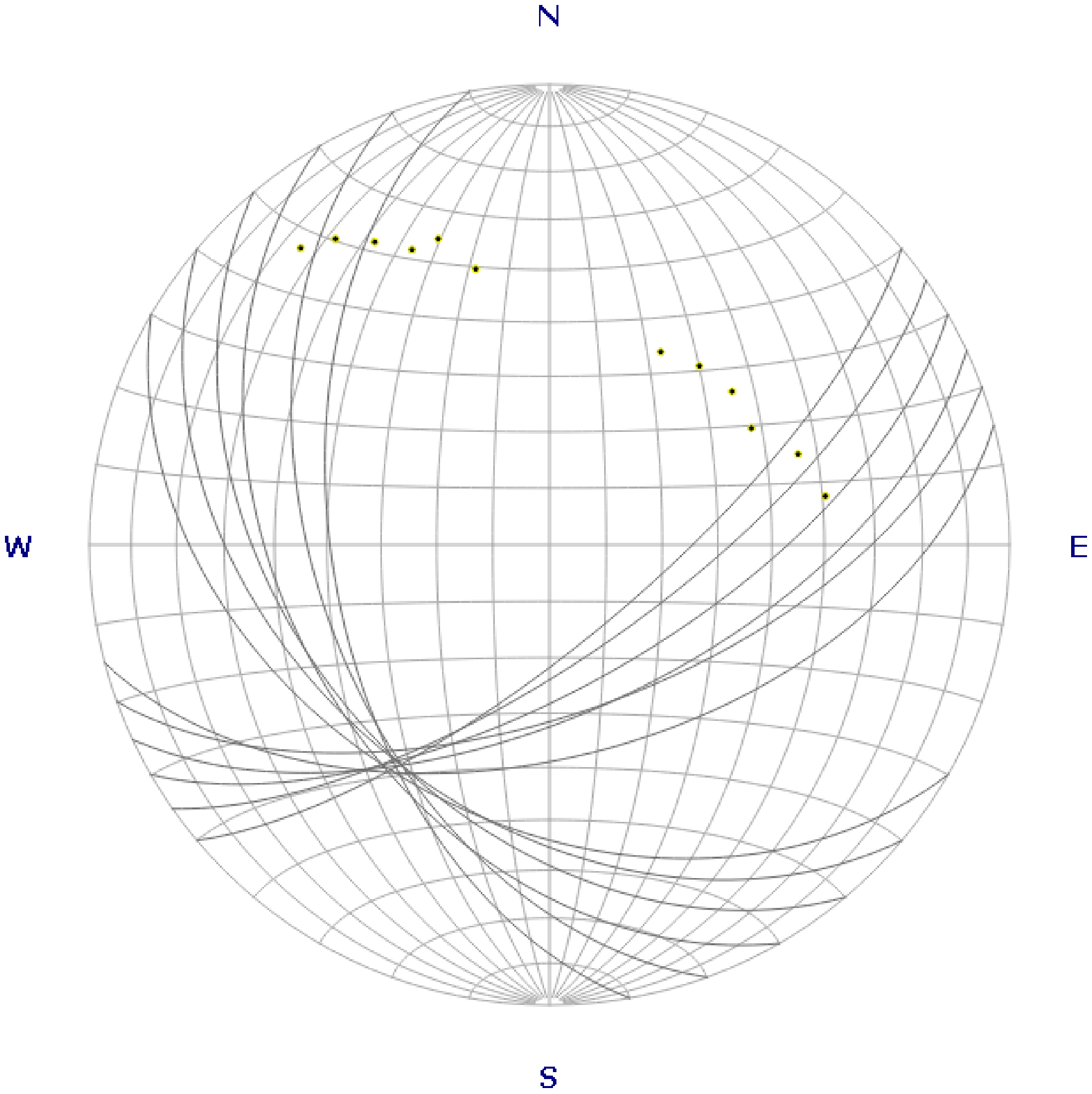

Figure 4-37 Stereonet diagram showing that the axis trend of the fold in the study area is 40º.

# CHAPTER 5

# Geomechanical and Petrophysical Properties

## 5.1 Lithological units

As discussed previously in chapter three, the study area is characterized by 5 main lithological units; fissile shale, bioturbated mudstone, very fine-grained micaceous siltstone, very fine to fine-grained hummocky cross-stratified sandstone, and fine to medium-grained trough cross-stratified sandstone. The vertical sections located in the study area (Fig 5.1) defines the five lithological units, that have been divided based on sedimentology (Thin sections, Scanning electron microscope (SEM), XRD, XRF), porosity, and spectral gamma ray.

## 5.2 Vertical successions and 1D models

Two outcrop locations have been studied in order to define lithological and geomechanical units in the study area. Vertical section-1 (Fig 5.2) shows the cycles of deposition in Qusaiba shale member in a very clear way and is characterized by the five main lithological units. Vertical section-2 (Fig 5.3) Shows the three depositional cycles of Qusaiba shale member with a smaller thickness for each cycle, and the grains of the lithological units are a bit coarser than how it was in vertical section-1, and that proposes more far location from the basin. Spectral gamma ray and Schmidt hammer readings were taken in the field at the same locations, in which samples have been taken. The general trend of Uranium (U) and Thorium (Th) is decreasing as we go up in both vertical sections (Fig 5.4) and (Fig 5.5), but potassium (K) is increasing as we go up (Fig 5.4) and (Fig 5.5). Schmidt hammer readings of rebound number are also increasing towards the top of the vertical sections (Fig 5.6). The distribution of the Schmidt hammer readings over the study area is shown in a 3D geostatistical model (Fig 5.7). The highest readings of Uranium occurred in the fissile shale and Mudstone lithofacies, due to the dense presence of organic matter, micaceous siltstone gave moderate readings, as the organic matter is not completely flushed out from it, and the sandstone facies gave the lowest readings of Uranium (Fig 5.4) and (Fig 5.5.). Potassium (K) readings in both vertical sections were mainly determined by the occurrence of feldspar minerals. The range of readings, in general, was low (0 % – 0.28 %), but the lithological diversity was clear between different lithofacies (Fig 5.4) and (Fig 5.5). Schmidt hammer readings were at the peak in Hummocky stratified sandstone and trough cross-stratified sandstone, a little bit less in the micaceous siltstone, and at its lowest readings in the fissile shale and mudstone lithofacies (Fig 5.6) and (Fig 5.7). These results suggest that the sandstones lithofacies have the higher penetration resistance and surface hardness.

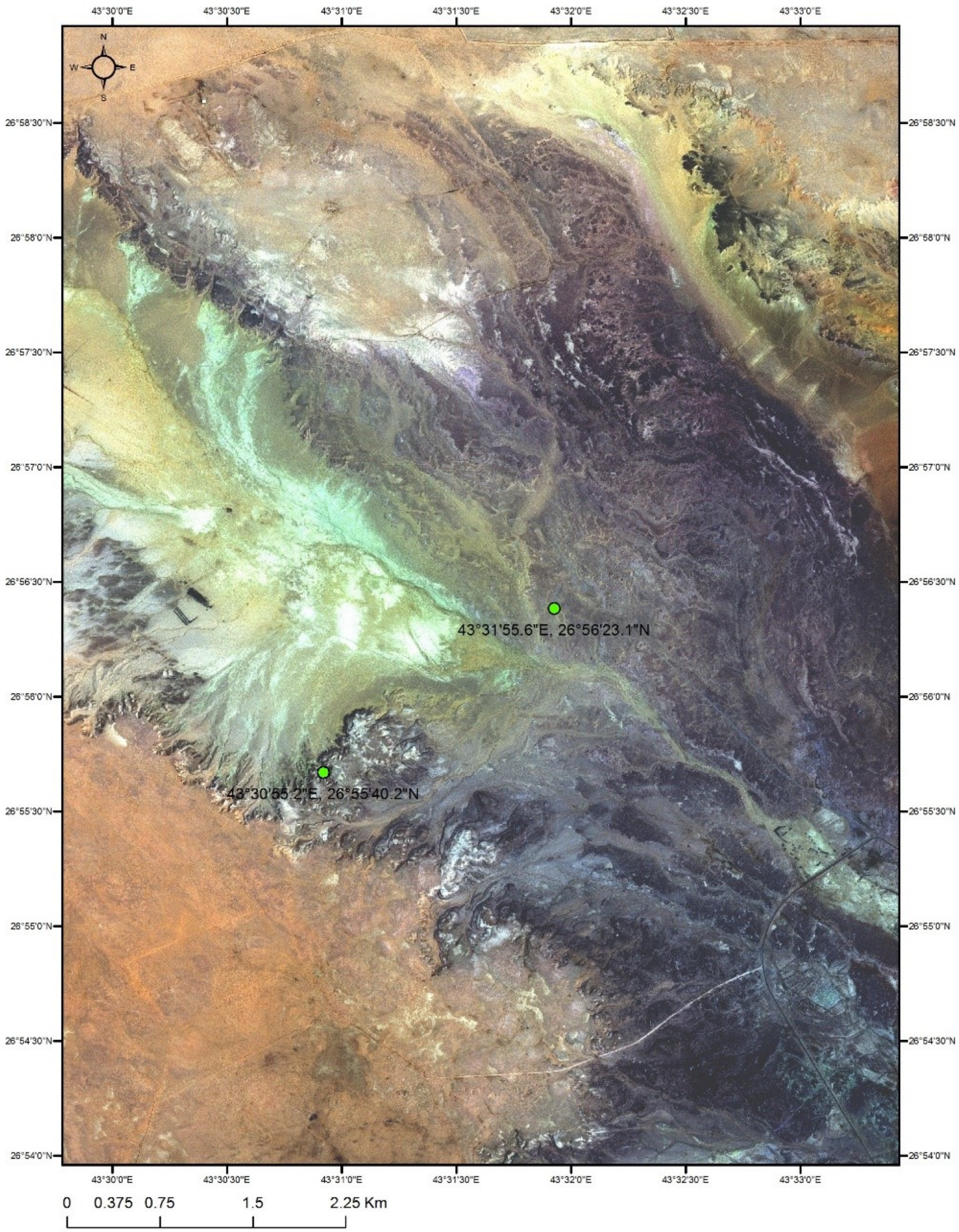

**Figure 5-1 Spot-7 satellite image showing the location of the study area. Green circles indicate the locations of the two main outcrops.**

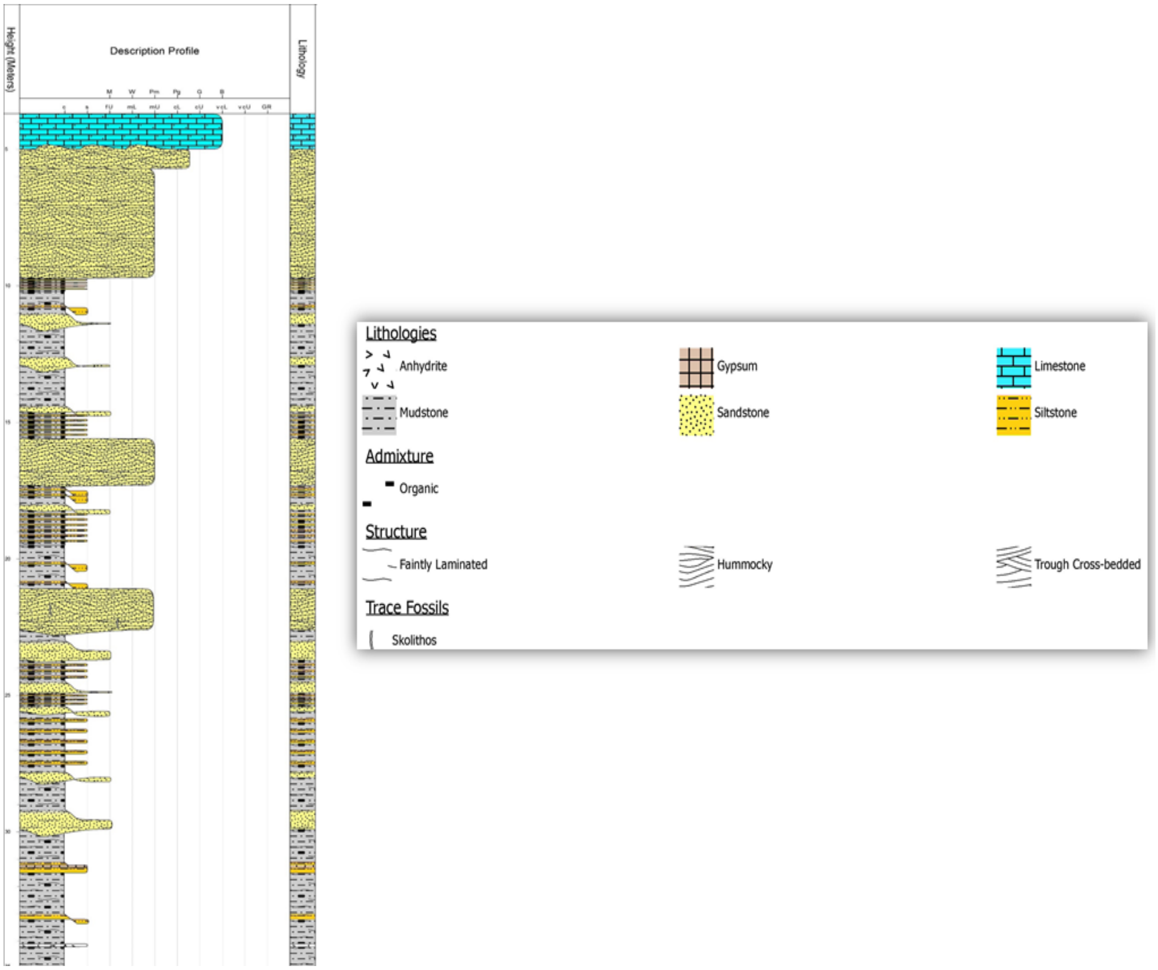

**Figure 5-2 Vertical lithostratigraphic section-1 showing the various lithofacies, sedimentary structures, and mineralogy.**

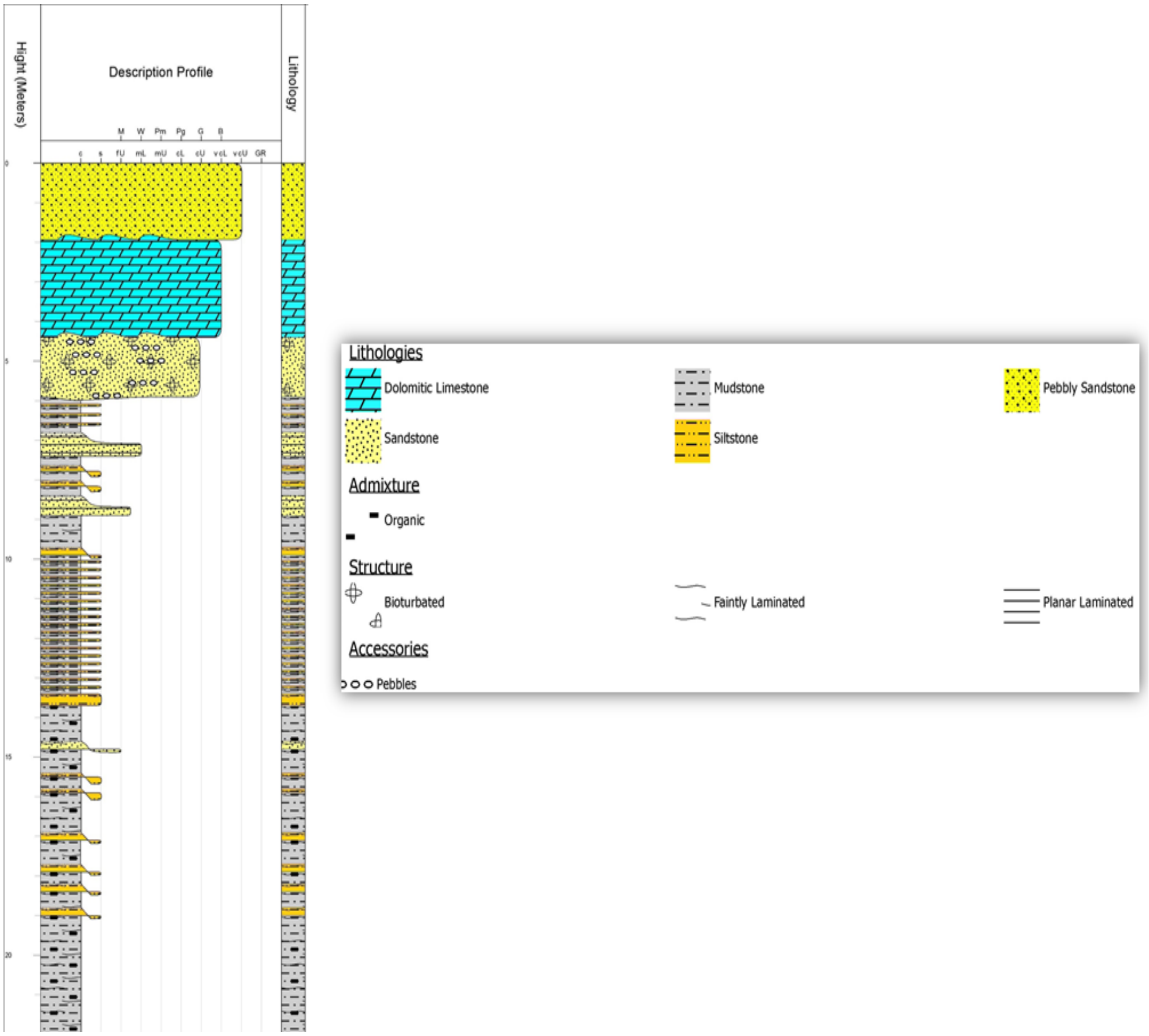

Figure 5-3 . Vertical lithostratigraphic section-2 showing the various lithofacies, sedimentary structures, and mineralogy.

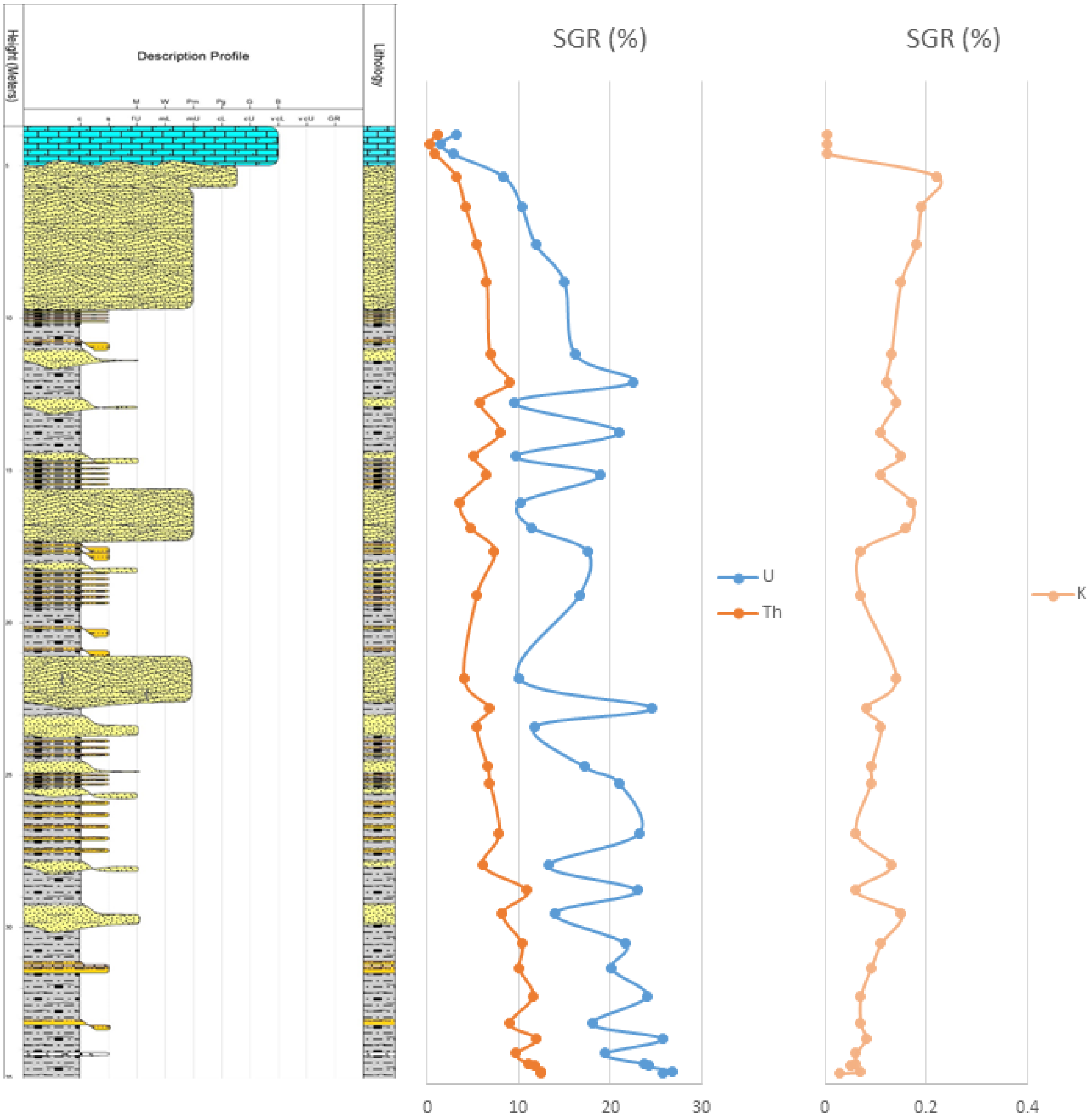

Figure 5-4 Vertical lithostratigraphic section-1 showing the various lithofacies, sedimentary structures, and Gamma Ray readings (U, Th, and K).

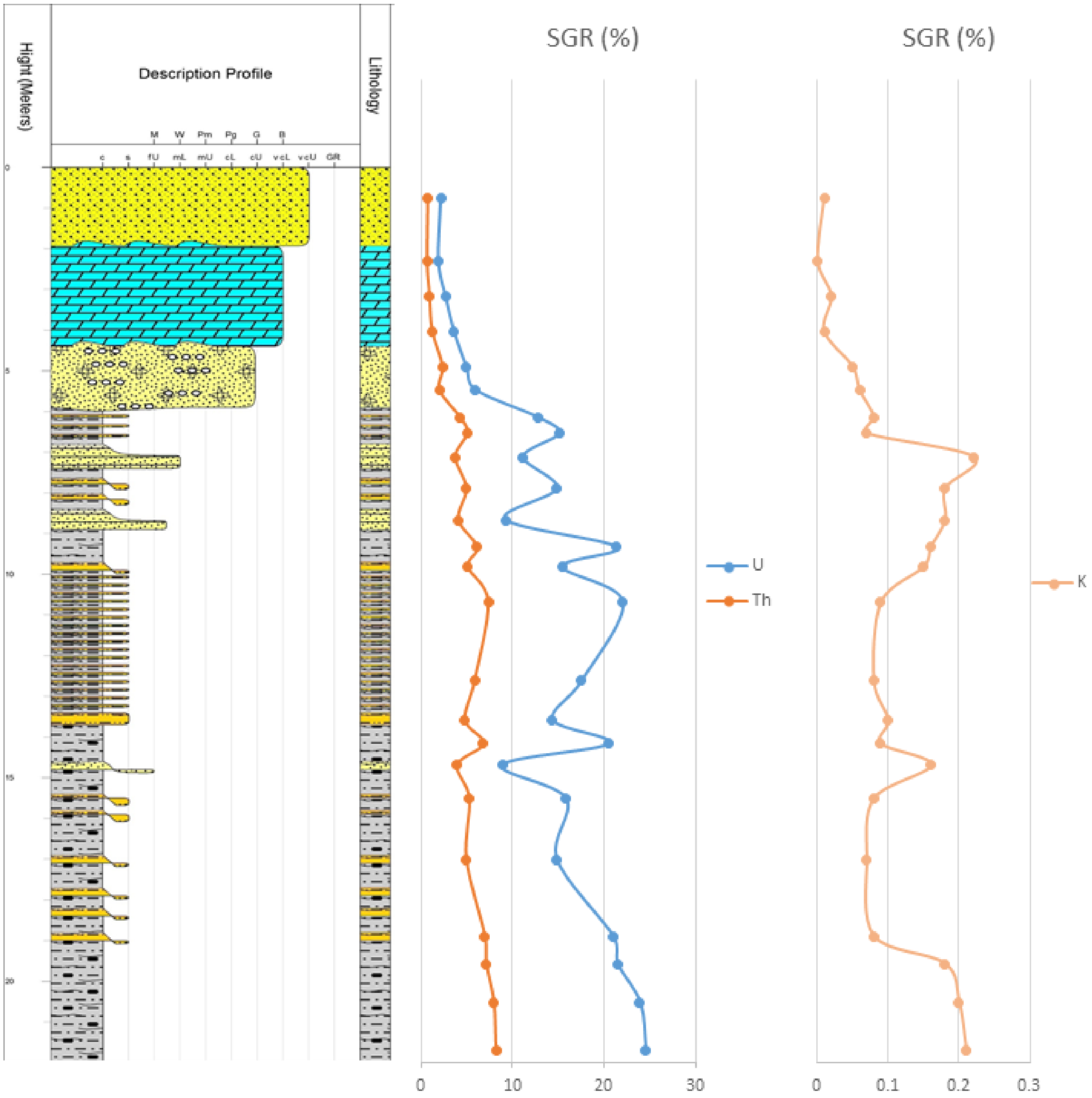

Figure 5-5 Vertical lithostratigraphic section-2 showing the various lithofacies, sedimentary structures, and Gamma Ray readings (U, Th, and K).

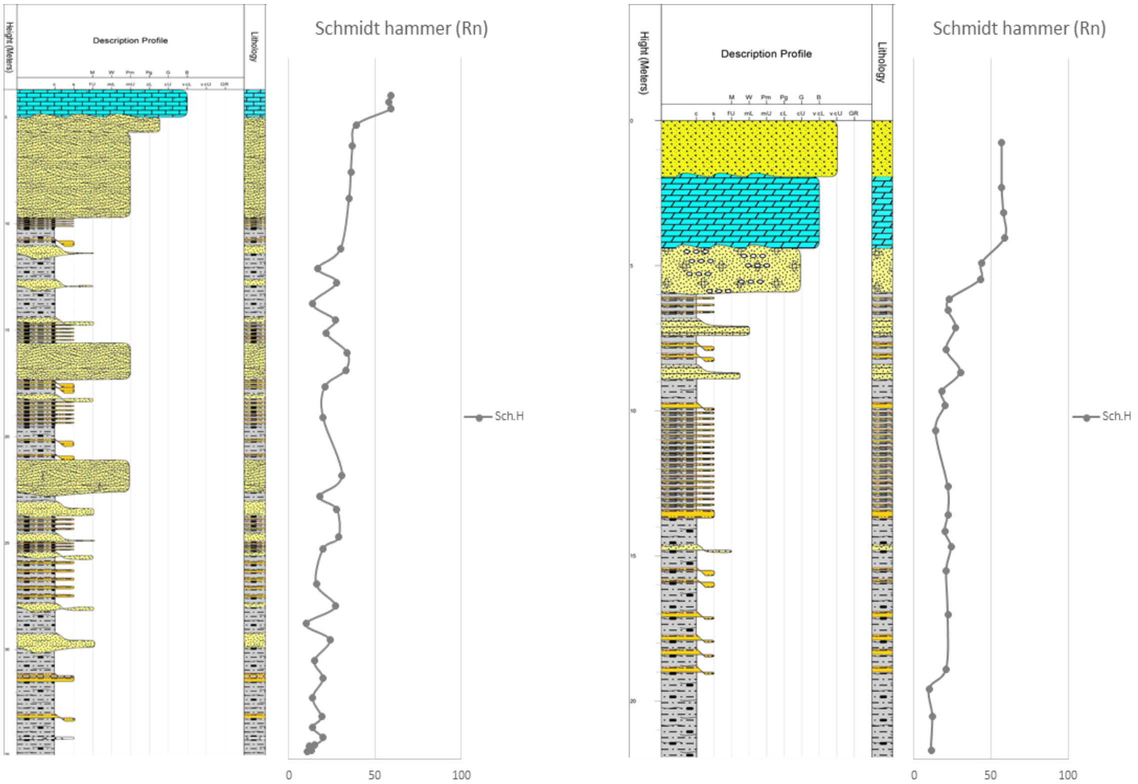

Figure 5-6 . Vertical lithostratigraphic sections -1 and -2 showing the various lithofacies, sedimentary structures, and Schmidt hammer Rebound number readings.

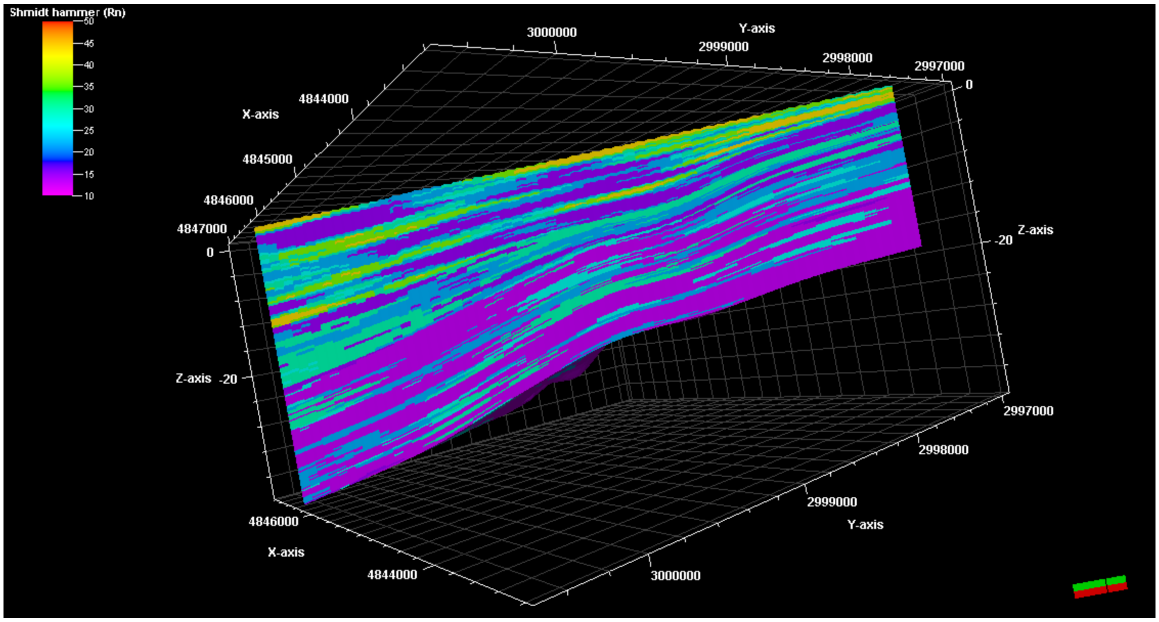

Figure 5-7 3D geostatistical model viewed from the North-West shows the distribution of the Schmidt hammer values in the study area. (Shmidt hammer readings were assigned as numeric values into the lithofacies model).

In addition to spectral gamma ray (SGR) and Schmidt hammer, that were measured in the field, many other measurements were taken in laboratory; P-wave velocity (Vp), Point load index (I), Uniaxial compressive strength (UCS), Poisson ratio (Vd), elastic young modulus (Es), and dynamic young modulus (Ed). The highest readings of P-wave velocity (Vp) occurred in the sandstone facies, especially in the upper parts of the vertical sections. Fissile shale and mudstone due to their low density have the lowest readings of velocity (Fig 5.8) and (Fig 5.9). Point load index (I) ranges from 0.2 to 1.2 in the fissile shale and mudstone lithofacies, from 1.2 to 1.6 in the siltstone lithofacies, and from 1.6 to 6.6 in the hummocky cross-stratified and trough cross-stratified sandstones (Fig 5.10) and (Fig 5.11). Uniaxial compressive strength (UCS) keeps the same trend of point load index (I), with the highest values in the sandstones lithofacies, and the lowest values in the shale and mudstone facies. Dynamic Poisson ratio values are decreasing towards the top of the vertical sections, with almost constant values for each lithofacies; Sandstones (0.257), Siltstone (0.293), Fissile shale and Mudstone (0.333) (Fig 5.12) and (Fig 5.13). These results suggest that fissile shale and Mudstone tend to have a ductile behavior, and Sandstone tend to have a brittle behavior as a response to deformation (Gereck, 2007). Dynamic Young modulus values are not like Dynamic Poisson ratio increasing towards the top of the vertical sections, revealing the highest values in the sandstone lithofacies (2.0 to 7.0), and the lowest values in the fissile shale and mudstone lithofacies (0.1 to 0.9) (Fig 5.14). The higher values of Dynamic young modulus in sandstone lithofacies propose Higher degree of stiffness than fissile shale and Mudstone (Baumgart, 2000). All measured properties are put together at the end to help to understand the geomechanical units against the lithological units, and to make it easier to divide the lithofacies of the vertical sections into geomechanical units (Fig 5.15), (Fig 5.16), (Fig 5.17), and (Fig 5.18).

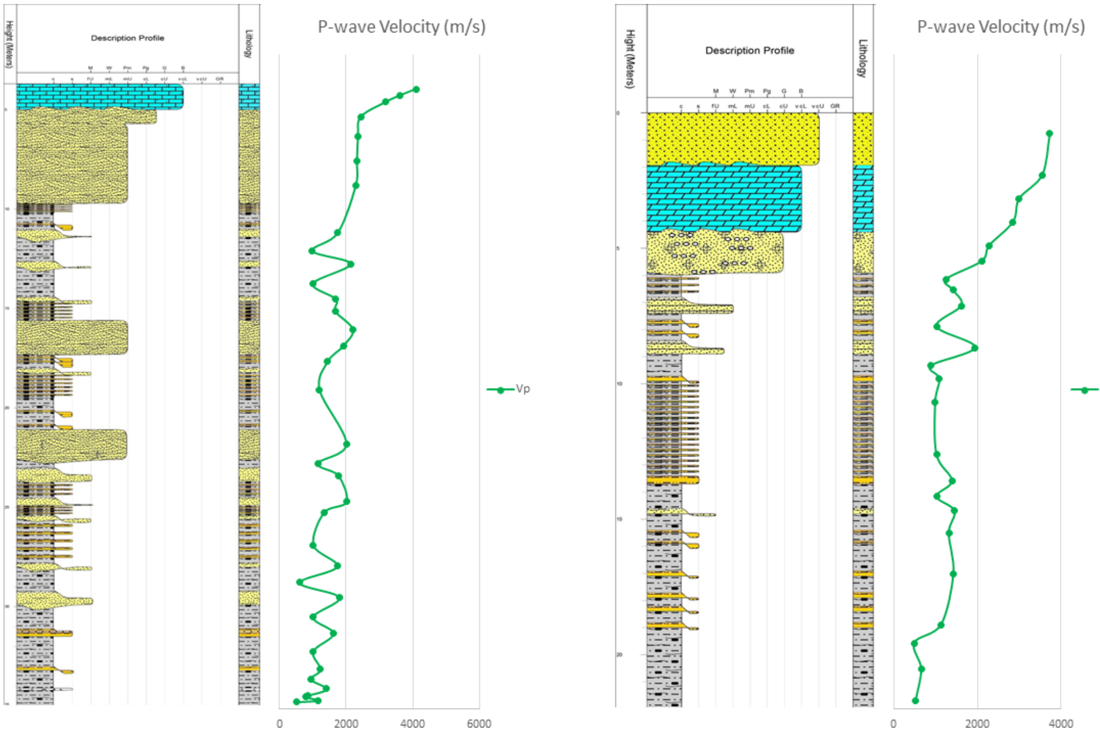

**Figure 5-8 Vertical lithostratigraphic sections -1 and -2 showing the various lithofacies, sedimentary structures, and P-wave velocity (m/s) readings.**

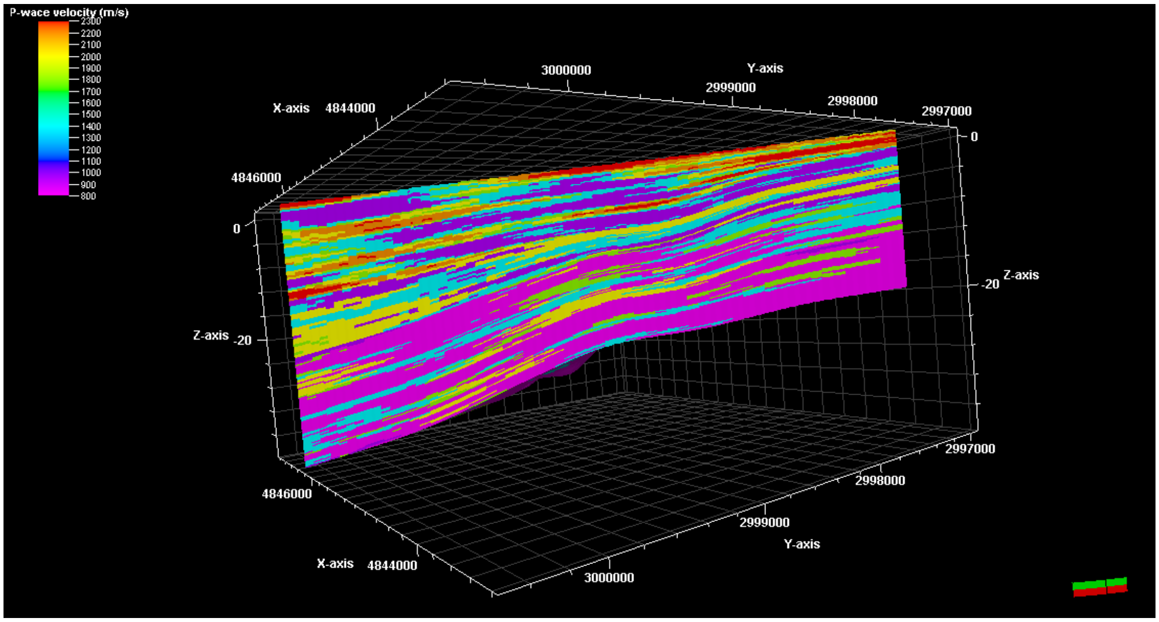

**Figure 5-9 3D geostatistical model viewed from the North-West shows the distribution of the P-wave velocity values in the study area. (P-Wave velocity readings were assigned as numeric values into the lithofacies model).**

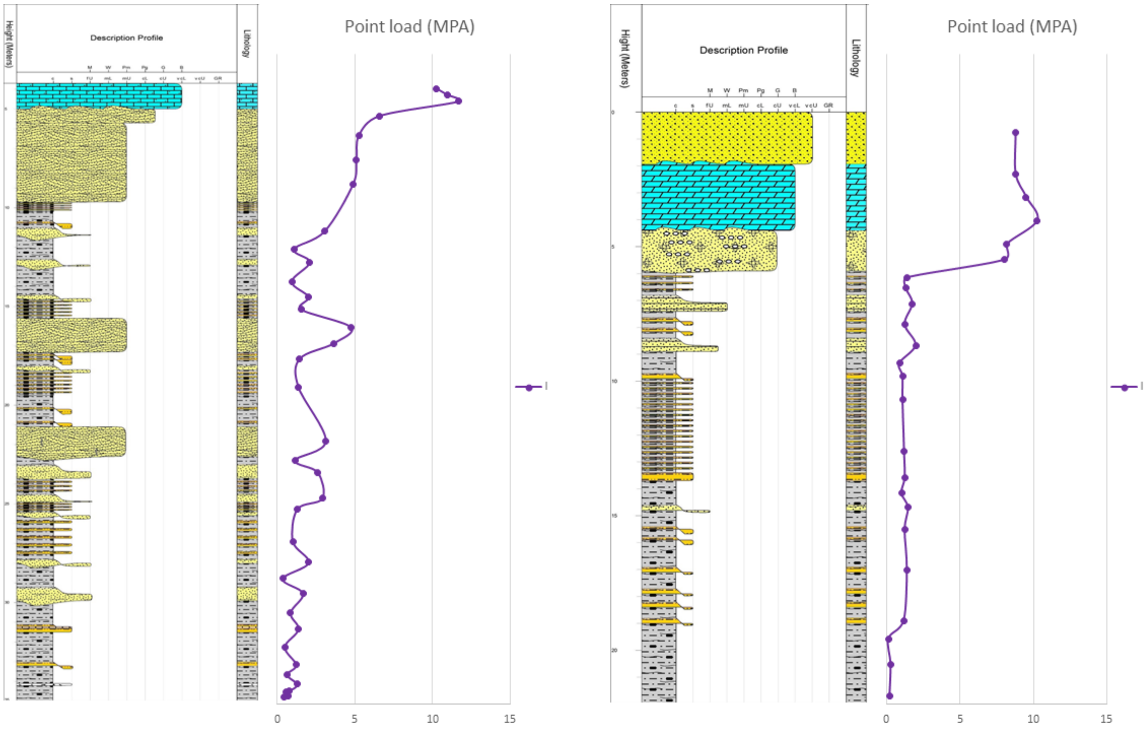

**Figure 5-10 5.10. Vertical lithostratigraphic sections -1 and -2 showing the various lithofacies, sedimentary structures, and Point load index (MPA) readings.**

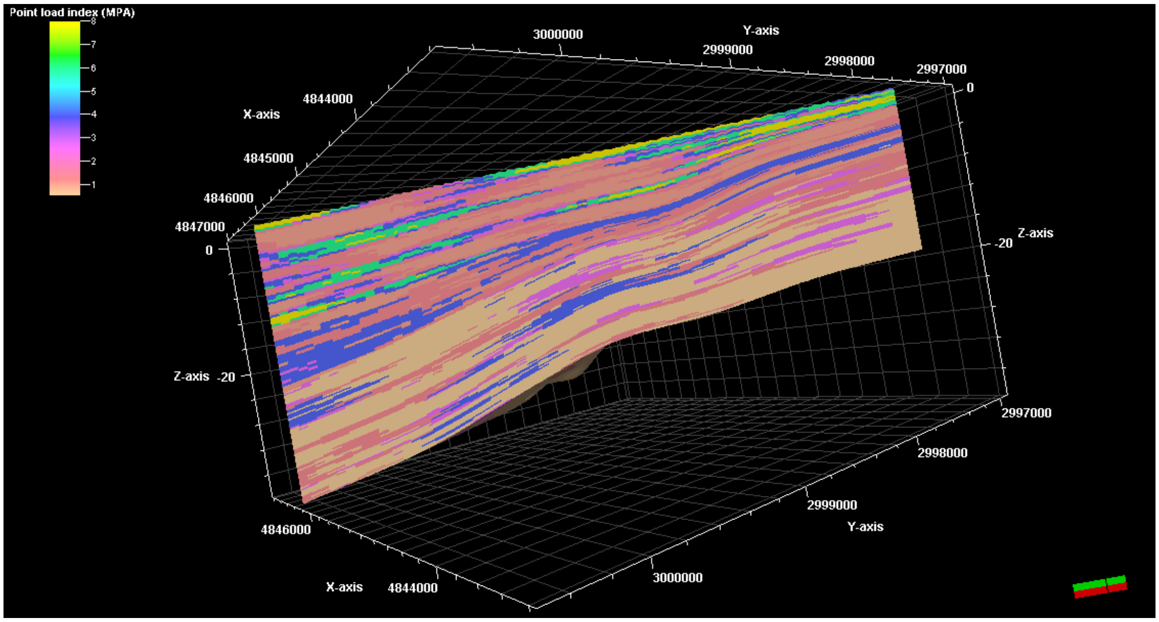

**Figure 5-11 3D geostatistical model viewed from the North-West shows the distribution of the Point load index values in the study area. (Point load readingsreadings were assigned as numeric values into the lithofacies model).**

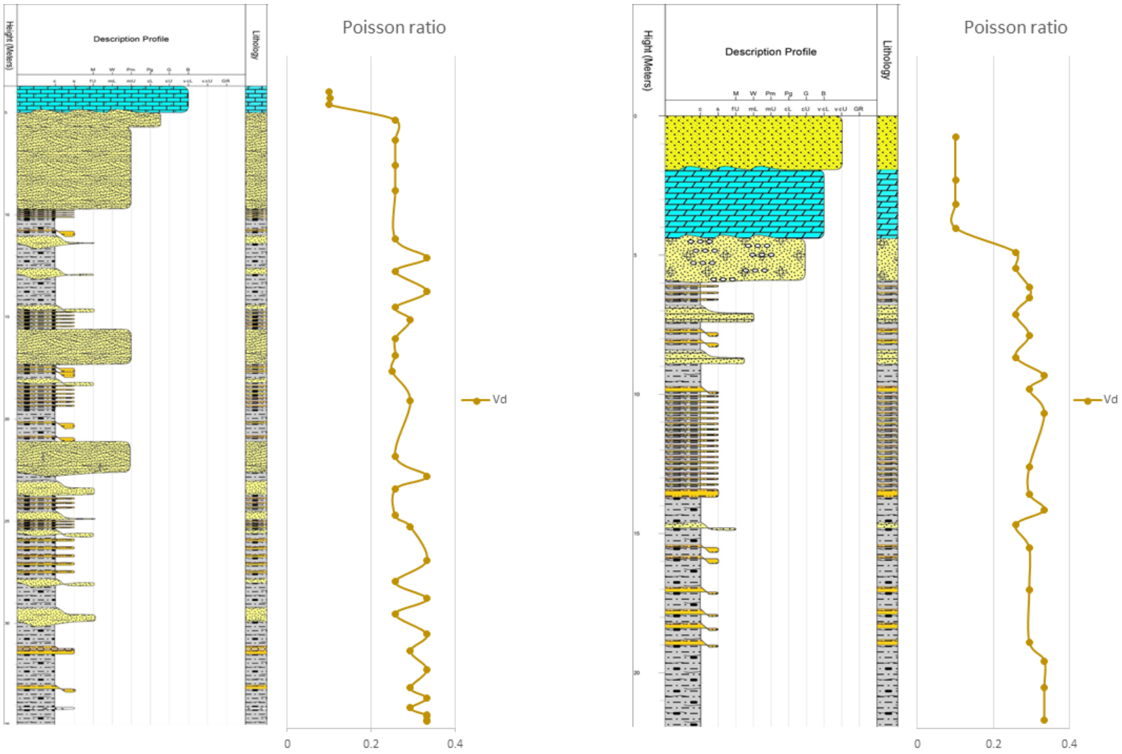

Figure 5-12 Vertical lithostratigraphic sections -1 and -2 showing the various lithofacies, sedimentary structures, and Dynamic Poisson ratio values.

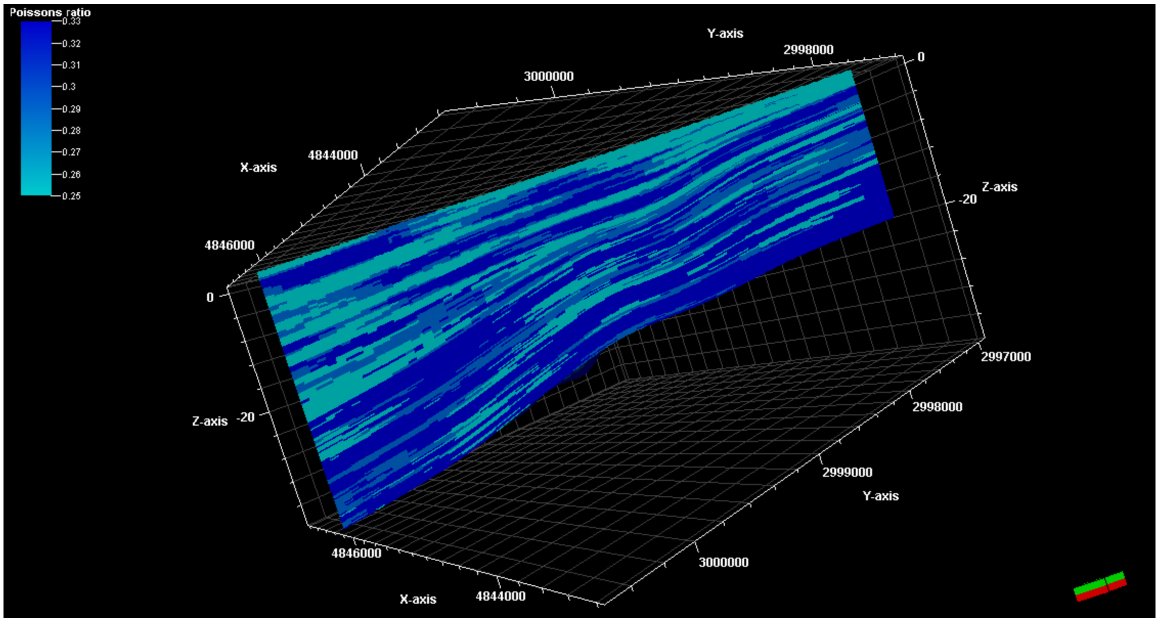

Figure 5-13 3D geostatistical model viewed from the North-West shows the distribution of the dynamic Poisson ratio values in the study area. (Poisson ratio were assigned as numeric values into the lithofacies model).

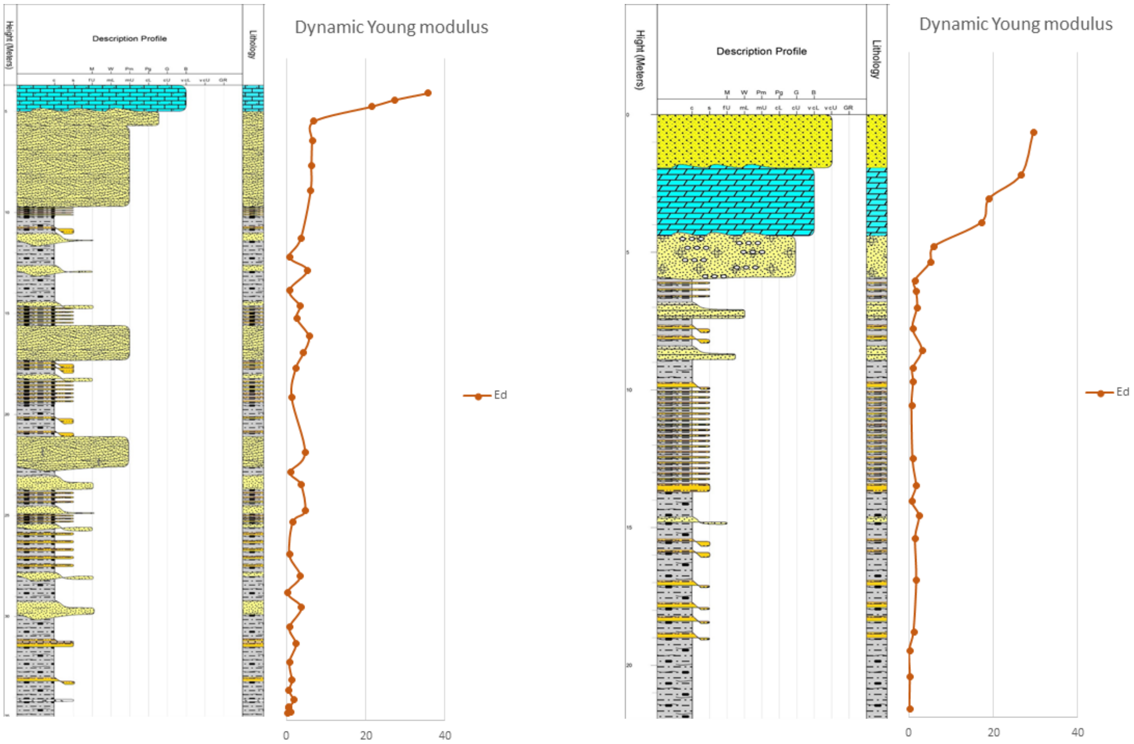

Figure 5-14 Vertical lithostratigraphic sections -1 and -2 showing the various lithofacies, sedimentary structures, and Dynamic Young modulus values.

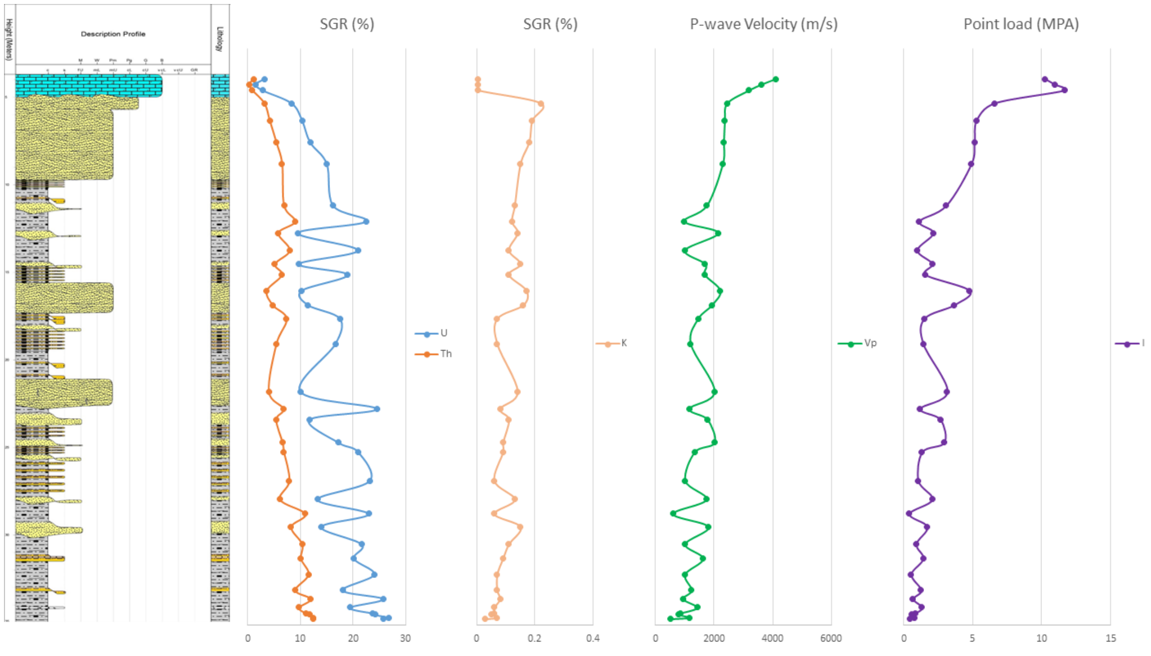

Figure 5-15 Vertical lithostratigraphic section-1 showing the various lithofacies, sedimentary structures, Spectral gamma ray (SGR) readings, P-wave velocity (m/s) readings, and Point load index (MPA) readings.

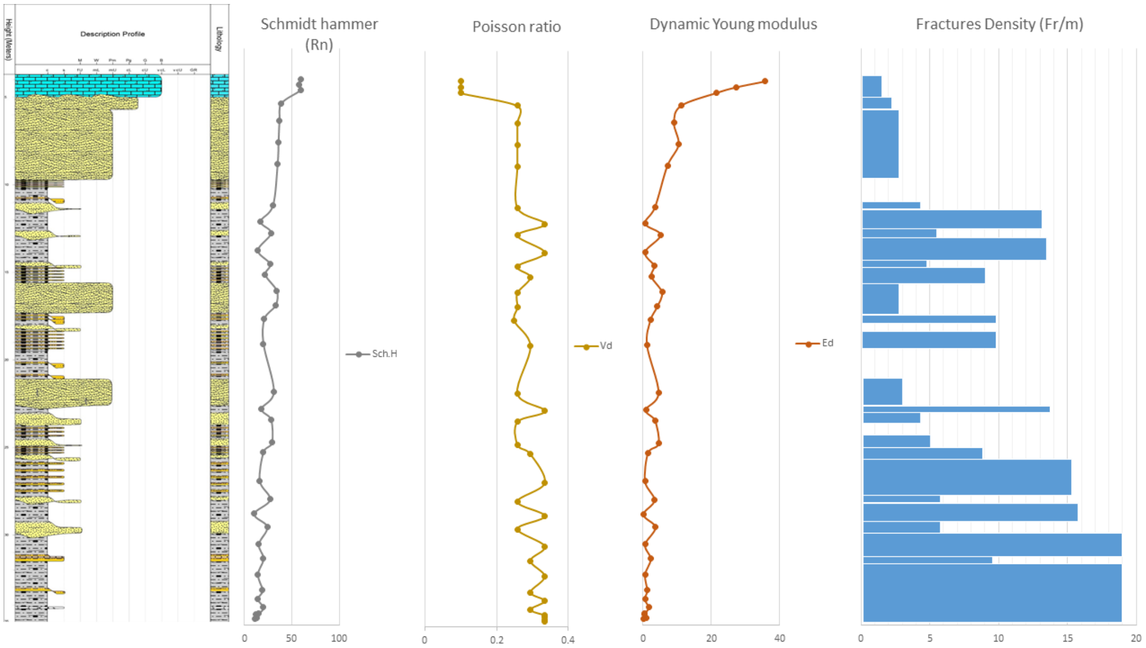

Figure 5-16 Vertical lithostratigraphic section-1 showing the various lithofacies, sedimentary structures, Schmidt hammer (Rn) readings, Dynamic Poisson ratio values, Dynamic Young modulus values, and Fractures density (Fr/m).

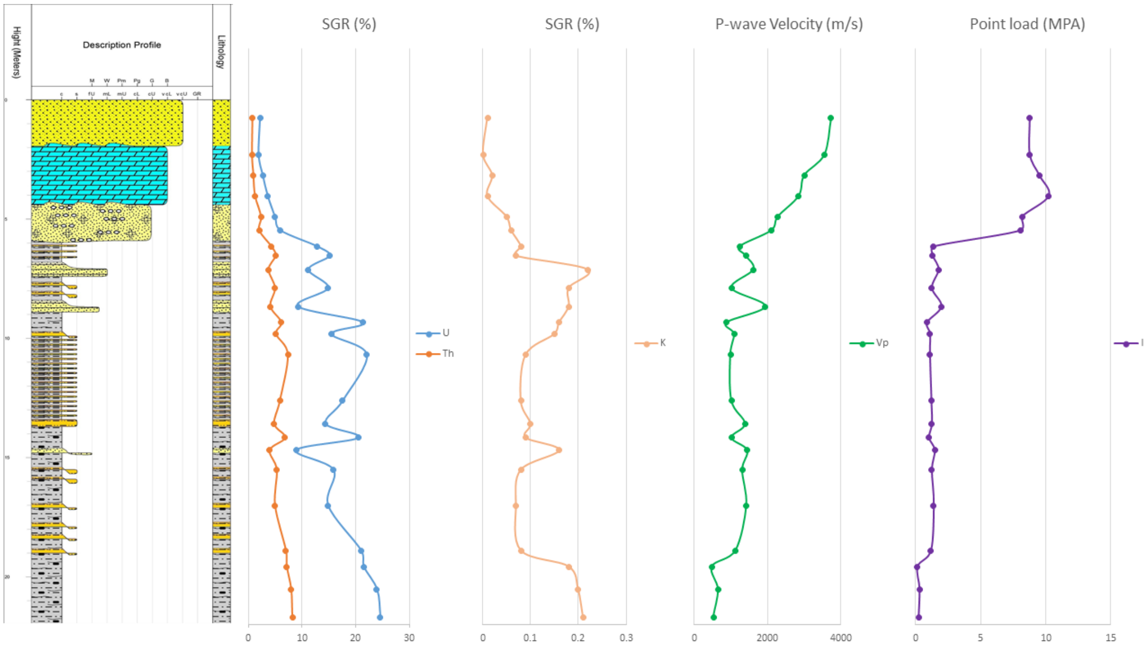

Figure 5-17 Vertical lithostratigraphic section -2 showing the various lithofacies, sedimentary structures, Spectral gamma ray (SGR) readings, P-wave velocity (m/s) readings, and Point load index (MPA) readings.

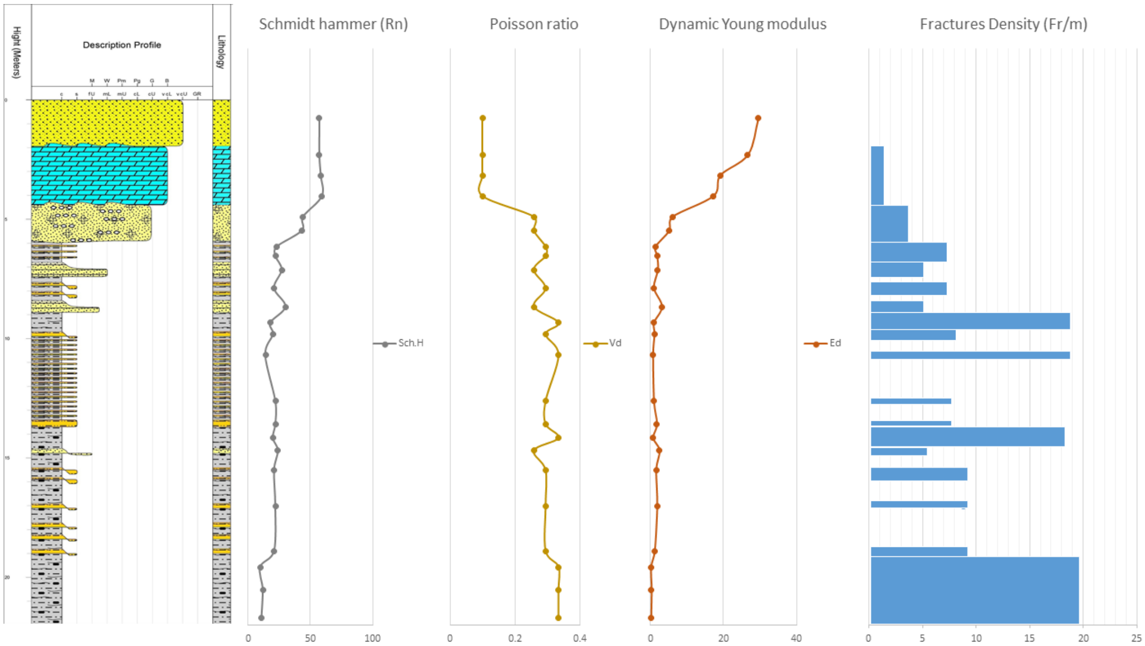

**Figure 5-18 Vertical lithostratigraphic section-1 showing the various lithofacies, sedimentary structures, Schmidt hammer (Rn) readings, Dynamic Poisson ratio values, Dynamic Young modulus values, and Fractures density (Fr/m).**

## 5.3 Petrophysical and geomechanical relationships

Porosity is defined as the proportion between voids volume and the total volume of a rock (Duncan, 1969), and it's considered as one of the most important factors affecting the petrophysical properties. Larger voids volume means higher porosity percentage, and that leads to lower strength. Porosity is dependent on grain size, compaction, and density (Glover, 2011). Literature and work done in this study reveals a strong relationship between porosity and geomechanical properties expressed in cross plots showing the regression coefficient ($R^2$). In general, the relationships between porosity and other geomechanical properties are inverse, except for the Dynamic Poisson ratio, that defines the ductility of the rocks. (Fig 5.19) and (Fig 5.20) shows the relationship between porosity and point load index for the samples taken from vertical section-1 and vertical section-2 respectively. The inverse relationship says that the strength of the rocks decreases as the porosity increases. Fissile shale and mudstone lithofacies are two different lithological units, but they behave almost the same when it comes to petrophysical and geomechanical properties. Anyway, these figures and other geomechanical and petrophysical relationship figures show mainly the different lithological units of Qusaiba shale member behavior when geomechanical and petrophysical properties are applied. (Fig 5.21) and (Fig 5.22) shows the relationship between porosity and Uniaxial compressive strength for the samples taken from vertical section-1 and vertical section-2. It shows the same inverse relationships of porosity and point load index, for more confirmation that the strength decreases when pores volume increases. Schmidt hammer values were also plotted against porosity (Fig 5.23) and (Fig 5.24) for samples taken for vertical section-1 and vertical section-2. The inverse relationships for different lithological units suggest that the decrease in surface hardness and penetration resistance is a result of pores volume increase.

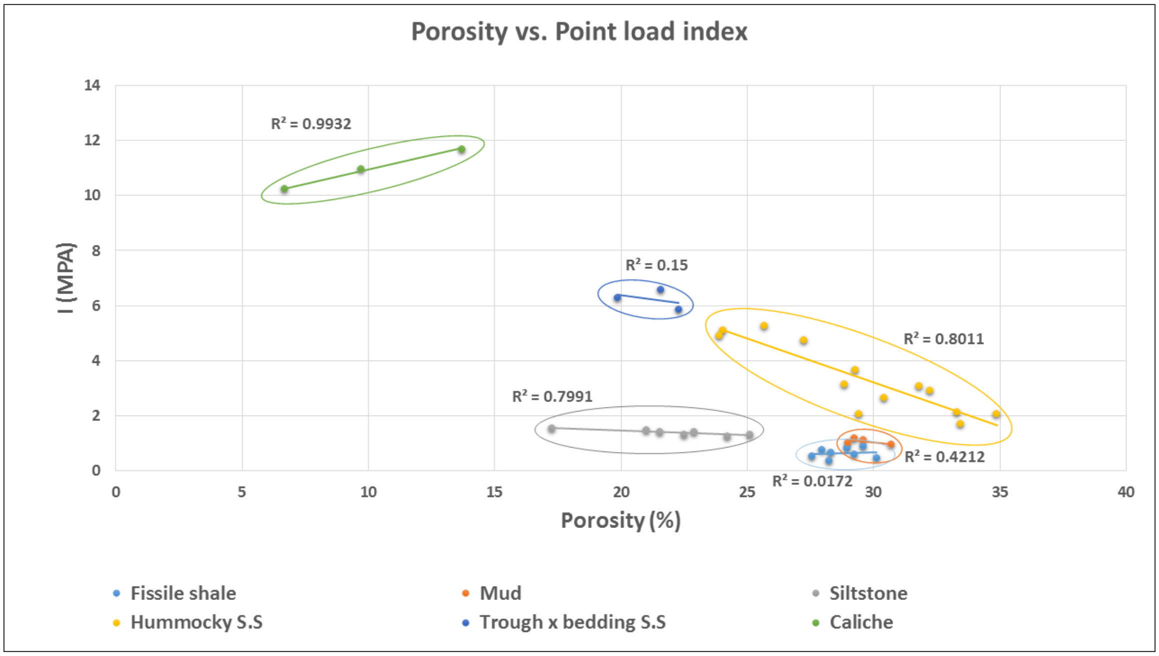

Figure 5-19 Cross plot of porosity and point load index for different lithological units in vertical section-1.

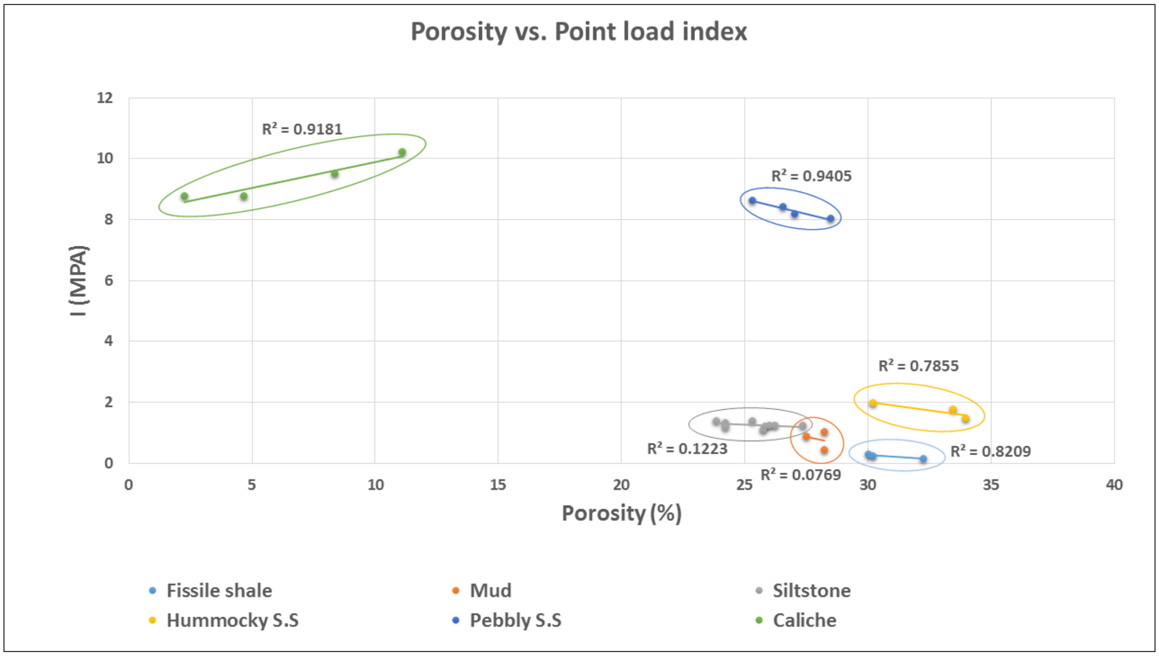

Figure 5-20 Cross plot of porosity and point load index for different lithological units in vertical section-2.

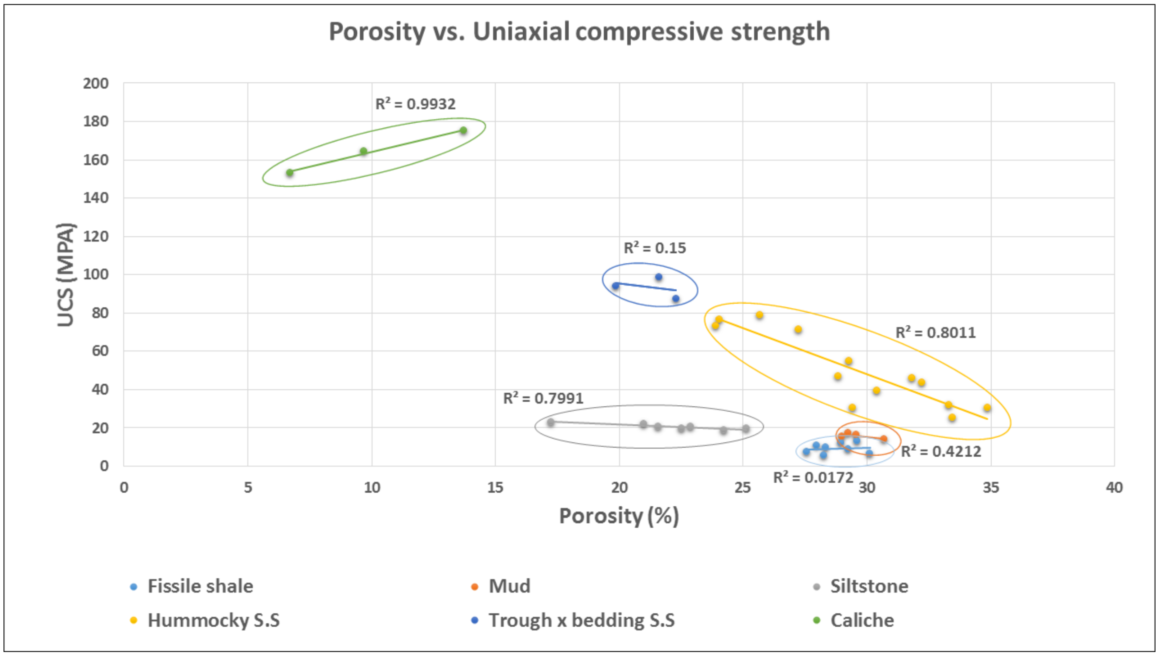

Figure 5-21 Cross plot of porosity and Uniaxial compressive strength for different lithological units in vertical section-1.

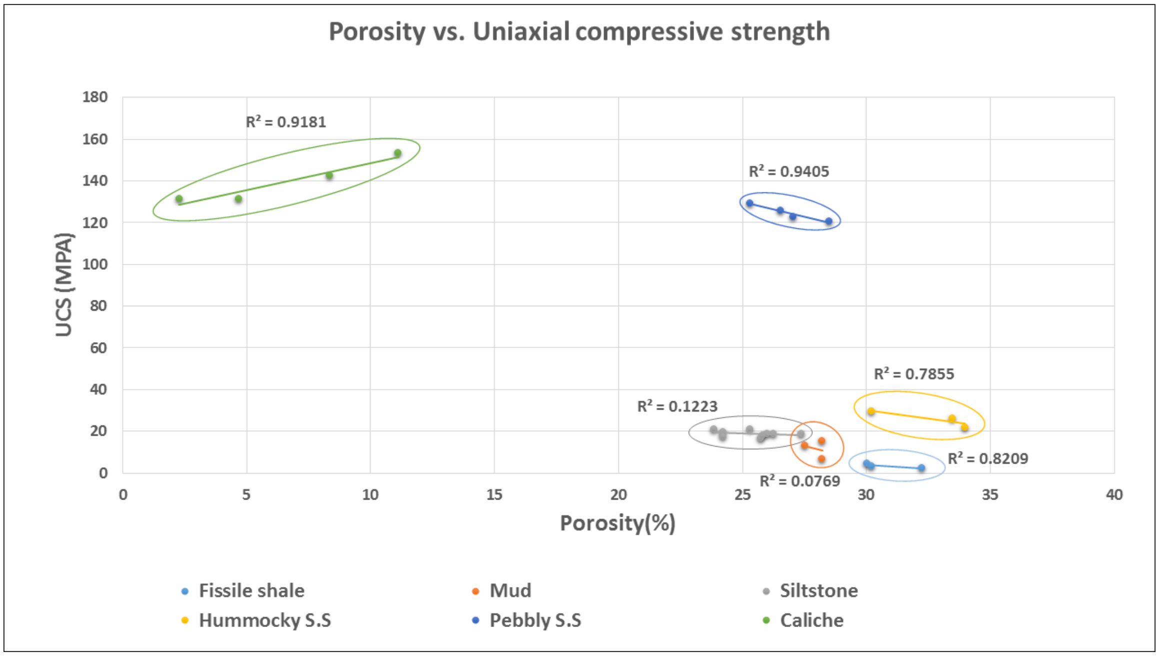

Figure 5-22 Cross plot of porosity and Uniaxial compressive strength for different lithological units in vertical section-2.

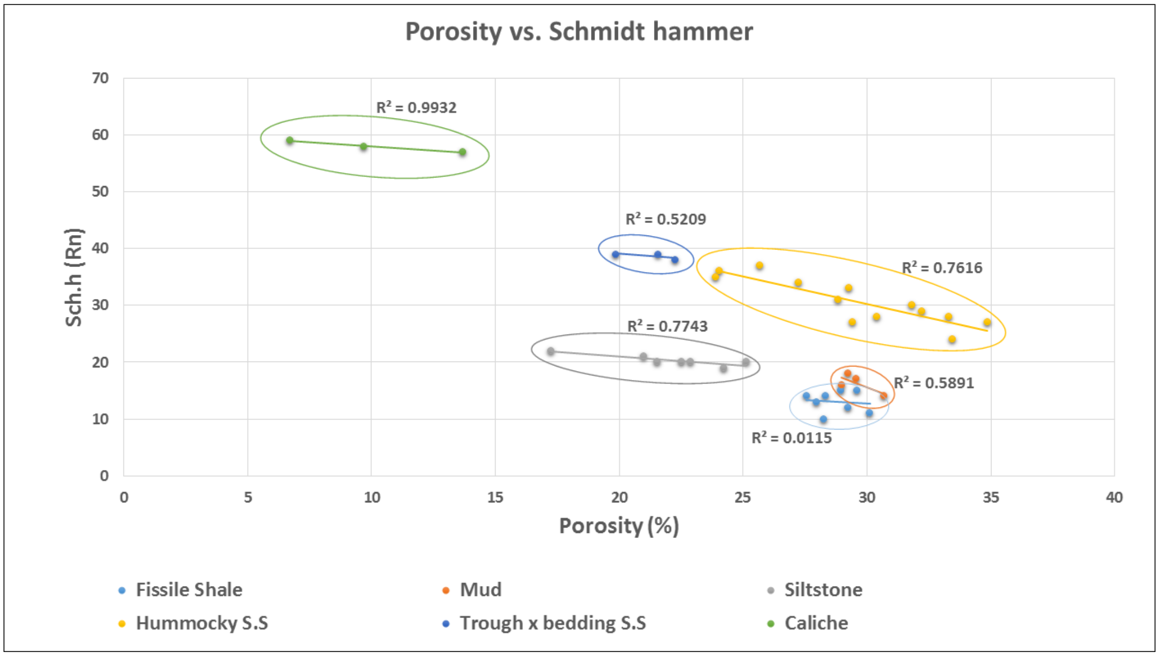

**Figure 5-23 Cross plot of porosity and Schmidt hammer for different lithological units in vertical section-1.**

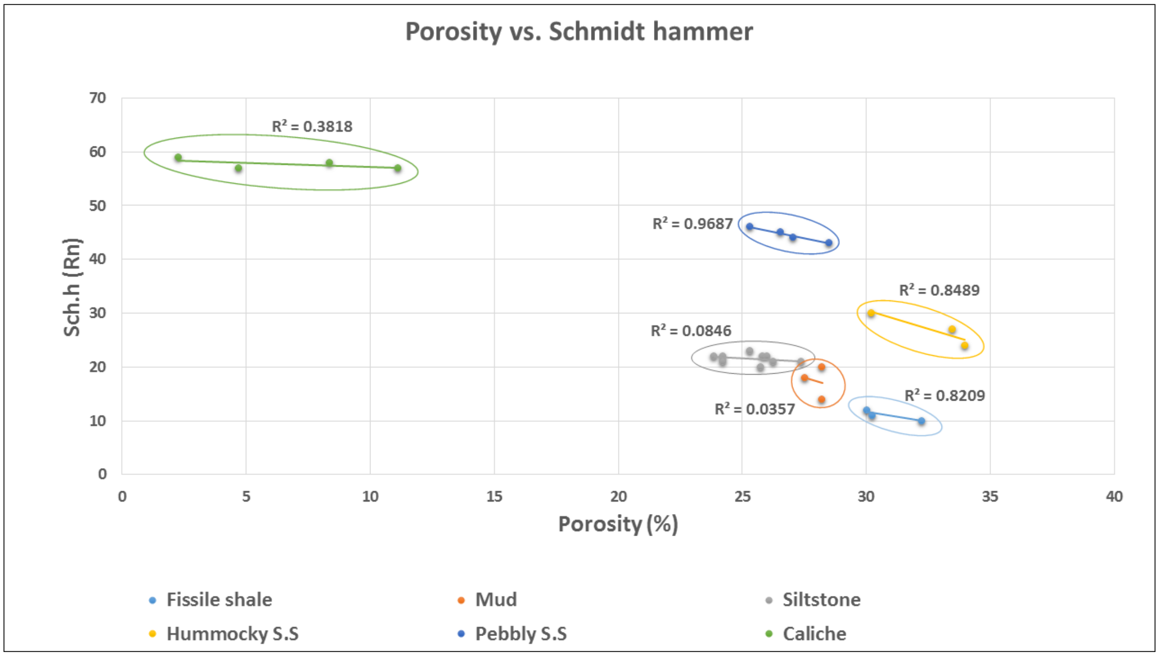

**Figure 5-24 Cross plot of porosity and Schmidt hammer for different lithological units in vertical section-2.**

(Fig 5.25) and (Fig 5.26) show the inverse relationship between P-wave velocity and porosity for samples taken from vertical section-1 and vertical section-2. P-wave velocity is an important indicator for geomechanical properties and a reflector to the compaction of the body (Milsom, 2003). These figures reflect that the decrease in compaction degree and density is linked to the increase in pores volume.

(Fig 5.27) and (Fig 5.28) shows another inverse relationship, between Dynamic young modulus and porosity. Since Dynamic young modulus is an indicator for rocks stiffness, this relationship suggests that the increase of pore volumes is a cause for the decrease in stiffness.

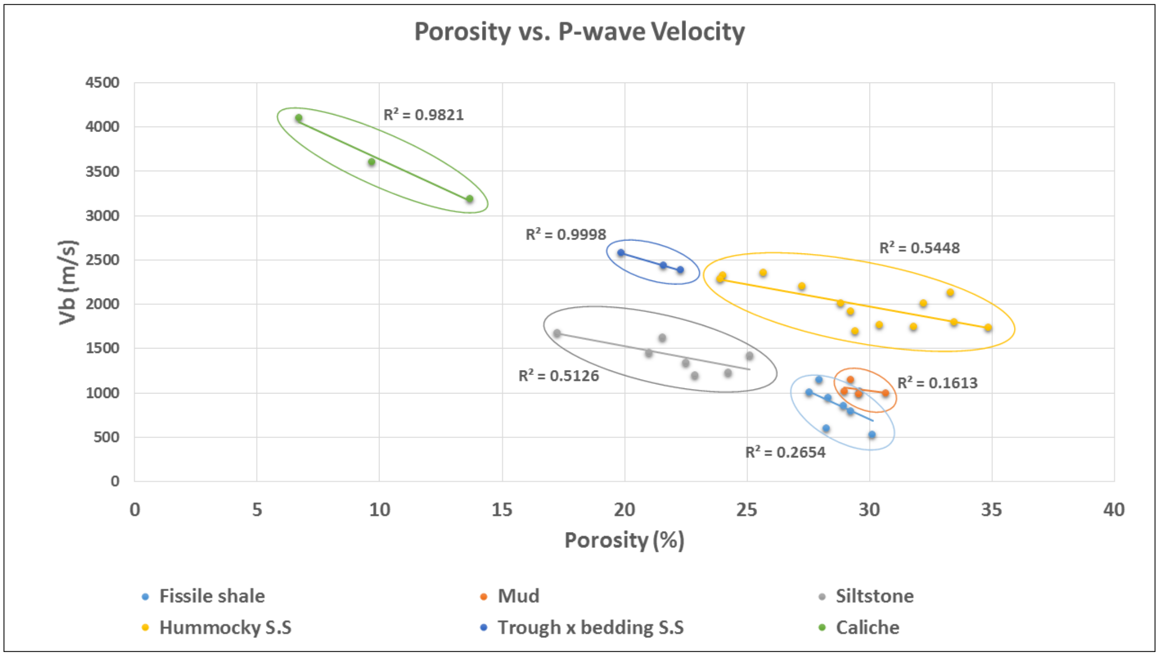

Figure 5-25 Cross plot of porosity and P-wave velocity for different lithological units in vertical section-1.

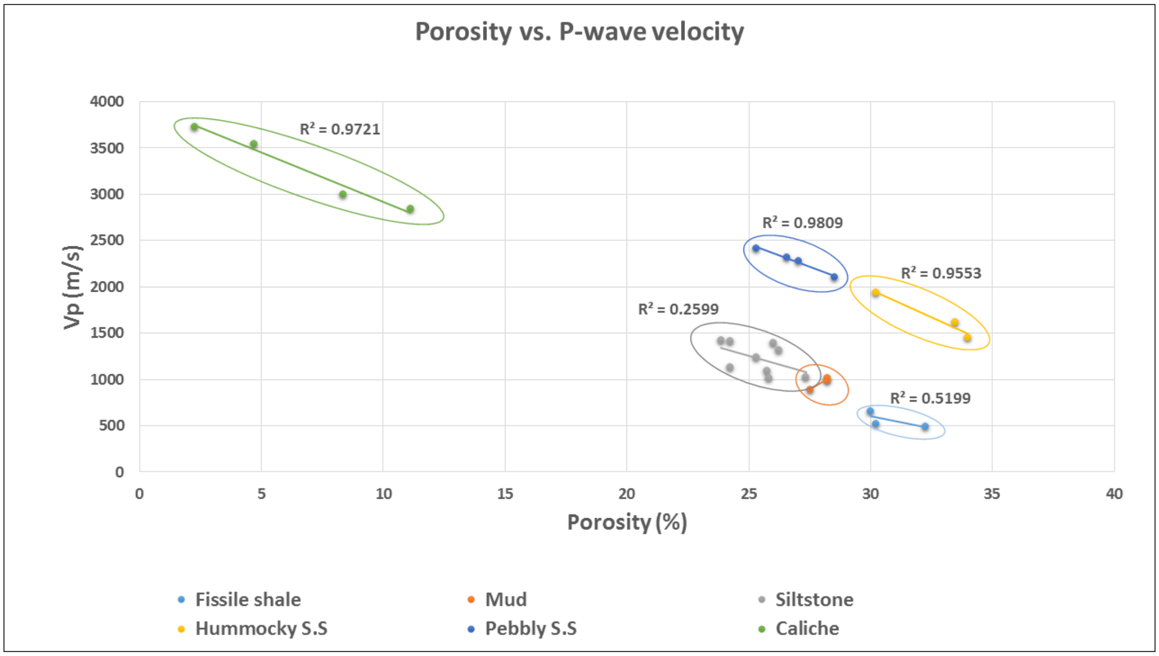

Figure 5-26 Cross plot of porosity and P-wave velocity for different lithological units in vertical section-2.

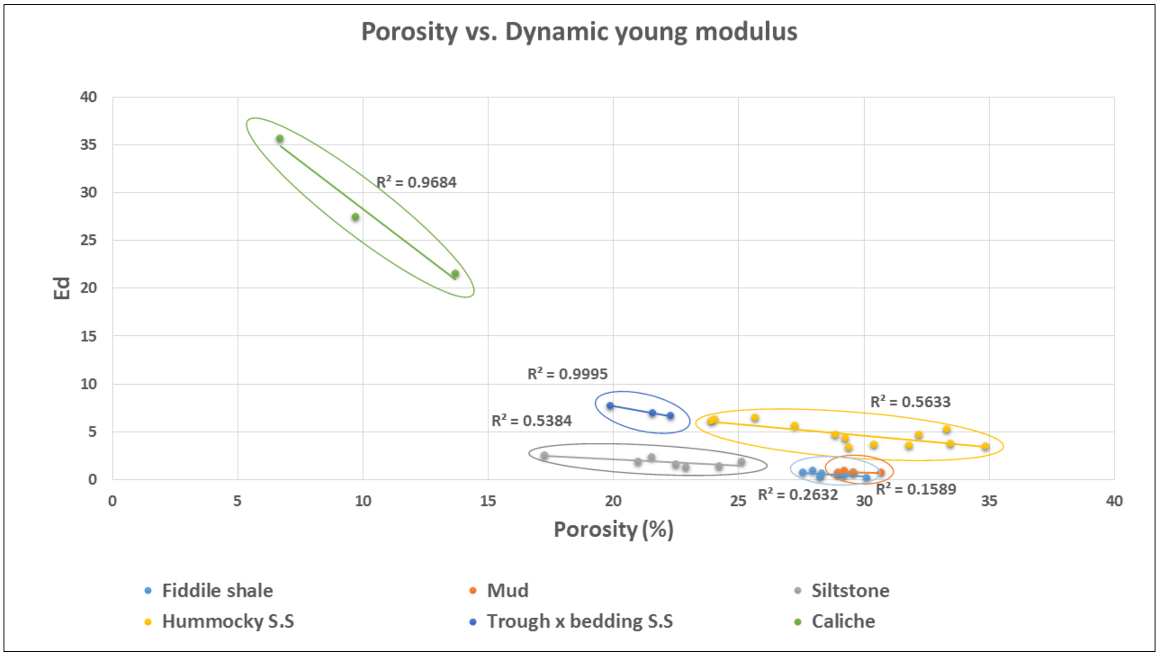

Figure 5-27 . Cross plot of porosity and Dynamic young modulus for different lithological units in vertical section-1.

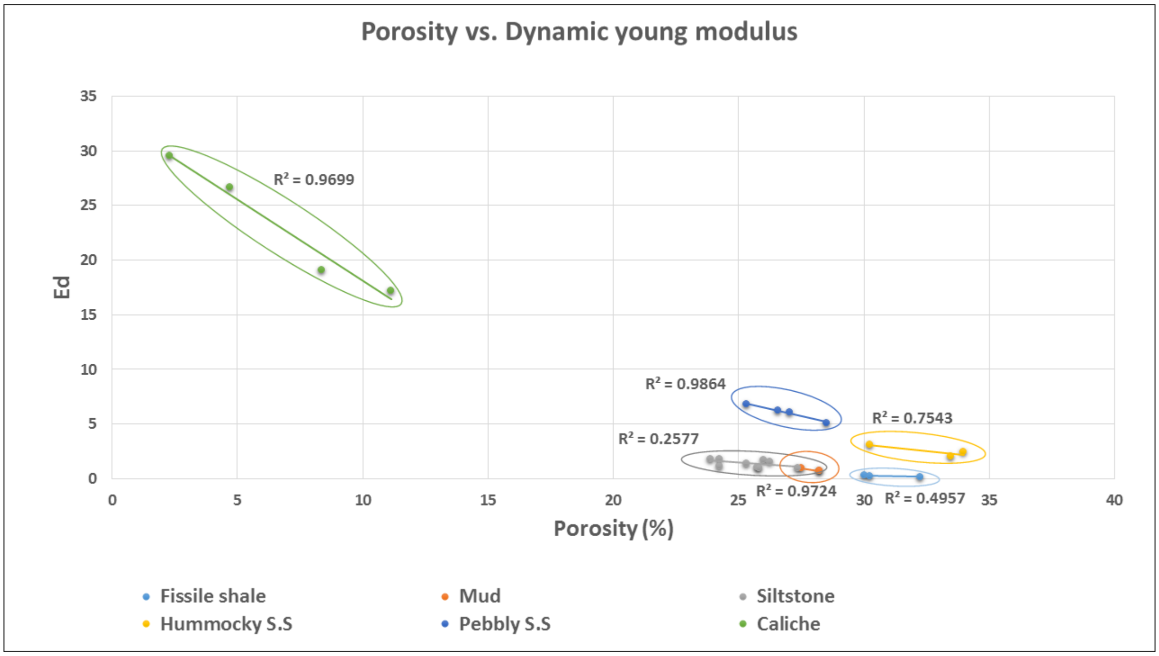

Figure 5-28 Cross plot of porosity and Dynamic young modulus for different lithological units in vertical section-2.

P-wave velocity is inversely proportional to the porosity but directly proportional to most of the geomechanical properties. (Fig 5.29) and (Fig 5.30) show the relationship between P-wave velocity and point load index for the samples taken from vertical section-1 and vertical section-2. The direct proportion relationships of all lithofacies propose that the compaction degree and density of these rocks increase with the increase in strength.

(Fig 5.31) and (Fig 5.32) show the same direct proportion relationships of the different lithofacies between P-wave velocity and Schmidt hammer. These figures reflect that compaction degree and density are directly proportion to penetration resistance and surface hardness.

The relationships between geomechanical properties are mostly directly proportional. The relationship between point load index and Schmidt hammer shows that the increase in the strength of a rock is proportional to the increase in penetration resistance and surface hardness (Fig 5.33) and (Fig 5.34). The relationship between Uniaxial compressive strength and Dynamic young modulus shown in (Fig 5.35) and (Fig 5.36) is directly proportional for all lithofacies in Qusaiba shale member. These relationships reflect the proportion between strength and stiffness in these rocks.

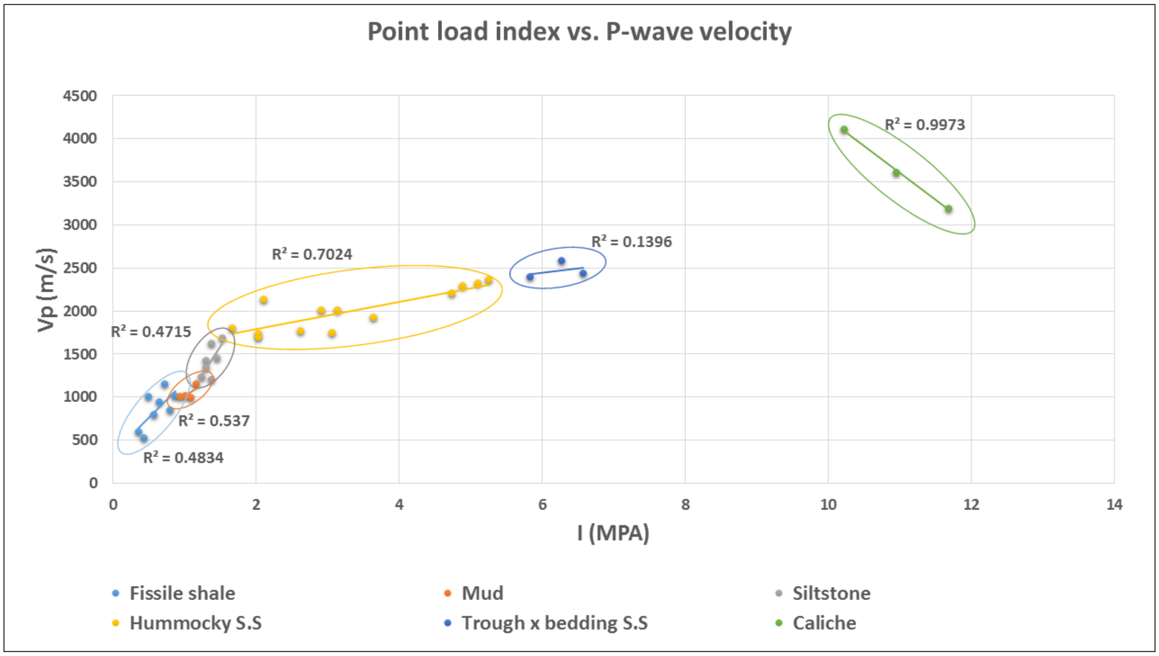

Figure 5-29 Cross plot of Point load and P-wave velocity for different lithological units in vertical section-1.

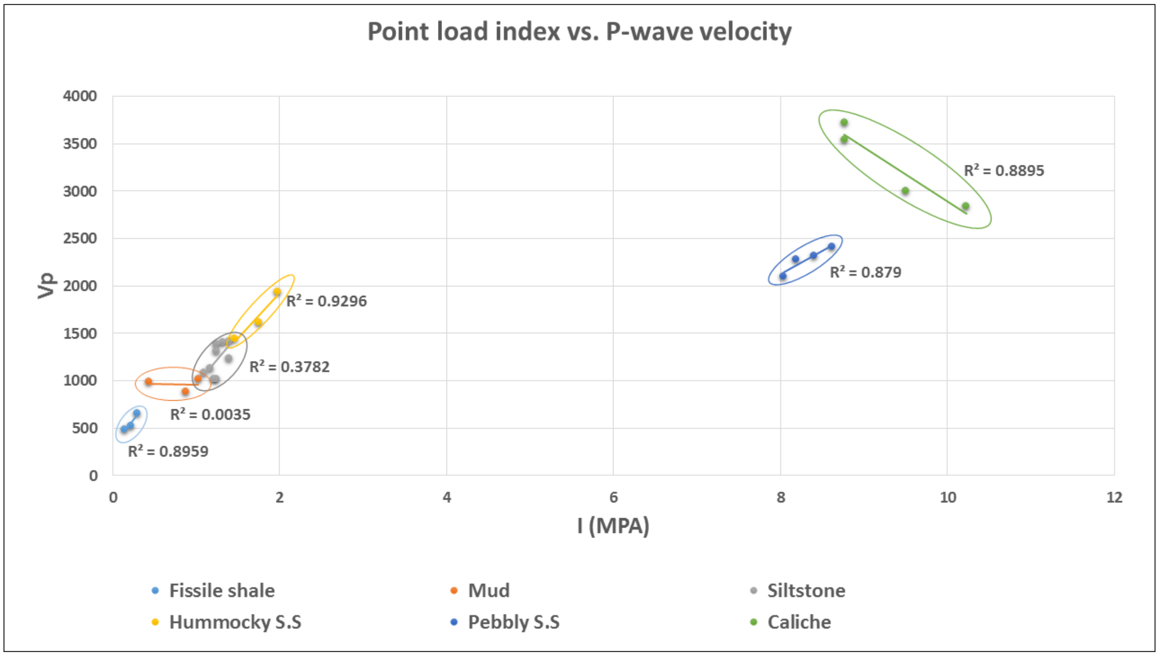

Figure 5-30 Cross plot of Point load and P-wave velocity for different lithological units in vertical section-2.

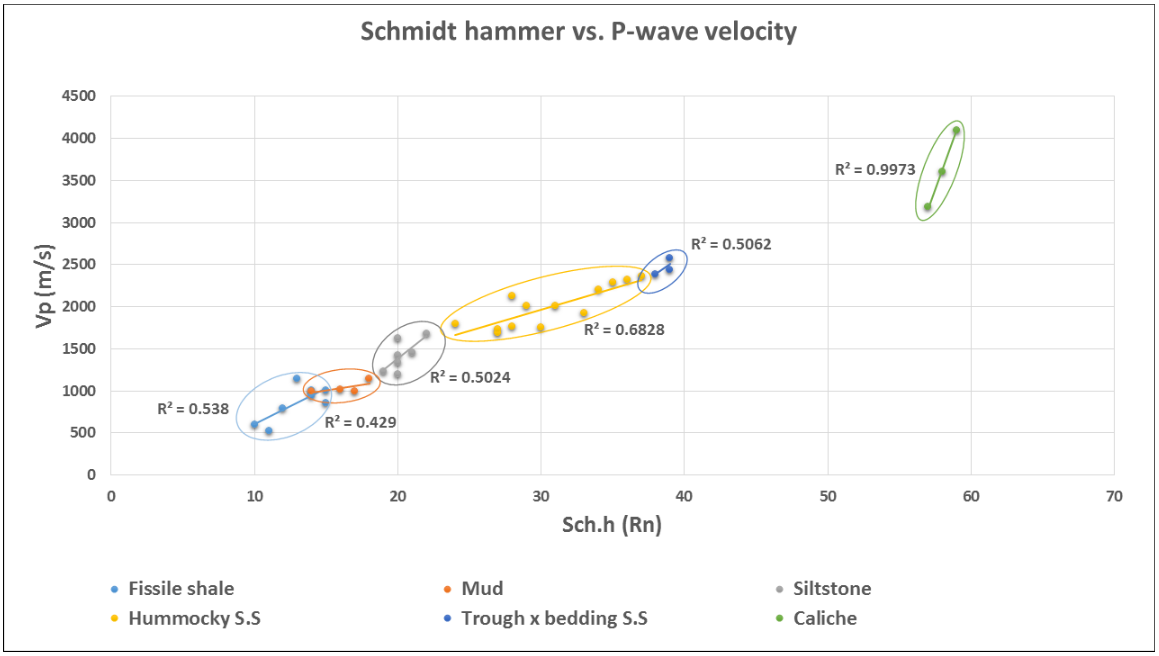

Figure 5-31 Cross plot of Schmidt hammer and P-wave velocity for different lithological units in vertical section-1.

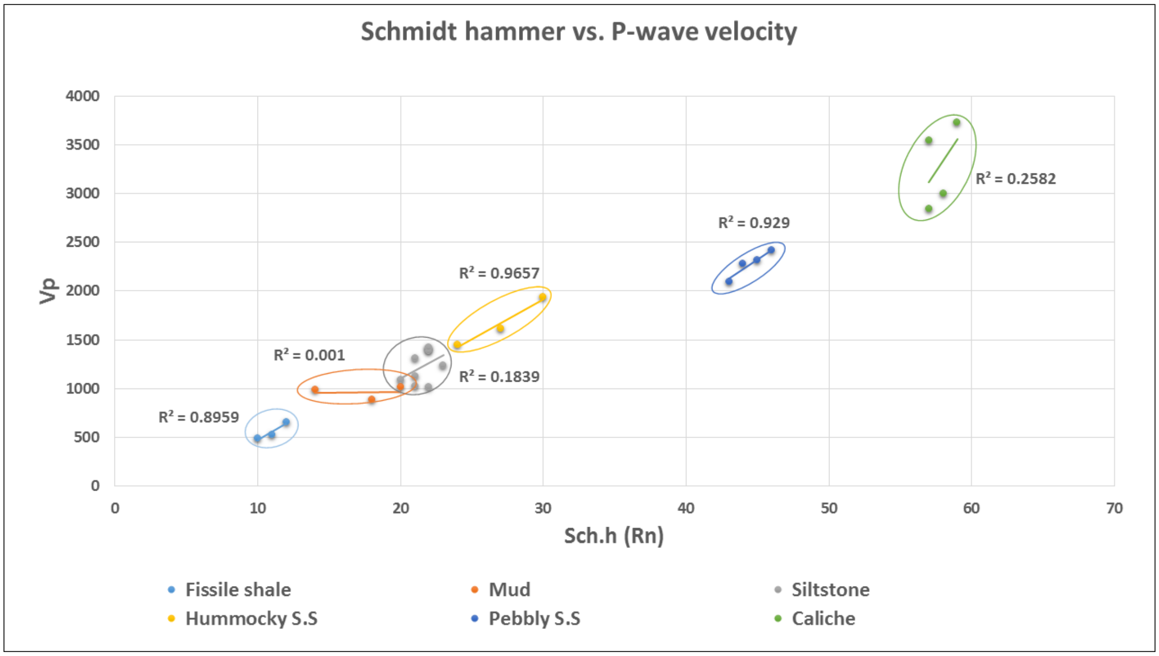

Figure 5-32 Cross plot of Schmidt hammer and P-wave velocity for different lithological units in vertical section-2.

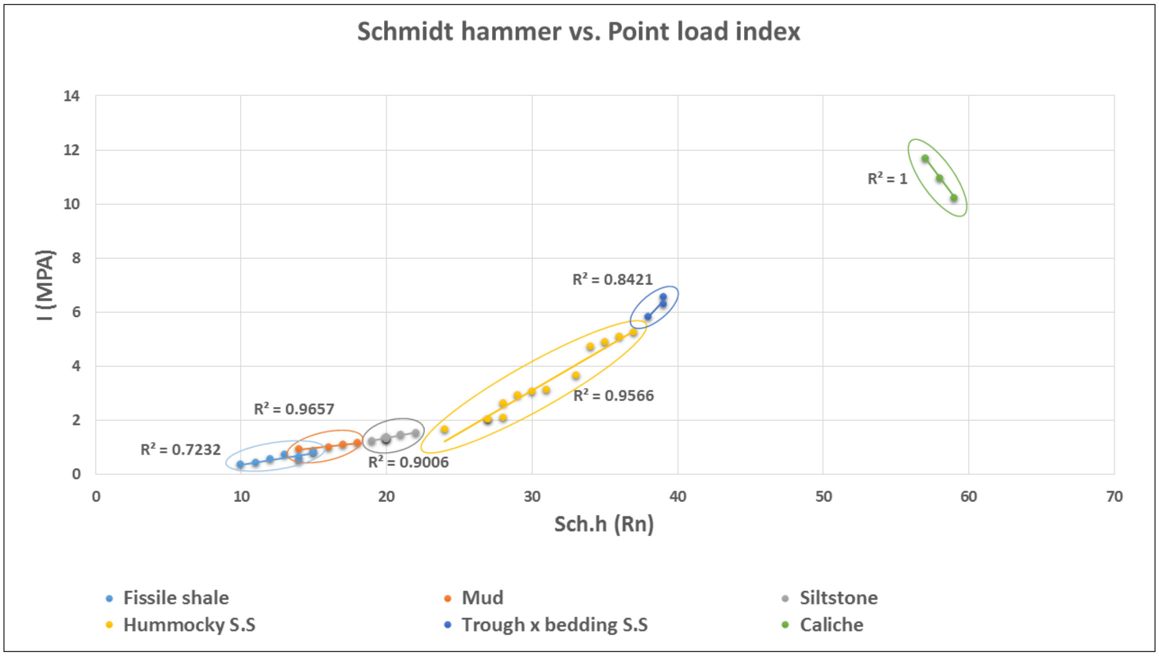

Figure 5-33 Cross plot of Schmidt hammer and Point load index for different lithological units in vertical section-1.

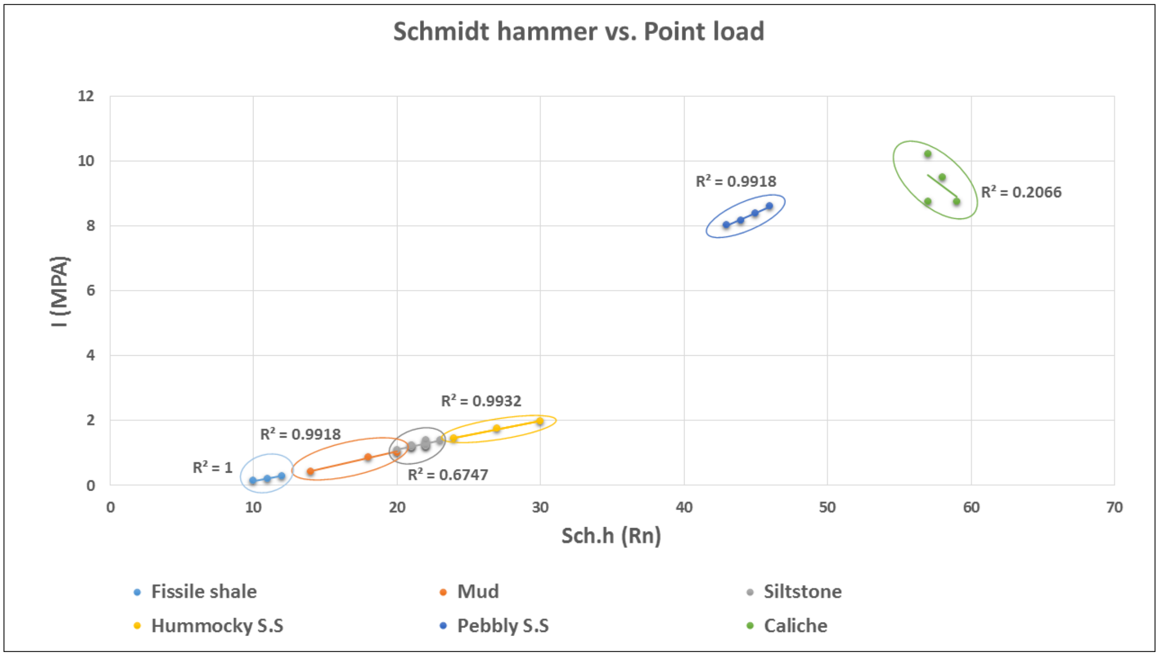

Figure 5-34 Cross plot of Schmidt hammer and Point load index for different lithological units in vertical section-2.

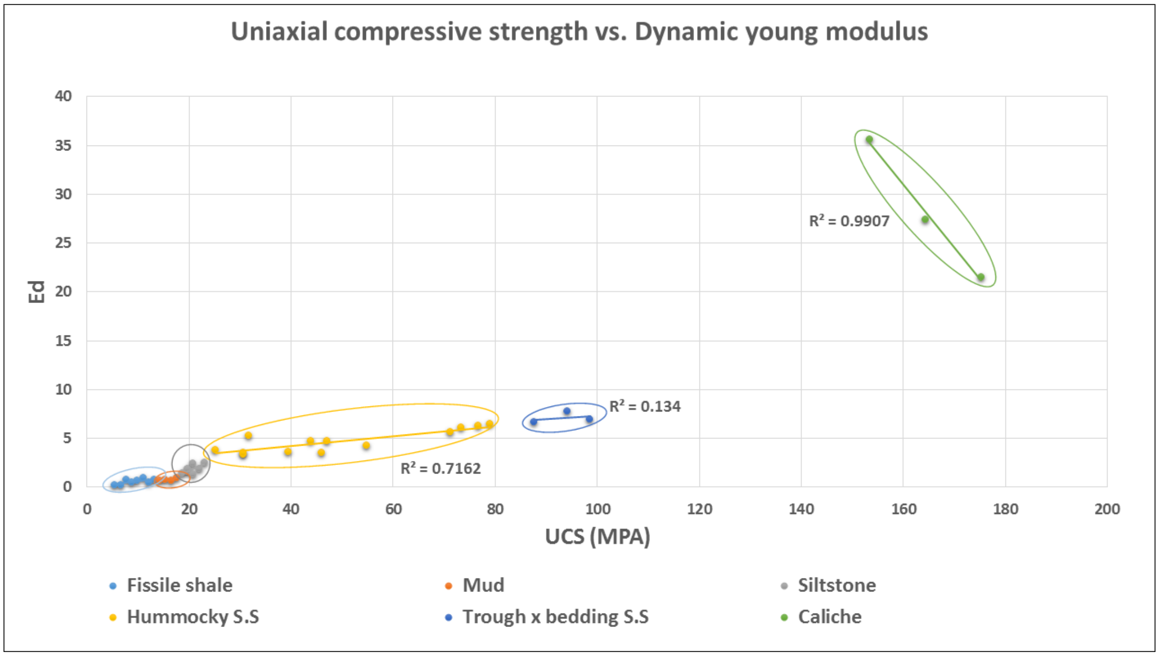

Figure 5-35 Cross plot of Uniaxial compressive strength and Dynamic young modulus for different lithological units in vertical section-1.

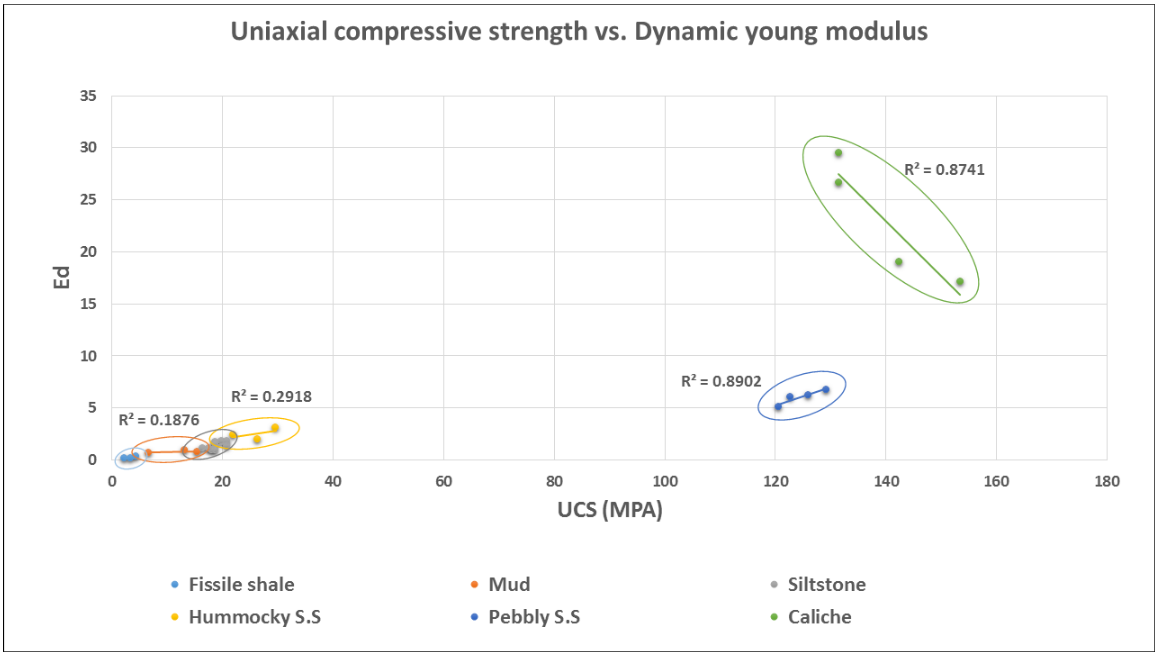

Figure 5-36 Cross plot of Uniaxial compressive strength and Dynamic young modulus for different lithological units in vertical section-2.

## 5.4 Classification and determination of geomechanical units

The lithological units have been classified using Point load index values (Bieniawski, 1975) (Table 5.1), and Uniaxial compressive strength values (Lucas, 2000) (Table 5.2).

According to the previous classifications the lithological units in the area have been classified as shown in (Table 5.3) and (Table 5.4), and according to the geomechanical properties, geomechanical petrophysical relationships, and fractures information, five geomechanical units have been determined as shown in (Fig 5.37) and (Fig 5.38).

**Table 5-1 Classification of strength based on point load index (Bieniawski, 1975).**

| Classification | Point load index (I) (MPA) |
|---|---|
| Very high strength | > 8 |
| High strength | 4 - 8 |
| Medium strength | 2 - 4 |
| Low strength | 1 - 2 |
| Very low strength | < 1 |

**Table 5-2 Classification of strength based on Uniaxial compressive strength (Lucas, 2000).**

| Classification | Uniaxial compressive strength (MPA) |
|---|---|
| Very high | > 200 |
| High | 100 - 200 |
| Medium | 50 - 100 |
| Low | 25 - 50 |
| Very low | 10 - 25 |
| Extremely low | < 10 |

Table 5-3 Lithological units’ classification based on Uniaxial compressive strength values.

| Lithological unit | Average I (MPA) | (Bieniawski, 1975) |
|---|---|---|
| Pebbly SS | 8.3085 | Very high strength |
| Trough x-stratified SS | 6.2329 | High strength |
| Hummock x-stratified SS | 2.923 | Medium strength |
| Micaceous siltstone | 1.3732 | Low strength |
| Mudstone | 1.0305 | Low strength |
| Fissile shale | 0.6182 | Very low strength |

Table 5-4 . Lithological units’ classification based on Point load index values.

| Lithological unit | Average UCS (MPA) | (Lucas, 2000) |
|---|---|---|
| Pebbly SS | 124.63 | High |
| Trough x-stratified SS | 93.53 | Medium |
| Hummocky x-stratified SS | 43.61 | Low |
| Micaceous siltstone | 20.21 | Very low |
| Mudstone | 15.42 | Very low |
| Fissile shale | 9.14 | Extremely low |

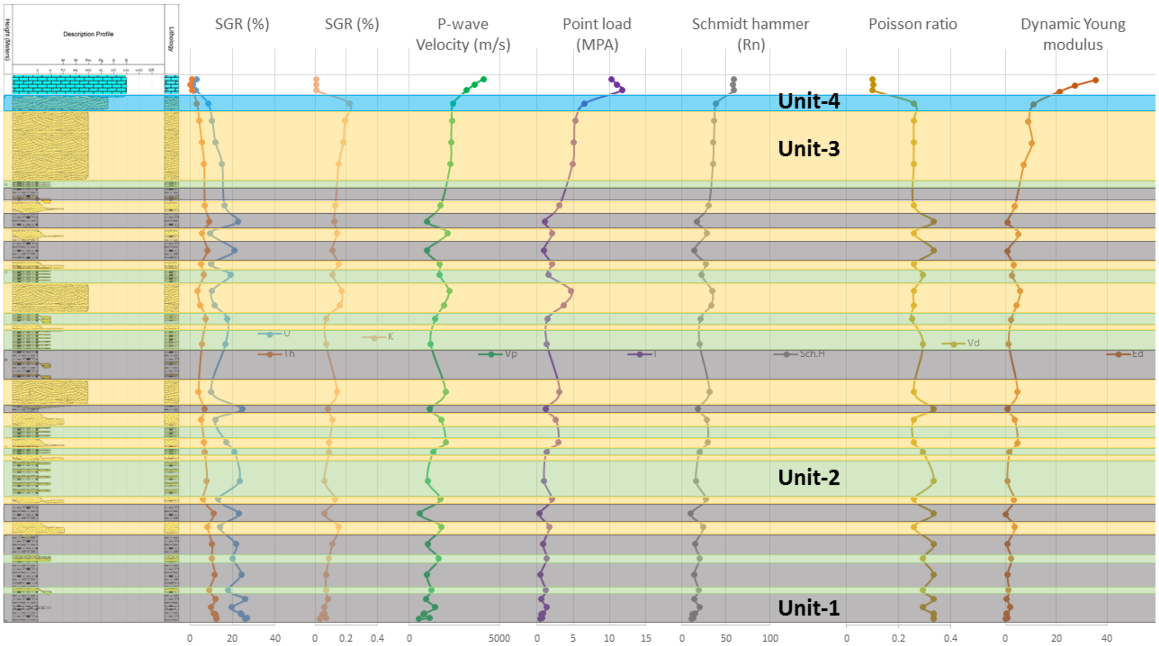

**Figure 5-37 Vertical lithostratigraphic section-1 showing the various lithofacies, sedimentary structures, Spectral gamma ray (SGR) readings, P-wave velocity (m/s) readings, Point load index (MPA) readings, Schmidt hammer (Rn) readings, Dynamic Poisson ratio values, Dynamic Young modulus values and geomechanical units.**

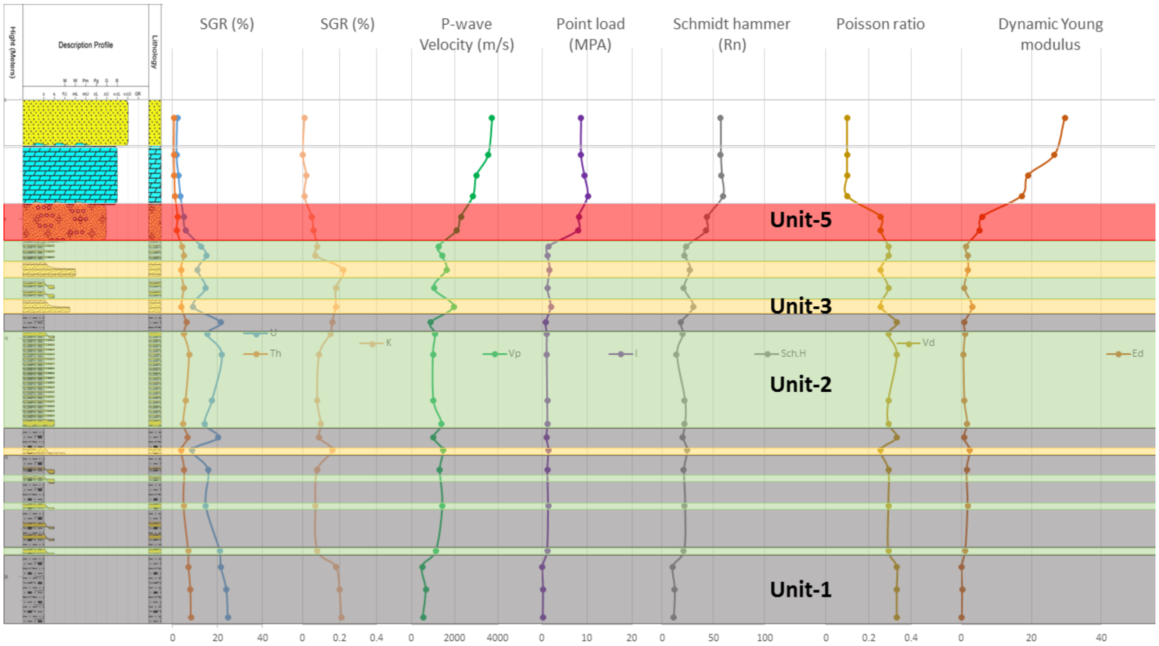

**Figure 5-38 Vertical lithostratigraphic section-2 showing the various lithofacies, sedimentary structures, Spectral gamma ray (SGR) readings, P-wave velocity (m/s) readings, Point load index (MPA) readings, Schmidt hammer (Rn) readings, Dynamic Poisson ratio values, Dynamic Young modulus values and geomechanical units.**

# CHAPTER 6

# Conclusions and Recommendations

## 6.1 Conclusions

This research has been carried to understand the relationships between natural fractures, lithological properties, and geomechanical properties. The outcrops of the study area are located in Central Saudi Arabia to the west of Qusayba' village, in Al-Qasim area, and they are composed of the Silurian lower part of Qusaiba hot shale member of Qlibah formation.

Qusaiba shale member in the study area consists of 5 main lithofacies. The fissile shale and mudstone lithofacies were deposited in an offshore depositional environment, siltstone lithofacies deposited in the transitional zone between offshore and lower shoreface depositional environments, very fine to fine-grained hummocky cross-stratified sandstone lithofacies deposited in the lower shoreface depositional environment, and fine to medium-grained low/high angle cross-stratified sandstone lithofacies deposited in the middle to the upper shoreface depositional environment. The 3D geostatistical model of Qusaiba shale member showed the distribution of the lithofacies in the study area, it consists of 3 zones representing the 3 depositional cycles of Qusaiba shale member. Zone-1 and zone-2 were modeled using sequential indicator simulation and zone-3 was modeled using truncated Gaussian simulation.

Lineaments interpretation of the Spot-7 and Landsat ETM+ satellite images showed two major directions in the study area; 320º that could be related to Najd fault system and 20º that could be related to the extensional activities which took place after Amar collision. Field investigations showed that the spacing between the 20º fractures is larger than the spacing between the 320º in different lithology. Fractures are much denser in the fissile shale and mudstone lithofacies than sandstones lithofacies, and spacing is smaller in the fissile shale and mudstone lithofacies than sandstones lithofacies. Lineaments and large-scale fractures are non-strata-bound fractures and they deal with the area as one big mechanical unit, but small-scale fractures are strata-bound fractures that propose different mechanical units within Qusaiba shale member in the study area. The spot-7 satellite image and field investigations revealed an existence of fault-related fold that could be a transverse fold with an axis trend of 40º.

Strength geomechanical parameters such as Schmidt hammer, point load index, uniaxial compressive strength, and dynamic young modulus have greater values in the hummocky cross-stratified sandstone, low/high angle cross-stratified sandstone, and pebbly sandstone than fissile shale, mudstone, and siltstone. The cross-plots of porosity versus different geomechanical properties revealed an inversely proportional relationship between them, and the cross-plots of different geomechanical properties versus each other revealed a directly proportional relationship. The lithological units of Qusaiba shale member in the study area were classified by using (Bieniawski, 1975) point load index classification and (Lucas, 2000) uniaxial compressive strength classification. The outcrops of Qusaiba shale member in the study area were divided into six geomechanical units; from unit-1 to unit-6 based on their fractures density and geomechanical properties.

## 6.2 Recommendations

1. Following recommendations could be effective in understanding the reservoir properties of the lower part of Qusaiba shale member.
2. A detailed study on the diagenesis and reservoir quality of Qusaiba shale member sandstone spots.
3. Correlation between the outcrops of the Silurian Qusaiba shale member in a larger scale.
4. Integration and comparison of outcrops data and subsurface data of Qusaiba shale member of Qalibah Formation.
5. More studies on the fold that was found in the area of outcrop of Qusaiba shale member in Qasim Area (North-Western part of Buraydah quadrangle) to find out it's tectonic and structural settings.

# References

Abdullatif, O. (2010). Geomechanical properties and rock mass quality of the carbonate Rus formation, Dammam dome, Saudi Arabia. Arabian Journal for Science and Engineering, 35(2), 173.

Al-Husseini, Moujahed I. "Origin of the Arabian Plate structures: Amar collision and Najd rift." GEOARABIA-MANAMA- 5 (2000): 527-542.

Alikarami, R., Torabi, A., Kolyukhin, D., & Skurtveit, E. (2013). Geostatistical relationships between mechanical and petrophysical properties of deformed sandstone. International Journal of Rock Mechanics and Mining Sciences, 63, 27-38.

Al-Laboun, A. A. (2009). Tectonostratigraphy of the exposed Silurian deposits in Arabia. Arabian Journal of Geosciences, 2(2), 119-131.

Ameen, S.M., Smart,B.G., Somerville, J.M., Hammilten,S., 2009. Predicting rock mechanical properties of carbonate from wireline logs (a case study from Arab-D reservoir, Ghawar field, Saudi Arabia), marine and petroleum geology 26,430-444.

Arman, H., Hashem,W., Eltoki,M., Abdelghany,O., Elsaiy,A., 2012. Petrographical and geomechanical properties of the lower Oligeocene limestone from Al-Ain city, United Arab Emirates, Arab Journal for Science and Engineering, DOI 101007-013-8.

Aydin, A., & Basu, A. (2005). The Schmidt hammer in rock material characterization. Engineering Geology, 81(1), 1-14.

Bellian, J. A., Kerans, C., & Jennette, D. C. (2005). Digital outcrop models: applications of terrestrial scanning lidar technology in stratigraphic modeling. Journal of sedimentary research, 75(2), 166-176.

Bertotti, G., Hardebol, N., Taal-van Koppen, J. K., & Luthi, S. M. (2007). Toward a quantitative definition of mechanical units: New techniques and results from an outcropping deep-water turbidite succession (Tanqua-Karoo Basin, South Africa). AAPG bulletin, 91(8), 1085-1098.

Biswas, D. K., et al. "Magnetostratigraphy of Plio-Pleistocene sediments in a 1700-m core from Osaka Bay, southwestern Japan and short geomagnetic events in the middle Matuyama and early Brunhes chrons." Palaeogeography, Palaeoclimatology, Palaeoecology 148.4 (1999): 233-248.

Broch, E., & Franklin, J. A. (1972, November). The point-load strength test. In International Journal of Rock Mechanics and Mining Sciences & Geomechanics Abstracts (Vol. 9, No. 6, pp. 669-676). Pergamon.

Brown, E. T. (1981). Rock characterization. Test and Monitoring, Pergamon Pre~ Oxford.

Buckley, S. J., Howell, J. A., Enge, H. D., & Kurz, T. H. (2008). Terrestrial laser scanning in geology: data acquisition, processing and accuracy considerations. Journal of the Geological Society, 165(3), 625-638.

Cole, G. A. (1994). Graptolite-chitinozoan reflectance and its relationship to other geochemical maturity indicators in the Silurian Qusaiba Shale, Saudi Arabia. Energy & fuels, 8(6), 1443-1459.

Cole, G. A. (1995). The Petroleum Geochemistry of the Silurian Qusaiba Shale, Saudi Arabia.

Craigie, N. W. (2016). Chemostratigraphy of the Silurian Qusaiba Member, Eastern Saudi Arabia. Journal of African Earth Sciences, 113, 12-34.

Dacre, H. F., Grant, A. L., Hogan, R. J., Belcher, S. E., Thomson, D. J., Devenish, B. J., ... & Mattis, I. (2011). Evaluating the structure and magnitude of the ash plume during the initial phase of the 2010 Eyjafjallajökull eruption using lidar observations and NAME simulations. Journal of Geophysical Research: Atmospheres, 116(D20).

Dott, R. H., and Joanne Bourgeois. "Hummocky stratification: significance of its variable bedding sequences." Geological Society of America Bulletin 93.8 (1982): 663-680.

Faqira, M., Bhullar, A., & Ahmed, A. (2010). Silurian Qusaiba Shale Play: Distribution and Characteristics. In AAPG Heidelberg Conference, Austin.

Gao, Q., Hu, J., Tao, J., & Yu, X. B. (2014). Experimental Characterization of the Anisotropic Behaviors of Shale Rock. In Geo-Congress 2014 Technical Papers@ sGeo-characterization and Modeling for Sustainability (pp. 563-571). ASCE.

Glover, P. (2011). Petrophysics MSc Course Notes. Clay/Shale Effects on Porosity and Resistivity Logs.

Grabowski Jr, G. J. (2005, January). Sequence Stratigraphy and Distribution of Silurian Organic-Rich" Hot Shales" of Arabia and North Africa. In International Petroleum Technology Conference. International Petroleum Technology Conference.

Hayton, S., Heine, C., Sherba, E., Gratto, B. E., Zhang, S., & Wang, S. (2010, January). A New Exploration Play for Saudi Arabia, the Rhuddanian (Lower Qusaiba) Sandstone. In SPE Deep Gas Conference and Exhibition. Society of Petroleum Engineers.

Hawkes, I., & Mellor, M. (1970). Uniaxial testing in rock mechanics laboratories. Engineering Geology, 4(3), 179-285.

Hsieh, Y. M., Li, H. H., Huang, T. H., & Jeng, F. S. (2008). Interpretations on how the macroscopic mechanical behavior of sandstone affected by microscopic properties—revealed by bonded-particle model. Engineering Geology, 99(1), 1-10.

Jaeger, J. C., Cook, N. G., & Zimmerman, R. (2009). Fundamentals of rock mechanics. John Wiley & Sons.

Jones, P. J., & Stump, T. E. (1999). Depositional and tectonic setting of the Lower Silurian hydrocarbon source rock facies, central Saudi Arabia. AAPG bulletin, 83(2), 314-332.

Kanitpanyacharoen, W., Wenk, H. R., Kets, F., Lehr, C., & Wirth, R. (2011). Texture and anisotropy analysis of Qusaiba shales. Geophysical Prospecting, 59(3), 536-556.

Khandelwal, M., & Ranjith, P. G. (2010). Correlating index properties of rocks with P-wave measurements. Journal of Applied Geophysics, 71(1), 1-5.

Kharusi, A., & Mohammed, L. (2009). Correlation between high resolution sequence stratigraphy and mechanical stratigraphy for enhanced fracture characteristic prediction.

Konert, G., Afifi, A. M., Al-Hajri, S. A., De Groot, K., Al Naim, A. A., & Droste, H. J. (2001). AAPG Memoir 74, Chapter 24: Paleozoic stratigraphy and hydrocarbon habitat of the Arabian plate.

Laboun, Abdulaziz A. "Paleozoic tectono-stratigraphic framework of the Arabian Peninsula." Journal of King Saud University-Science 22.1 (2010): 41-50.

Laboun, Abdulaziz Abdullah. "Regional tectonic and megadepositional cycles of the Paleozoic of northwestern and central Saudi Arabia." Arabian Journal of Geosciences 6.4 (2013): 971-984.

Laubach, S. E., Olson, J. E., & Gross, M. R. (2009). Mechanical and fracture stratigraphy. AAPG bulletin, 93(11), 1413-1426.

Lüning, S., Craig, J., Loydell, D. K., Štorch, P., & Fitches, B. (2000). Lower Silurianhot shales' in North Africa and Arabia: regional distribution and depositional model. Earth-Science Reviews, 49(1), 121-200.

Mahmoud, M. D., Vaslet, D., & Husseini, M. I. (1992). The Lower Silurian Qalibah Formation of Saudi Arabia: An Important Hydrocarbon Source Rock (1). AAPG Bulletin, 76(10), 1491-1506.

Manivit, J., Vaslet, D., Berthiaux, A., Le Start, P., & Fourniguet, J. (1986). Geologic map of the Buraydah quadrangle, sheet 26G. Kingdom of Saudi Arabia: DGMR, Geoscience Map GM-114A.

Marshall, J. E. A. (1995). The Silurian of Saudi Arabia: thermal maturity, burial history and geotectonic environment. Review of Palaeobotany and Palynology, 89(1), 139-150.

McClure, H. A. "Chitinozoan and acritarch assemblages, stratigraphy and biogeography of the Early Palaeozoic of Northwest Arabia." Review of Palaeobotany and Palynology 56.1 (1988): 41-60.

Miller, M. A., & Melvin, J. (2005). Significant new biostratigraphic horizons in the Qusaiba Member of the Silurian Qalibah Formation of central Saudi Arabia, and their sedimentologic expression in a sequence stratigraphic context. GeoArabia, 10(1), 49-92.

Miller, R.P., 1965. Engineering classification and index properties for intact rock. PhD Thesis, University of Illinois.

Mwanga, A., Lamberg, P., & Rosenkranz, J. (2015). Comminution test method using small drill core samples. Minerals Engineering, 72, 129-139.

Nelson, R. (2001). Geologic analysis of naturally fractured reservoirs. Gulf Professional Publishing.

Odling, N. E., Gillespie, P., Bourgine, B., Castaing, C., Chiles, J. P., Christensen, N. P., ... & Trice, R. (1999). Variations in fracture system geometry and their implications for fluid flow in fractured hydrocarbon reservoirs. Petroleum Geoscience, 5(4), 373-384.

Pollard, D. D., & Aydin, A. (1988). Progress in understanding jointing over the past century. Geological Society of America Bulletin, 100(8), 1181-1204.

Powers, R. W., 1968, Saudi Arabia (excluding Arabian Shield). Lexique Stratigraphique International, v. 3, Asie. fascicle lObl: Paris, Centre National de la Recherche Scientifique. 177p.

Prabu, P., & Rajagopalan, B. (2013). Mapping of lineaments for groundwater targeting and sustainable water resource management in hard rock hydrogeological environment using RS-GIS. INTECH publications, http:// dx. doi. org, 10(5772), 55702.

Pyrak-Nolte, L. J., Myer, L. R., Cook, N. G., & Witherspoon, P. A. (1987, January). Hydraulic and mechanical properties of natural fractures in low permeability rock. In 6th ISRM Congress. International Society for Rock Mechanics.

Sabatakakis, N., Tsiambaos, G., & Koukis, G. (1993, September). Index properties of soft marly rocks of the Athens basin, Greece. In Proceedings of International Symposium Geotechnical Engineering of Hard soils and Soft Rocks (Vol. 1, pp. 275-279).

Sachdev, S., & Nelson, D. R. (1985). Statistical mechanics of pentagonal and icosahedral order in dense liquids. Physical Review B, 32(3), 1480.

Senalp, M., & Al-Duaiji, A. A. (2001). Qasim Formation: Ordovician storm-and tide-dominated shallow-marine siliciclastic sequences, Central Saudi Arabia. GEOARABIA-MANAMA-, 6, 233-268.

Strijker, G., Bertotti, G., & Luthi, S. M. (2012). Multi-scale fracture network analysis from an outcrop analogue: A case study from the Cambro-Ordovician clastic succession in Petra, Jordan. Marine and Petroleum Geology, 38(1), 104-116.

Underwood, C. A., Cooke, M. L., Simo, J. A., & Muldoon, M. A. (2003). Stratigraphic controls on vertical fracture patterns in Silurian dolomite, northeastern Wisconsin. AAPG bulletin, 87(1), 121-142.

Vaslet, D., l 987c. The Paleozoic (pre-Late Permian) of central Arabia and correlations with neighboring regions: Saudi Arabian Directorate General of Mineral Resources Technical Record BRGM-TR-07- 2. 167p.

Watkins, H., Bond, C. E., Healy, D., & Butler, R. W. (2015). Appraisal of fracture sampling methods and a new workflow to characterise heterogeneous fracture networks at outcrop. Journal of Structural Geology, 72, 67-82.

# Vitae

Name :Mohamed Ibrahim Mahgoub Ibrahim

Nationality :Sudanese

Date of Birth :5/10/1989

Email :mohdzma@hotmail.com

Address :KFUPM, Dhahran P.O.box:7682

Academic Background :Geology